Technische Universität München
TUM School of Medicine and Health

Multiparametric imaging of endogenous murine PDAC and its ex-vivo referencing using 1-^{13}C-pyruvate MRSI

Moritz Niklas Stanislaus Mayer

Vollständiger Abdruck der von der TUM School of Medicine and Health der Technischen Universität München zur Erlangung eines

Doktors der Medizin (Dr. med.)

genehmigten Dissertation.

Vorsitz: apl. Prof. Dr. Ute Reuning

Prüfende der Dissertation:

1. apl. Prof. Dr. Rickmer Braren
2. Prof. Dr. Franz Schilling

Die Dissertation wurde am 23.04.2024 bei der Technischen Universität München eingereicht und durch die TUM School of Medicine and Health am 10.10.2024 angenommen.

MULTIPARAMETRIC IMAGING OF ENDOGENOUS MURINE PDAC AND ITS EX-VIVO REFERENCING USING 1-^{13}C-PYRUVATE MRSI

Moritz Niklas Stanislaus Mayer

Für Emil

TABLE OF CONTENTS

LIST OF ABBREVIATIONS

2P	2-Parameter model
3P	3-Parameter model
ADC	Apparent diffusion coefficient
ADC_{perf}	ADC value indicative of microvascular perfusion
al.	Alii (m)/aliae (f)/alia (n)
APAF	Apoptotic protease activating factor
AUC	Area under the curve
b	b-value
BAX	Bcl2 associated x protein
BRCA	Breast cancer antigen
BSA	Bovin serum albumin
Bq	Becquerel
C	Carbon
CD	Cluster of differentiation
CDH1	Cadherin 1
CDK	Cyclin-dependant kinase
CDKN	Cyclin-dependant kinase inhibitor

CE	Classical epithelial
CI	Confidence interval
c.l.	Cell line
CRE	Cyclization recombinase
CSI	Chemical-shift imaging
CT	Computer tomography
CST	Color saturation threshold
CTS	Cumulative threshold spectrum
DAB	3,3'Diaminobenzidine
DAPI	4',6-diamido-2-phenylindole
DAPI3	Blue channel image of DAPI stained nuclei
DAPITexture	Virtual Image containing the textural information solely of DAPI stained regions
DCE-MRI	Dynamic contrast enhanced magnetic resonance Imaging
DICOM	Digital imaging and communications in medicine
DMEM	Dulbecco's modified eagle medium
DNA	Deoxyribonucleic acid
DNP	Dynamic nuclear polarisation
Dotarem	Gadoteric acid
DTM	Distance transform matrix
DWI-MRI	Diffusion weighted Imaging - MRI

E	Epithelial
EDTA	Ethylenediaminetetraacetic acid
EGF	Epidermal growth factor
EGFR	EGF-receptor
FA	Flip Angle
FBS	Fetal bovine serum
FELASA	Federation of European Laboratory Animal Science Association
^{18}F-FDG	^{18}F-fluor-2-desoxy-glucose
^{18}F-FDG-PET	^{18}F-FDG-Positron emission tomography
FFP	Formalin-fixed paraffin embedded tissue
FOV	Field of view
FSE	Fast spin echo
G	Strength of Gradient
GEMM	Genetically engineered mouse model
GF	Gaussian filter
GLCM	Grey-level co-occurrence matrix
GLUT	Glucose transporter
GTPase	Guanosine triphosphate hydrolysing enzyme

H	Hydrogen
HE	Haematoxylin-eosin
H&E	Haematoxylin-eosin
H.E.	Haematoxylin-eosin
HIF	Hypoxia inducible factor
HL	Half life ($t_{1/2}$)
HP	Hyperpolarized
hPDAC	Human pancreatic ductal adenocarcinoma
I	Image
I	Intensity
IAT	Image analysis tool
IF	Immunofluorescence
IHC	Immunohistochemistry
IPMN	Intraductal papillary mucinous neoplasia
IRB	Institutional review board
i.v.	Intravenous
IVIM	Intravoxel incoherent motion
KRAS	Kirsten rat sarcoma virus gene

KRT	Keratin
LDHA	Lactate-dehydrogenase A
LPA	Low-point approximation/approach
LSL	Lox-Stop-Lox
M	Magnetisation
M	Mega-
M	Mesenchymal
m	Milli-
m-	murine
µ	Micro-
MCT	Monocarboxylate transporter
min	Minimum
max	Maximum
MR-	Magnetic resonance
MRI	MR-Imaging
MRSI	Magnetic resonance spectroscopy imaging
MRT	MRI scanner
n	number
n	new

NaCl	Sodium chloride
NaI	Sodium Iodide
o	old
p	p-value (probability value)
p	Protein
PanIn	Pancreatic intraepithelial neoplasia
PBS	Phosphate buffered saline
PDAC	Pancreatic ductal adenocarcinoma
PDH	Pyruvate dehydrogenase
PET	Positron emission tomography
PFA	Paraformaldehyde
pH	$-\log_{10}[H^+/(mol*dm^3)]$ (*historically potential of hydrogen*)
PPC	Positive Pixel Count
P/S	Penicillin/Streptomycin
PTF, ptf	Pancreas associated transcription factor
PUMA	P53 upregulated modulator of apoptosis
QM	quasimesenchymal
r	(Pearson's) correlation coefficient

R2	Relaxation rate corresponding to T_2
RGB	RGB color model (*where R stands for red, G for green and B for blue*)
ROI	Region of interest
RT	Room temperature
S	Signal
s.c.	Subcutaneous
SD	Standard deviation
SE	Spin echo
Skew	Skewness
SNR	Signal to noise ratio
SPF	Simplified perfusion fraction
ST	Subtraction approach
SUV	Standard uptake value
T	[Tesla]
T	Threshold
T	Tumor
t	Offset of threshold from turning point in CTS
T_1	Spin-lattice relaxation

T_2	Spin-spin relaxation
T_2w-MRI	T_2-weighted MRI
TCA	Tricarboxylic acid
TE	Echo time
TGF	Transforming growth factor
TIF	Tagged image file
T/K-ratio	Tumor to kidney ratio
T/L-ratio	Tumor to liver ratio
T/M-ratio	Tumor to muscle ratio
TMA	Tissue micro-array
TR	Repetition time
TRIS	Tris(hydroxymethyl)aminomethane
t-test	Hypothesis test statistic
VEGF	Vascular endothelial growth factor
ZPF	*Zentrum für präklinische Forschung* (Centre for preclinical research)
∂	Duration of gradient
Δ	Time interval between gradients

I. INTRODUCTION

Pancreatic cancer has one of the worst prognoses among all gastrointestinal tumor entities (Ilic and Ilic 2016). The vast progress made in determining molecular mechanisms of pancreatic ductal adenocarcinoma (PDAC) has so far been unrewarding regarding the development of targeted therapies due to the high genetic, metabolic and structural heterogeneity of the disease. To this day, the search for meaningful biomarkers for human pancreatic ductal adenocarcinoma (PDAC) across all modalities is ongoing and has been unavailing (Costello, Greenhalf et al. 2012, Zhou, Xu et al. 2017, Zhang, Sanagapalli et al. 2018, O'Neill and Stoita 2021). Imaging biomarkers are well suited to represent the heterogeneity of PDAC, as they are able to better represent the whole extend of the disease. This is an advantage over molecular and histopathological evaluation of biopsy material that is derived of a single tumor sample. This work aims at expanding on the structural and metabolic properties of PDAC using a multimodal in-vivo imaging protocol (T_2-weighted MRI, DWI, 1-^{13}C-pyruvate MRSI, ^{18}F-FDG PET) that are validated by ex-vivo techniques (histology, immunohistochemistry, cytology, immunofluorescence) in different disease models. In order to structure this depiction, **this work is divided into three parts, each of which may be read separately.**

In Part One (III.) a multimodal imaging platform (including T_2-weighted MRI, DWI, 1-^{13}C-pyruvate MRSI, and ^{18}F-FDG-PET) for endogenous PDAC is established, and the results are correlated to ex-vivo findings. In this part, questions regarding the biological meaning of metabolic imaging data are discussed. Furthermore, the role of MCT4 as a relevant structural and metabolic biomarker is ventilated.

Part Two (IV.) focuses on the ties of morphometric and texture-derived determinants of PDAC samples and monocarboxylate transporter 4 (MCT4) expression. Thereby it is commenting on a connection of form and function in PDAC spanning multiple murine models (orthotopic and endogenous) and probes (cytology and immunohistochemistry (IHC)).

Part Three (V.) evaluates the meaning of MCT4 tissue expression and its association to established tumor subtypes in human PDAC. Thereby, it seeks to clarify its standing in terms of diagnostic relevance as a biomarker for human PDAC and its suitability as a biological reference for 1-^{13}C-pyruvate MRSI.

Finally, **the Conclusion (VI.)** critically evaluates the knowledge gain of these experiments and their contribution to future developments in imaging and characterization of PDAC.

Further additions to Parts One to Three as well as the acknowledgement of contributions may be found in the **Appendix (IX.).**

II. BACKGROUND

This chapter includes a depiction of pathophysiological features of PDAC, its subtypes, mouse models and imaging modalities. It provides a short overview on the basics and current literature in each chapter that are important to comprehend the experimental setup in the following experiments.

1. PANCREATIC DUCTAL ADENOCARCINOMA (PDAC)

The majority (80-90%) of pancreatic cancers are derived from epithelial tissue of pancreatic ducts and acini. It is widely acknowledged that human PDAC emerges from precursor lesions of exocrine pancreatic tissue (Gnoni, Licchetta et al. 2013, Goral 2015) that are classified as pancreatic intraepithelial neoplasia (PanIN) 1-3. These stages incorporate underlying genetic modifications as well as changes in the phenotype of the epithelium. Several well-known mutations (e.g. KRAS, p53, CDKN2, SMAD4) accumulate during tumorgenesis and in the following change the tissue's morphology. KRAS is the most commonly altered oncogene in PDAC that is already present in early precursor lesions. Furthermore the presence or KRAS mutations is directly associated with grade of dysplasia (36% in PanIN-1a, 44% in PanIN-1b, 87% in PanIN 2-3) (Kanda, Matthaei et al. 2012). In addition, it has been shown in a $KRAS^{G12D}$-driven PDAC mouse model that its activity is essential for tumor maintenance (Ying, Kimmelman et al. 2012). KRAS generally increases glycolytic flux (Ying, Kimmelman et al. 2012) and is indispensible for the retention of tumor metabolism and growth. Moreover, 76% of human PDAC reveal mutated TP53 resulting in its loss of function (Rozenblum, Schutte et al. 1997). The normal role of TP53 is to prevent flawed DNA from replication and spreading by directing the affected cell towards cell cycle arrest or cellular apoptosis. Therefore, functionally impaired TP53 supports proliferation and growth of abnormal cells.

Interestingly, this genetic predetermination of carcinogenesis yields highly heterogeneous tumors that pose large challenges to diagnostics and therapy.

2. THE ROLE OF GLUCOSE, LACTATE AND MONOCARBOXYLATE TRANSPROTERS IN PDAC

Glucose is the dominant in vivo substrate for ATP synthesis (through glycolysis, TCA cycle and respiratory chain), anabolic pathways including DNA composition (through the pentose-phosphate pathway) and protein glycosylation (through the hexosamine biosynthesis pathway). All of these are altered during carcinogenesis and become essential for tumor cell survival. Compared to normal cells, proliferating tumor cells use proportionally more glucose to entertain biosynthesis (Lunt and Heiden 2011). In murine models of PDAC, it has been shown that mutant KRAS directly promotes glucose uptake through an increased expression of GLUT1 and hexokinase as well as glucose flux into glycolysis, pentose-5-phosphate pathway and hexosamine biosynthetic pathway (Ying, Kimmelman et al. 2012).

Under normoxic conditions, healthy tissue further oxidizes pyruvate, the end product of glycolysis, to acetyl-CoA, which then enters the mitochondrial TCA-cycle. As early as 1924, it has been recognized by Otto Warburg that tumor cells exhibit increased levels of anaerobic glycolysis with the generation of lactate even with sufficient supply of oxygen. An increased lactate production has also been confirmed for human PDAC further influenced by an hypoxic microenvironment (Feig, Gopinathan et al. 2012). This so called “Warburg-shift” is thought to have beneficial effects for the tumor cells regarding oxygen-independence of energy supply as well as biosynthetic capacities. It is based on an increased induction of lactate dehydrogenase A (LDHA) by a multitude of mutant oncogenes (Chang, Liu et al. 2022) as well as increased levels of other glycolytic enzymes and required transporters (such as MCT1 and MCT4) that export excessive lactate (Halestrap and Wilson 2012) out of the cell to prevent oxidative stress and stalling of the glycolytic flux. The role of increased levels of LDHA, MCTs and glycolytic capacity exceeds mere metabolic considerations as they influence invasiveness of cancer cells (Kong, Nøhr-Nielsen et al. 2016), their power to establish metastases according to the “seed” and “soil” theory (Lehuédé, Dupuy et al. 2016, Nimmakayala, Leon et al. 2021) as well as survival (Baek, Tse et al. 2014).

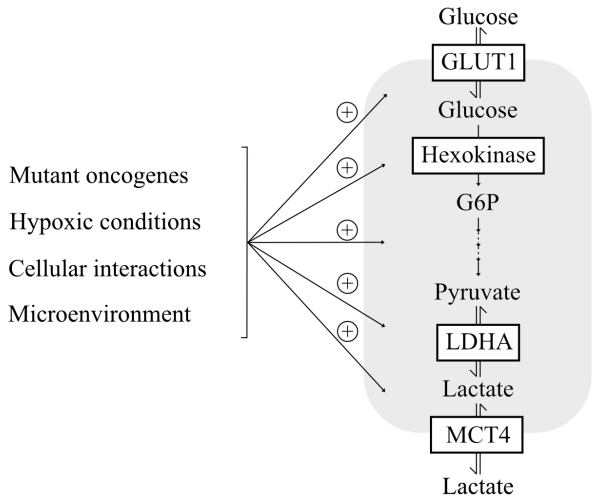

Fig.II-1: Illustration of altered glycolytic determinants – The illustration shows the effect of several factors (on the left) on parts of the glycolytic pathway including Glucose Transporter 1 (GLUT1), Hexokinase, lactate dehydrogenase A (LDHA) and monocarboxylate transporter 4 (MCT4)

3. SUBTYPES OF PDAC

Three transcriptional subtypes (classical, quasi-mesenchymal [i.e. squamous] and exocrine-like) of PDAC have been identified in cytology-derived and laser-microdissected transcriptome samples (Collisson, Sadanandam et al. 2011). The classical subtype shows high expression of genes mainly found in epithelial tissue for example adhesion-related proteins Cytokeratine CK7 and E-Cadherine. As the name suggests the quasi-mesenchymal subtype exhibited high expression of genes associated with mesenchyme, such as Vimentine and N-Cadherine (Collisson, Sadanandam et al. 2011). Furthermore, cell lines of the classical subtype showed high sensitivity to inhibitors of lipogenesis whereas cells from quasi-mesenchymal lesions showed high sensitivity to inhibitors of glycolysis. Additionally, they differed in their use of glutamine and glucose (Daemen, Peterson et al. 2015). From these findings the genetic and transcriptional classification in classical and quasi-mesenchymal subtypes has been expanded by metabolic classifications of lipogenic and glycolytic.

Kalimuthu et al. demonstrated how morphologic growth patterns evaluated in PDAC histology are associated with transcriptional subtypes and overall survival. Non-gland forming lesions were correlated to worse survival and quasi-mesenchymal subtype (S, Wilson et al. 2020). This illustrates that observed and morphologically characterized patterns can be regarded results of genetic changes.

Furthermore, Heid et al. introduced a structural classification, assigning murine PDAC lesions into groups of $PDAC^{low}$, $PDAC^{med}$ and $PDAC^{high}$ depending on the amount of tumor cells and their clustering within the tissue in histopathological examination. They showed that these classifications correlate with in-vivo imaging findings of Diffusion-weighted MRI (DWI) (Heid, Steiger et al. 2017).

More transcriptionally defined subtypes and different classifications have been presented and certainly are of high interest (Moffitt, Marayati et al. 2015, Bailey, Chang et al. 2016). Nevertheless, in this work I will focus on the two main subtypes classical epithelial and quasi-mesenchymal with their respective ties to metabolism and morphology. This is due to the shift in metabolism that is expected between those two distinct subgroups (the exocrine-like subtype will not be regarded in this work as its status as a distinct subtype is unclear) (Puleo, Nicolle et al. 2018).

4. MOUSE MODELS

Mouse models imitating human pathophysiology allow investigating pathophysiological processes. In this work, two different mouse models – one model with orthotopic implantation of characterized cell lines, the other a genetically engineered mouse model (GEMM) with endogenously grown heterogeneous lesions – were used. It will be discussed in further detail below in which way insights gained on murine PDAC in these models may be transferred to human PDAC.

4.1 ORTHOTOPIC MOUSE MODEL OF PDAC

Orthotopic mouse models of PDAC are implemented by surgically seeding tumor cells into pancreatic tissue of immunodeficient mice. Thereby the specific tumor microenvironment is thought to better mimic human disease than subcutaneous tumor models with a higher translational value of the results while maintaining experimental advantages such as controlled genetics and growth. It has been shown for pancreatic cancer that orthotopic growth of tumor cells in contrast to heterotopic transplantation or culture induces different genetic translation especially of genes involved in cell migration (Nakamura, Fidler et al. 2007). In addition, implantation site influence pathogenesis and even response to therapy (Erstad, Sojoodi et al. 2018). Nevertheless, translational meaningfulness for other models may be limited as the orthotopic model renders tumors with dense tumor cell growth and comparably low portions of desmoplastic stroma. This is further underlined by the understanding that tumor evolution and development is bound to host specific biology (Ben-David, Ha et al. 2017).

4.2 ENDOGENOUS MOUSE MODEL OF PDAC (GEMM)

Endogenous models of PDAC are created by introducing targeted changes into the pancreatic genome. Unsuccessful attempts of generating endogenous models of PDAC with mere loss of tumor suppressors indicate that tumor suppressor gene loss is not alone able to initiate PDAC (Donehower, Harvey et al. 1992, Yang, Li et al. 2002). The development of PDAC is mainly dependant on changes in the proto-oncogene KRAS. Common changes in KRAS include a missense mutation in Codon 12. Development of a Lox-Stop-Lox(LSL)-$KRAS^{G12D}$ allele (Jackson, Willis et al. 2001) then paved the way for reliable PanIn and PDAC models (Hingorani, Petricoin et al. 2003). The used mice express a *ptf1a*-promoter dependant CRE-Recombinase which then cuts the stop-codon placed in front of $KRAS^{G12D}$ and initiates expression of mutant KRAS during pancreatic development. This ensures that these changes remain specific to the pancreatic tissue.

Similar to human PDAC, mPDAC derived from GEMM is of predominantly glandular origin. It mimics clinical features such as cachexia, ascites and lethargy (Tuveson and Hingorani 2005). Tumors show ductal, cribriform or combined growth patterns. During tumor progression, ductal structure is lost and dense neoplastic growth patterns dominate. The histology observed is very similar to human PDAC (Heid, Steiger et al. 2017).

5. IMAGING MODALITIES

In this work, a multimodal imaging approach combining structural and metabolic imaging modalities was used. Therefore, this chapter aims at introducing relevant literature regarding these modalities in PDAC and relatable models. Further information about the signal measurements and their interpretation may be found in the Appendix (VII.2).

Diffusion-weighted imaging (DWI) using multiple b-values, allows the calculation of apparent diffusion coefficient (ADC)-Maps depicting the water diffusivity of the tissue. Low ADC values indicate diffusion restriction as it can be imposed by e.g. increased cell density and/or loss of ductal structures. This has been shown in murine as well as human PDAC, where decreased ADC values of PDAC lesions correlated with increased tumor cellularity (Heid, Steiger et al. 2017, Jeon, Jang et al. 2021, Zhu, Zhang et al. 2021) and worse disease-free survival (Jeon, Jang et al. 2021). Furthermore, it has been recognised that quantitative ADC maps enable the prediction immunohistochemical expression patterns of epithelial-to-mesenchymal transition in human PDAC potentially enabling patient stratification for targeted therapies (Mayer, Kraft et al. 2021).

Metabolic imaging is a promising tool to further enable non-invasive subtype stratification of PDAC. Magnetic resonance spectroscopic imaging (MRSI) enables the imaging of hyperpolarized 1-^{13}C-pyruvate accumulation and conversion in tumorous tissue. In breast cancer, it has been demonstrated that the ratio of area under the curve (AUC) of lactate and pyruvate (1-^{13}C-lactate/1-^{13}C-pyruvate) signals correlates with MCT1 and HIF1A expression (Gallagher, Woitek et al. 2020) and therapy response (Woitek, McLean et al. 2021). Furthermore, studies conducted in prostate cancer found ties between a high 1-^{13}C-lactate-to-1-^{13}C-pyruvate ratio, LDHA, MCT4 expression and tumor grade (Chen, Aggarwal et al. 2020). In murine PDAC hyperpolarized 1-^{13}C-pyruvate MRSI has been used to detect malignant lesions (Dutta, Pando et al. 2020) and stratify them depending on their glycolytic metabolism and heterogeneity (Heid, Münch et al. 2022). First study performed on 2 patients confirms that this method is usable for PDAC(Stødkilde-Jørgensen, Laustsen et al. 2020).

Other than 1-^{13}-C-pyruvate MRSI, which enables dynamic imaging of enzymatic process downstream of glycolysis, ^{18}F-FDG PET is used to detect glucose uptake and phosphorylation ("metabolic trapping") in the tumor. Its methodology is further explained in the appendix. In pancreatic cancer, it has been used to reliably detect tumors (Serrano, Chaudhry et al. 2010) and stratify lesions (Hyun, Kim et al. 2016). Because of its limitation to solely detect glucose uptake a low specifity mainly regarding the differentiation of cancerous lesions and pancreatitis has been attributed to this modality (Wang, Yang et al. 2014).

6. DIGITAL ANALYSIS OF EX-VIVO DIAGNOSTICS

In this work H&E stained histology, immunohistochemistry and immunofluorescence stained cytology are analyzed and referenced to in-vivo imaging data. These ex-vivo diagnostics are analyzed from digital images to extract quantifiable features.

Images of immunofluorescence (IF) with fluorescent-labeled antibodies are used to detect the expression of specific antigens. In this study, it is applied on cytology that was drawn from orthotopically and endogenously grown tumors. Indirect immunofluorescence works by incubating the cells with a primary antibody that binds a specific antigen. After that, a second fluorophore-labeled antibody is added that binds the first. This two-step process amplifies available signal and thereby increases sensitivity (Odell and Cook 2013). Using multiple antibodies that are only sensitive to their specific wavelength enable collocation of expression patterns and thereby effective biological characterization. Based on the technique of indirect immunofluorescence the signal is in close vicinity to the binding site. Furthermore, higher signal intensities correlate with higher expression of the antigen. Nevertheless, there is not a linear proportionality to signal intensities because of spatial overlapping effects and multiple antibody binding. That is why, data derived from images with this

technique display semi-quantitative ratios that are of high quality for comparison between groups but do not equal absolute measurements.

DAPI (4',6-diamidino-2-phenylindole dichloride) is a rather specific fluorescent probe for DNA attaching to the minor groves of Adenine and Thymine rich sequences (Kapuscinski 1995) and is consequently used to display nuclei in immunofluorescence cytology. DAPI images can be used to assess the number and shape of nuclei contained in an image. Also antibodies for E-Cadherin (a cell-cell adhesion molecule – indicative of the epithelial subtype of PDAC), Vimentin (an intermediate filament protein – expressed in mesenchymal and migrating cells – indicative of the (quasi)mesenchymal subtype of PDAC) and MCT4 were used.

Comparable to the two-step process of indirect immunofluorescence, immunohistochemistry (IHC) is at its core based on an antigen specific binding of an antibody-reporter complex. Most commonly visualization is implemented using a reporter complex containing DAB (brown chromogen). Immunohistochemistry allows the detection of biomarkers in the context of their original tissue and consequently is very useful for describing spatial distribution and structural dependences of biomarker expression. Similarly to IF staining is more intense with multiple antibody binding events – however a linear proportionality is not given.

Images from histology, IF and IHC are taken as images in the RGB color space (red, green, blue) using a microscopy camera and processed as grey value image matrices, where an intensity value (I) between 0 and 255 is assigned to each pixel. These image matrices allow complex calculations. A standard image analysis workflow contains the following steps: Reading the Image – preprocessing – segmentation – feature extraction and classification. For image analysis platforms such as MATLAB, Image J or packages such as Aperio's Imagescope are used. For segmentation of a biological image – in this work – mainly thresholding-based techniques are used. Thresholding works by assigning a value of 1 to all pixels above a threshold (T) and 0 to all pixels below T. T can be a numeric value or - as the matrix definition of an image allows algebraic calculations - a ratio or sum. T can be determined manually or by performing calculations based on the image matrix values. Second order thresholding may derive a threshold not using image matrix values but classification results for determining a threshold (this is further illustrated in IV.2.3, Fig.IV-2, Fig.IV-3). Furthermore, T can be assigned generally or localized for portions of an image.

III. PART ONE: IMAGING METABOLISM OF ENDOGENOUS MURINE PDAC IDENTIFIES $AUC_{LACTATE}/AUC_{PYRUVATE}$ AS A STABLE MULTIDIMENSIONAL PARAMETER DEPENDING ON CELLULAR METABOLISM, TUMOR CELL DENSITY AND PERFUSION

1. INTRODUCTION

Endogenous mPDAC derived from a GEMM including the mutation of KRAS and TP53 mimics the pathogenesis of human PDAC (Hingorani, Petricoin et al. 2003, Tuveson and Hingorani 2005). These tumors show a high similarity to human PDAC concerning morphology, growth patterns and subtypes (Heid, Steiger et al. 2017). Furthermore, they show distinct recruiting of desmoplastic stroma and complex patterns of angiogenesis (Heid, Münch et al. 2022)

In this sub-study a multimodal imaging platform including structural (T_2-weighted MRI, DWI) and metabolic (hyperpolarized 1-^{13}C-pyruvate MRSI, ^{18}F-FDG PET) modalities was established for endogenous mPDAC. Furthermore, the imaging results are referenced to corresponding histology, immunohistochemistry and cytology using a novel image analysis tool implemented in MATLAB. Additionally, the micro-structural and metabolic short-term stability of these tumors is evaluated using a longitudinal study protocol.

The goal of this study is to shed light on the following questions:

- In which way do such determinants as cellularity, stromal content and perfusion influence metabolic imaging in endogenous mPDAC?
- Are MCT4 and GLUT1 relevant tissue biomarkers for tumor stratification in endogenous mPDAC?

These questions were chosen in order to evaluate the multiparametric study protocol as a platform for future therapy trials.

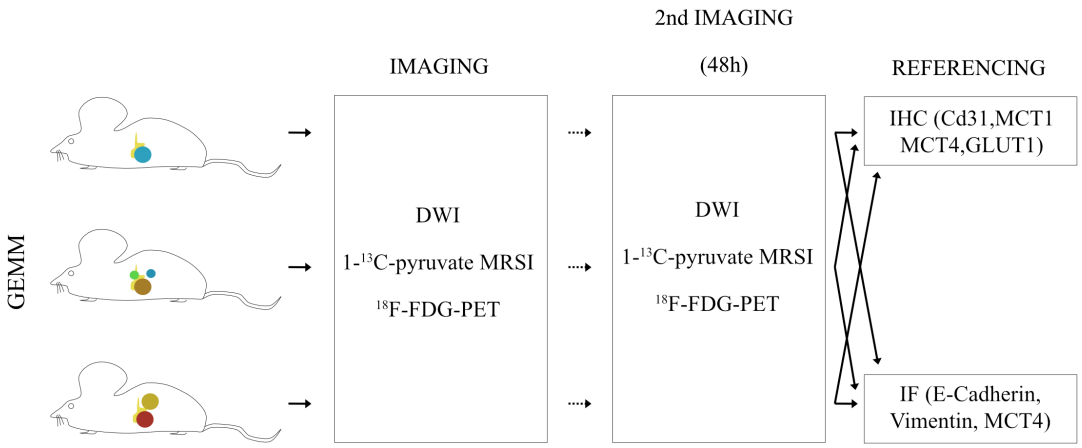

Fig.III-1: Study design of Part One (III.) – the tumors of genetically engineered mice were imaged longitudinally using Diffusion-weighted imaging (DWI), Magnetic resonance spectroscopic imaging with hyperpolarized 1-13C-pyruvate and ^{18}F-FDG PET. These in-vivo findings were validated using immunohistochemistry and cytology stained for markers of vascularization (CD31), of metabolism (MCT1, MCT4, GLUT1) and differentiation (E-Cadherin and Vimentin)

2. Materials & Methods

Chapter 2.1 reveals information about the tumor model and detailed information about the study collective. Chapter 2.2 describes the applied imaging. The Chapters 2.3 and 2.4 explain the methodology of ex-vivo referencing. Image data of these were analyzed using the Image Analysis Tool further described in the Appendix (see VII.4).

2.1 ANIMALS AND TUMOR MODEL

	n_{mice}	$n_{Tumor\ regions}$
DWI		
Endpoint	24	30
Longitudinal 1h	2	2
Longitudinal 24h	1	2
Longitudinal 48h	10	17
Longitudinal 72h	2	6
Hyperpolarized 1-^{13}C-pyruvate MRSI		
Endpoint	24	30
Longitudinal 48h	5	7
^{18}F-FDG PET		
Endpoint	21	57
Longitudinal 48h	2	3
Cell lines	17	35
IHC		
CD31	31	57
MCT4	38	65
MCT1	38	65
GLUT1	36	63
HIF-1-α	18	24
IF (cytology)		
Vimentin	4	4
E-Cadherin	4	4
MCT4	4	4

Table III-1: Study collective

As genetic background mixed C57BL/6/S129 was used. Mice with the following alterations have been included in the experiments:

*(1) CRE-Recombinase under the Ptf1a promoter ($ptf1a^{wt/CRE}$ = **C**)*
*(2) Mutated KRAS with loxed STOP-Sequence ($KRAS^{wt/LSL\text{-}KRASG12D}$ = **K**)*
*(3) Loxed p53 ($TP53^{fl/fl}$ = **P**)*
*(4) TGFaR (EGFR) overexpression (= **T**)*

The mice were held in ZPF-Klinikaustauschraum (Zentrum für Präklinische Forschung, Klinikum rechts der Isar der Technischen Universität München, Ismaningerstr. 22, 81675 München, Bau 557, Raum 1.11). The room accounts for all special needs of animal housing as it was specifically designed for that purpose. It grants access only to authorized personnel. It has a night/day rhythm of 12h and a smooth transition phase and possesses special ventilation and air-conditioning.

The hygiene status of the animals corresponds to an SPF status according to the recommendations of FELASA (Federation of European Laboratory Animal Science Associations) and is reassessed regularly with sentinel animals.

The animals were kept in special single-aerated cages (Tecniplast-IVC). 3-5 mice live together in one cage with an area of 16x37cm^2. The mice were fed ad libidum with autoclaved pellets (No. 1324SP, Fa. Altromin). The mice also received acidified (pH = 3-3.5) water ad libidum with a bottle exchange every week. Special granules (Select Fine, Ssniff) served as bedding and were changed twice a week. For nest-construction autoclaved cellulose was added. In each cage were two houses of red polycarbonate (Bioscape, Otterndorf).

Animal care attendants checked the mice daily. Furthermore mice are weighed at age of 3 weeks and 8 weeks, and then from the start of the experiment on were scored at least once per week. Scoring included weighing, visual inspection of subcutaneous fat, eyes, ears, hygiene and general behaviour of the animal alone and in the group.

All animals were identified by ear markings that were punched during deep narcosis.

2.2 IMAGING

In order to perform imaging, the mice were anesthetized by continuous gaseous infusion of isoflurane (Abbott, Illinois) using a veterinary anaesthesia system (Vapor 2000, Drägerwerk AG&Co. KGaA, Lübeck, Germany). Anaesthesia was introduced with 5% and sustained with 2% gaseous infusion of isoflurane with 1.5-2 L Oxygene. During anaesthesia, the temperature of the mice was monitored. To prevent hypothermia, mice were placed on to a heating mat. During imaging a special heater ensured stable temperatures of the animals.

The protocol includes weighing of mouse, glucose measurements before and after the scan, continuous temperature and breathing measurements and adaptation of isoflurane concentrations during the imaging. The animal's eyes were protected through application of eye ointment. Before the imaging mice were laid in prone position.

Special positioning was necessary to yield imaging with little noise and enable transport from the PET facility to the 7T preclinical MRI scanner. Mice were laid into a mouse bed with the attached isoflurane tube, thermometer, breathing patch and ^{13}C-urea phantom (see Fig. III-2). For transport this mouse bed could be placed into a special transport tube, flooded with isoflurane, which allowed transport and direct insertion into the MRI scanner, minimizing movement of the abdominal region of the mouse. Thereby PET could be correlated to T_2-weighted imaging data.

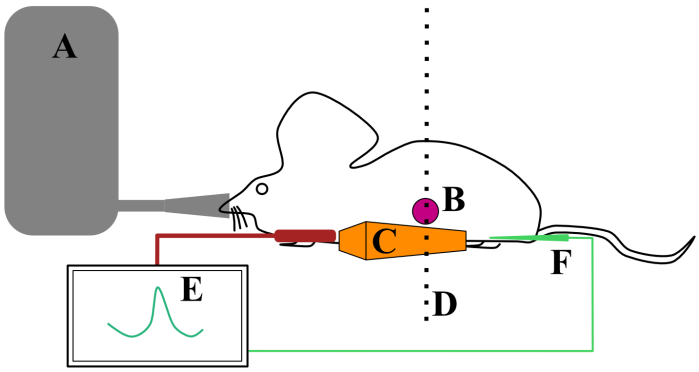

*Fig.III-2: Mouse setup illustration showing (**A**) isoflurane 2% (**B**) abdominal tumor mass (**C**) 1-^{13}C-urea phantom (**D**) desired imaging slice and (**E**) breathing patch connected to monitor (**F**) thermometer connected to monitor.*

MRI experiments were performed at 7T MRT (BioSpec) by Bruker (Billerica, MA) located in the department of nuclear medicine of Klinikum rechts der Isar (Munich, Germany) using a small ^{1}H/^{13}C volume receiver coil (31mm ID) by RAPID Biomedical GmbH (Rimpar, Germany).

Axial T2-weighted (T_2w) TSE was performed for tumor detection and detailed planning of Diffusion-weighted (DWI) and hyperpolarized 1-^{13}C-pyruvate MRSI. All parameters for this and following sequences are summarized in the Table III-2.

DWI was performed during free breathing with low breathing frequencies of 30-50 min^{-1} and temperatures above 37°C. ADC-Maps were calculated using MATLAB (R2018b) by MathWorks, Inc. (Natick, MA). Further Analysis of the before calculated ADC Maps was performed using HOROS.

To achieve signal enhancement of hyperpolarized 1-^{13}C-pyruvate in solution for 1-^{13}C-pyruvate MRSI experiments a HyperSense Dynamic Nuclear Polarizer by Oxford Instruments (Abingdon, England) was used. The 1-^{13}C-pyruvate-sample consists of 1-^{13}C-pyruvate, Dotarem and a stable radical by Sigma Aldrich (St. Louis, MO). 1-^{13}C-pyruvate MRSI was performed with low breathing frequencies of 30-50 min^{-1} and temperatures above 37°C. Dynamic scans were performed with measuring timepoints of 5s-6s and a Flip Angle of 5°. Reference Power was calibrated every time (0.275-0.325W) using a ^{13}C-urea phantom, which was placed in line with the abdominal tumor mass. The scans were analyzed using MATLAB (R2018b) by MathWorks, Inc. (Natick, MA) and a previously published methodology (Hill, Orton et al. 2013).

	T_2-weighted MRI technical data (Scout/Planning)	DWI technical data	1-^{13}C-pyruvate MRSI technical data
Resolution [mm^2]	0.250x0.250 / 0.133x0.133	0.250x0.250	3x3
Number of slices	35/9-15	9-15	1
Slice thickness [mm]	1/1	1	3
TE [ms]	48/48	38.59	1.101
TR [s]	4/4	5	44.643
Averages	2/4	1	1
Repetitions	1/1	10	42
Bandwidth [Hz]		$1*10^5$	2000
Flip Angle [°]	90/90	90	5
b-values [s/mm^2]	-	12.37; 112.78; 215.04; 316.77; 418.24; 519.52; 620.69; 721.76; 822.75; 1024.58; 1226.22; 1528.45	-

Table III-2: Technical data of MRI imaging experiments

PET measurements were performed on Inveon PET-CT by Siemens (Munich, Germany) located in the department of nuclear medicine of Klinikum rechts der Isar (Munich, Germany). The injected tracer had an activity of 10-13 MBq. Static PET was performed with breathing frequencies of 30-40 min^{-1} and temperatures above 35° for 15 minutes after 45 min of uptake in sleep. Mice were starved for 1h prior imaging. Data was reconstructed using the OSEM 3D algorithm. Sybille Reder and Markus Mittelhäuser performed the PET experiments.

Regions of interest (ROI) were drawn manually on delineable tumor regions. ROI size ranged from 2 to 30 mm^2 and no correlation was noted between size of ROI and PDAC group. All ROIs were manually defined based on visible tumor borders and quality of imaging data. Histologically confirmed areas of necrosis or tumor areas influenced by partial volume effects were excluded from all imaging analyses. Imaging and corresponding histology ROIs were correlated slice based for every

tumor region. In animals with several slices of the same tumor subtype, the central tumor slice was chosen.

The study for the longitudinal sample was implemented as depicted in Fig.III-3. After 48 hours the second imaging was performed including ^{18}F-FDG PET. After the imaging dissection of the mice and sampling of the tumors was performed. In some cases longitudinal imaging was performed in a 24h to 72h time frame, the protocol was implemented identically; data is represented accordingly.

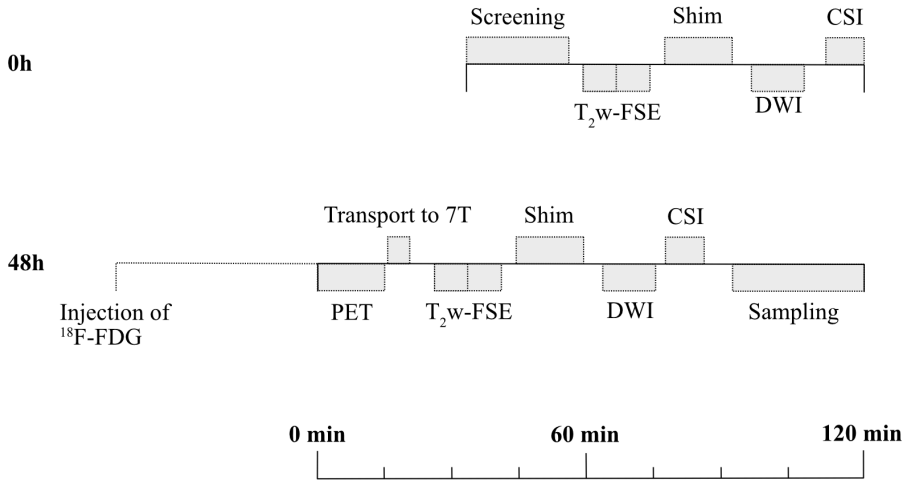

Fig.III-3: Schedule of longitudinal study protocol

2.3 IMMUNOHISTOCHEMISTRY

Murine PDAC tissue samples were fixed in 4% PFA/PBS solution, dehydrated and paraffin-embedded (FFPE) according to the standard pathology core conditions of Technical University of Munich. FFPE slices of 2-4 µm were stained with Mayer's haemalaun and eosin (H&E), according to a standard protocol for tissue visualization.

For immunohistochemical (IHC) stainings slides were sent to the Pathology department of the Technical University of Munich and stained in the laboratory of PD Dr. Katja Steiger. FFPE slices were pretreated 30 min with citrate buffer pH=6.0 and stained with antibodies against GLUT1 (rabbit, ab 115730, 1:750, Abcam, USA), MCT1 (rabbit, ab 85021, 1:1500, Abcam, USA) and MCT4 (rabbit, sc-50329, 1:150 for mPDAC, mouse sc-376140 1:150 for hPDAC, Santa Cruz Biotechnologies, USA) on a Bond RXm system (Leica Biosystems, Wetzlar, Germany). Antibody binding was detected using DAB as chromogen after pre-incubation with respectively Bond Polymer Refine Detection Kit (Leica). Nuclei were counterstained with haemalaun. All slides were digitalized using Aperio Scanner

(Leica). Analysis of IHC intensity was carried out using Aperio Image viewer (Leica), Aperio positive pixel count algorithm (Version 9) and our new in-house IAT (see VII.4). ROIs for analysis were drawn after co-registration with imaging data and identification of respective regions on the histologic slides as demonstrated in Fig.V-3 (Average ROI size ± SD [mm^2] = 11 ± 6). A Color Saturation Thresholding (CST) method was used for all slides of each staining (CST_{GLUT1} = 0.20, CST_{MCT4} = 0.17, CST_{MCT1} = 0.10) where signals above CST were counted. Final values were normalized to the area (($N_{pixels>CST}$ /N_{pixels})×100 = stained area [%]).

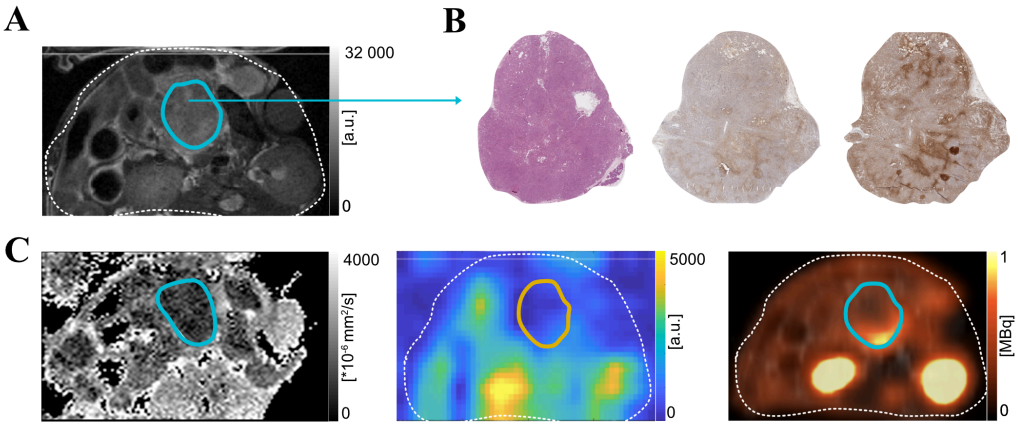

*Fig.III-4: Imaging data and corresponding histology (**A**) T_2-weighted planning scan (**B**) From left to right H.E., MCT4, GLUT1 stained histology (**C**) From left to right - DWI, 1-^{13}C-pyruvate MRSI, ^{18}F-FDG PET*

2.4 Cytology

Primary pancreatic tumor cells were isolated from 4 tumors after the endpoint imaging, by studious cutout of the tumor tissue and culturing of it under standard conditions. The isolated murine PDAC cells were cultured in high glucose Dulbecco's Modified Eagle Medium (DMEM, Thermo Fisher Scientific, Waltham, USA) supplemented with 10% fetal bovine serum (FBS, Thermo Fisher Scientific, Waltham, USA) and 1% Penicillin/Streptomycin (P/S, Thermo Fisher Scientific, Waltham, USA). For immunofluorescence (IF) staining, cells were cultured in DMEM supplemented with 5mM D-glucose (Thermo Fisher Scientific, Waltham, USA), 2 mM L-glutamine (Sigma-Aldrich, St. Louis, USA) and 5% FBS for 48h prior experiments.

For immunofluorescence (IF) staining, cells were washed and fixed for 10 min at RT using 4% PFA, treated with 0.15% glycine for 5 min, permeabilized with 0.2% Triton-X 100 in PBS. After washing, cells were blocked for 1.5 h in 10% donkey serum and 0.1% BSA diluted in PBS. The primary antibodies were incubated overnight at 4°C in 0.1% BSA diluted in PBS Anti-CDH1 (1:200, AF748,

R&D Systems), Anti-Vimentin (1:50, MAB2105, R&D Systems), Anti-MCT4 (1:100, rabbit, sc-50329, Santa Cruz Biotechnology). After washing, the secondary antibodies were incubated for 2.5 h at RT in the dark (donkey anti-goat AF488, donkey anti-rat AF594, donkey anti-rat AF680, 1:250, Invitrogen). Thereafter, cells were treated for 2 min with DAPI, washed and mounted. Slides were kept at 4°C until further analysis using the Leica TCS SP8 Confocal Microscope (Leica). The immunofluorescence staining was performed by Katja Peschke. Analysis of immunofluorescence intensity was carried out on six randomly selected images of each cell line (on average including 117 ± 71 cells) using our in-house script for MATLAB (R2018b) by MathWorks, Inc. (Natick, MA). Signal intensities of Vimentin, E-Cadherin and MCT4 stainings were referenced to DAPI signal intensity. Cell count was determined via threshold segmentation (see IV.2.3, Fig.IV-2, Fig.IV-3).

2.5 Statistical Methods

Statistical analysis was performed in GraphPad Prism (version 7 and 8, GraphPad Software Inc., San Diego, CA). For all statistical tests, a level of significance of 5% was used. A two-sided Student's t-test was performed for group comparisons of normally distributed quantities. All datasets with sample size below 10 were considered normally distributed. The strength of association between quantitative measures was assessed by Pearson's (r, normally distributed data) correlation coefficient. Data presented as mean values including standard deviation or 95% confidence interval (95%-CI).

3. Results

The presentation of results is structured in order to answer the following questions:

- In which way do determinants such as cellularity, stroma and perfusion influence metabolic imaging in endogenous mPDAC? (see III.3.1 – III.3.3)
- Are MCT4 and GLUT1 relevant markers for tumor stratification in endogenous mPDAC? (see III.3.3)

In order to contemplate these questions, the results are discussed further in chapter 4 (*Discussion*).

3.1 Multiparametric Endpoint Imaging of endogenous mPDAC

Diffusion-weighted imaging displayed tumors with heterogeneous diffusion restriction and was capable of predicting tumor cellularity accurately (Mean ADC $PDAC^{low}$ = 1601 ± 53, Mean ADC $PDAC^{high}$ = 1306 ± 93, $p < 0.001$, see Fig.III-5 B). The AUC_l/AUC_p correlated significantly with these subgroups (Mean AUC_l/AUC_p $PDAC^{low}$ = 0.491 ± 0.120, Mean AUC_l/AUC_p $PDAC^{high}$ = 0.798 ± 0.3365, $p = 0.010$, see Fig.III-5 C). However this could not be seen in the metabolic data derived from PET (Mean SUV_{mean} $PDAC^{low}$ = 1.930 ± 0.731, Mean SUV_{mean} $PDAC^{high}$ = 2.090 ± 0.576, $p = 0.373$, see Fig.III-5 D).

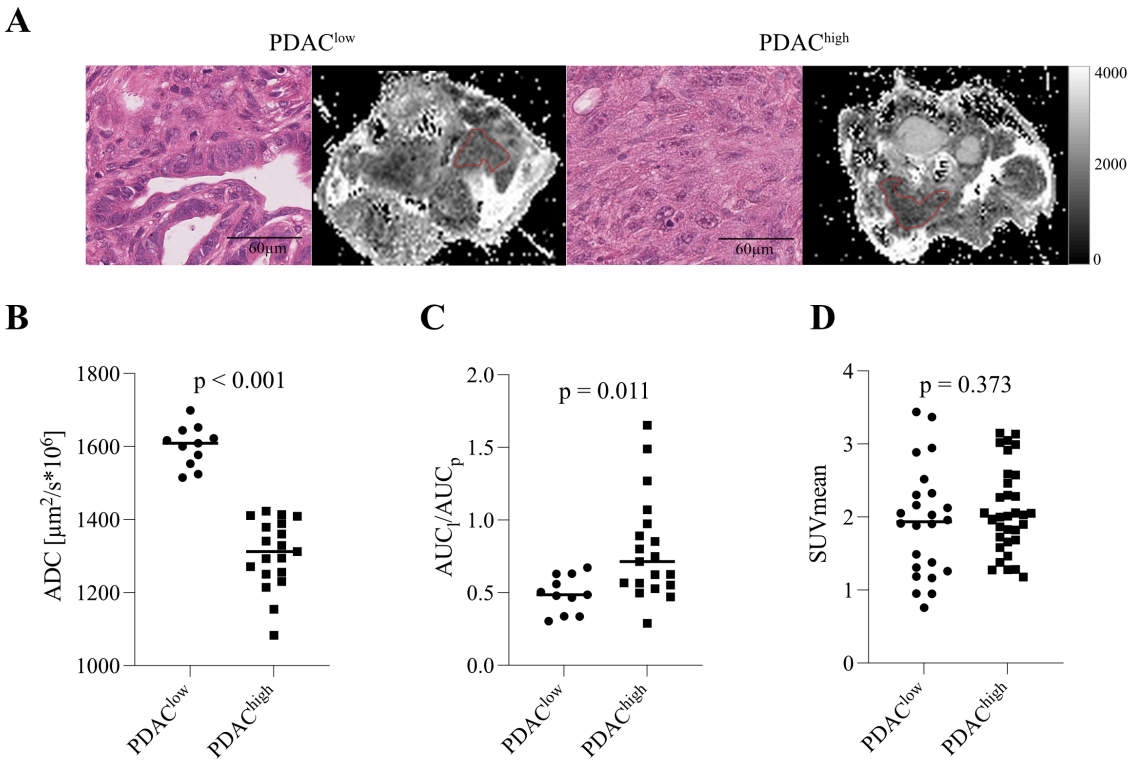

Fig.III-5: Endpoint Imaging: ***(A)*** *Tumors with low ($PDAC^{low}$) and high cellularity ($PDAC^{high}$) with H.E. stained histology (left) and corresponding ADC-Map (right)* ***(B)*** *ADC in relation to tumor cellularity* ***(C)*** *AUC_l/AUC_p in relation to tumor cellularity* ***(D)*** *SUV_{mean} in relation to tumor cellularity*

The two subgroups differed in the suggestive inflow/perfusion marker 1-^{13}C-pyruvate maximum signal intensity (Mean pyruvate-peak-intensity $PDAC^{low}$ = 14714 ± 6712, Mean pyruvate-peak-intensity $PDAC^{high}$ = 8688 ± 4578, $p = 0.0374$) with highly cellular tumors displaying lower 1-^{13}C-

pyruvate signal intensities. However, no association between CD31 staining and $PDAC^{low}$ and $PDAC^{high}$ was observed (CD31 $PDAC^{low}$ = 8.35 ± 2.24, CD31 $PDAC^{high}$ = 7.02 ± 2.52, p = 0.503).

Correlating the ADC with the AUC_l/AUC_p, *outliers* were identified. Five tumors showed a higher AUC_l/AUC_p ("*overperformers*") and 5 tumors showed a lower AUC_l/AUC_p ("*underperformers*") than the main trend observed in other tumors and their respective ADC value (defined by the 95%CI in highly cellular tumors, see Fig.III-6 A). Among the group of underperformers are two tumors that showed mucinous differentiation whereas growth patterns in the overperforming group were mainly dense cellular growth. Furthermore, we could observe a marked trend that tumors of the overperforming group showed lower pyruvate AUC (Mean AUC_p Underperformer = 36121 ± 9506, Mean AUC_p Overperformer = 20070 ± 12336, p = 0.073) and higher areal MCT4 expression (Mean MCT4 Underperformer = 6.33 ± 3.39, Mean MCT4 Overperformer = 13.25 ± 5.49, p = 0.165, see Fig.III-6 B) and areal GLUT1 expression (Mean GLUT1 Underperformer = 13.33 ± 11.8, Mean GLUT1 Overperformer = 29.50 ± 8.29, p = 0.132, see Fig.III-6 C).

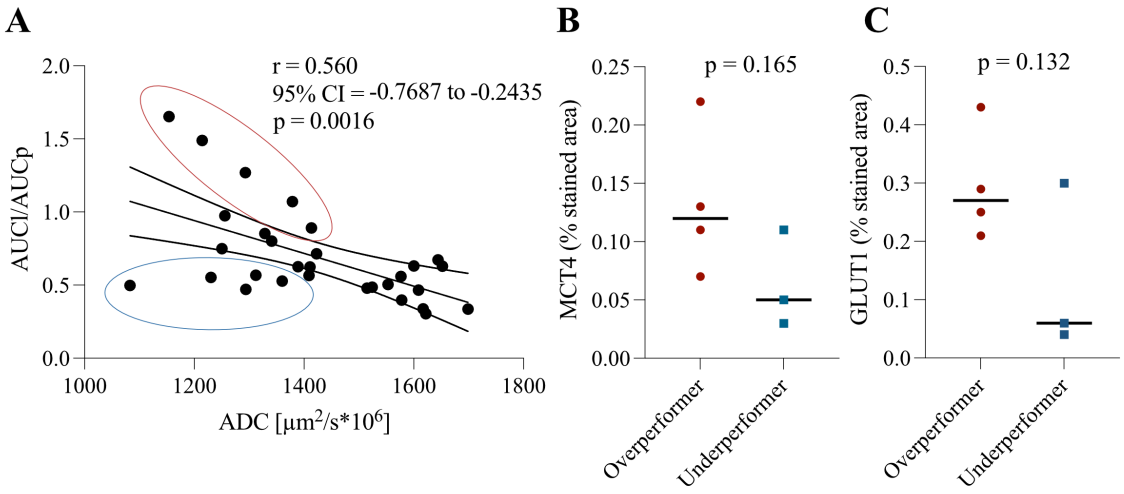

Fig.III-6: Decoupling cellularity from metabolic imaging results ***(A)*** *Correlation of ADC and respective* AUC_l/AUC_p ***(B)*** *Areal MCT4 expression in Over- and Underperformers* ***(C)*** *Areal GLUT1 expression in Over- and Underperformers*

3.2 Immunohistochemical biomarker expression of endogenous mPDAC referenced with endpoint imaging

As described in 3.1 no significant connection between tumor cellularity and vascular tissue biomarker CD31 expression was found. Furthermore, there was no distinct coherent pattern of vessel distribution observed that could be assigned to cellularity or tumor subtype.

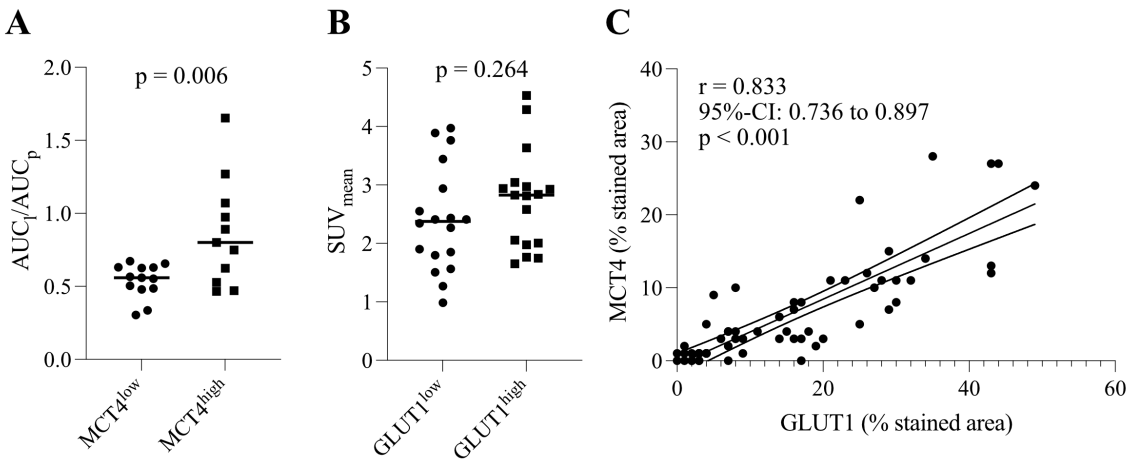

Fig.III-7: Immunohistochemical expression of metabolically relevant biomarkers in endogenous mPDAC ***(A)*** *AUC_l/AUC_p in tumors with low ($MCT4^{low}$) and high ($MCT4^{high}$) MCT4 expression* ***(B)*** *SUV_{mean} of ^{18}F-FDG in tumors with low ($GLUT1^{low}$) and high ($GLUT1^{high}$) GLUT1 expression* ***(C)*** *Correlation of areal GLUT1 and MCT4 expression*

The areal expression of MCT4 (r = 0.727, 95%-CI = 0.458 - 0.874, p < 0.001) as well as the areal expression of GLUT1 (r = 0.621, 95%-CI = 0.246 -0.834, p = 0.004) were correlated to the AUC_l/AUC_p. Thereby the AUC_l/AUC_p is reliable in differentiating the two phenotypes $MCT4^{low}$ and $MCT4^{high}$ (Mean AUC_l/AUC_p $MCT4^{low}$ = 0.538 ± 0.111, Mean AUC_l/AUC_p $MCT4^{high}$ = 0.863 ± 0.349, p = 0.006, see Fig.III-7). These mimic the metabolic phenotype found in epithelial and mesenchymal cell lines in the orthotopic model. Furthermore, the expression of GLUT1 and MCT4 is linked quantitatively in the whole tumor (r = 0.833, 95%-CI = 0.736 – 0.897, p < 0.001, see Fig.III-7 C) as well as in its intratumoral distribution (see Fig.III-8 A). Interestingly, MCT4 expression was not exclusively observed in tumor cells but also in stroma cells (see Fig.III-8 B). Stromal expression levels of MCT4 were not directly connected to tumor cell expression. Some tumors were observed in which the mainly ductal tumors cells were MCT4 negative and stromal expression of MCT4 was present, mainly surrounding the ductal structures. Furthermore, also tumors with high tumor cell expression of MCT4 were found in which stroma was classified as MCT4 negative. These circumstances seemed to have no relevant influence on AUC_l/AUC_p as stromal positive tumors were distributed amongst $MCT4^{low}$ and $MCT4^{high}$ equally, with low and high production of lactate in the hyperpolarized 1-^{13}C-pyruvate MRSI. Additionally, areal MCT4 expression was linked to diffusion restriction measured with the ADC (r = -0.615; 95%-CI: -0.816 to -0.282; p= 0.001) indicative of tumor cellularity.

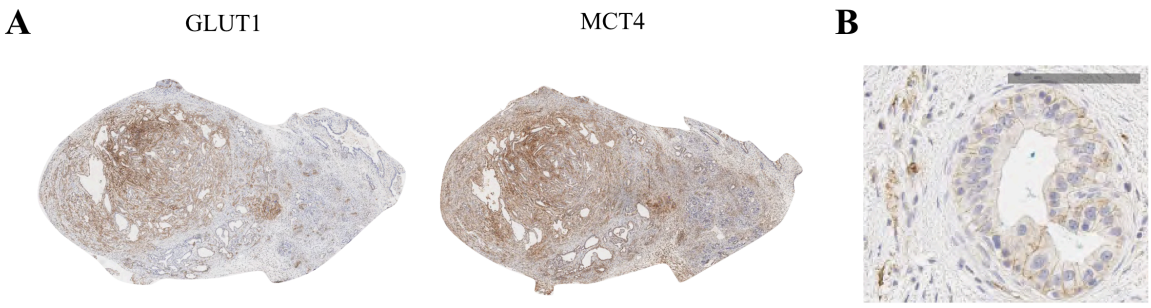

Fig.III-8: Intratumoral distribution and stromal expression of GLUT1 and MCT4 ***(A)*** *Intratumoral distribution of GLUT1 (right) and MCT4 (left) expression* ***(B)*** *Exemplary image of stromal MCT4 expression (grey scale bar = 100µm)*

As observed in chapter 3.1 outliers have been identified: Tumors with rather low cellularity and high AUC_l/AUC_p (titled "overperformers") and tumors with a relatively high ADC for their comparably low AUC_l/AUC_p (titled "underperformers").

Interestingly, PET derived parameters such as SUV_{mean} (but also SUV_{max}, Tumor/Liver, Tumor/Muscle and Tumor/Kidney) showed no correlation with areal expression of GLUT1 (r = 0.108, 95%-CI = -0.233 – 0.426, p = 0.5354).

Referencing metabolic data quantitatively with information on tumor cellularity via ADC or apparent tumor perfusion via hyperpolarized 1-^{13}C-pyruvate signal intensities or 1-^{13}C-pyruvate time-to-peak did not yield better representation of metabolic tissue markers (MCT4 and GLUT1). Moreover, an association of MCT1 expression and CD31 was not observed in this tumor model.

3.3 Immunofluorescence cytology derived from endogenous mPDAC

Four cell lines from the endogenous tumors were established and stained for their E-Cadherin, Vimentin and MCT4 expression. These four cell lines were not chosen at random; but from each subgroup ($PDAC^{low}$ and $PDAC^{high}$) two cell lines were selected that showed vastly different behavior in metabolic imaging (see Fig.III-9 A). Conclusively, one cell line from $PDAC^{low}$ showing little AUC_l/AUC_p and one cell line showing high AUC_l/AUC_p were chosen. The same was repeated for $PDAC^{high}$ tumors. In culture these cells showed a similar metabolic behavior as their primaries. Cell lines with comparably high AUC_l/AUC_p also displayed high MCT4 and Vimentin expression (see Fig.III-9 D-F). MCT4 and Vimentin correlated very well in all analyzed cell cultures (r = 0.817; 95%-CI: 0.644 to 0.911; $p < 0.001$). Interestingly, the cell lines of high Vimentin and MCT4 expression also showed higher E-Cadherin expression (see Fig.III-9 D-F). Cells from tumors that had higher

AUC_l/AUC_p ratios than their subtype counterpart also exhibited higher Vimentin (Mean Vimentin/DAPI: 3.580 and 3.049 vs. 1.911 and 1.799) and MCT4 expression (Mean MCT4/DAPI: 6.770 and 4.722 vs. 4.230 and 3.505).

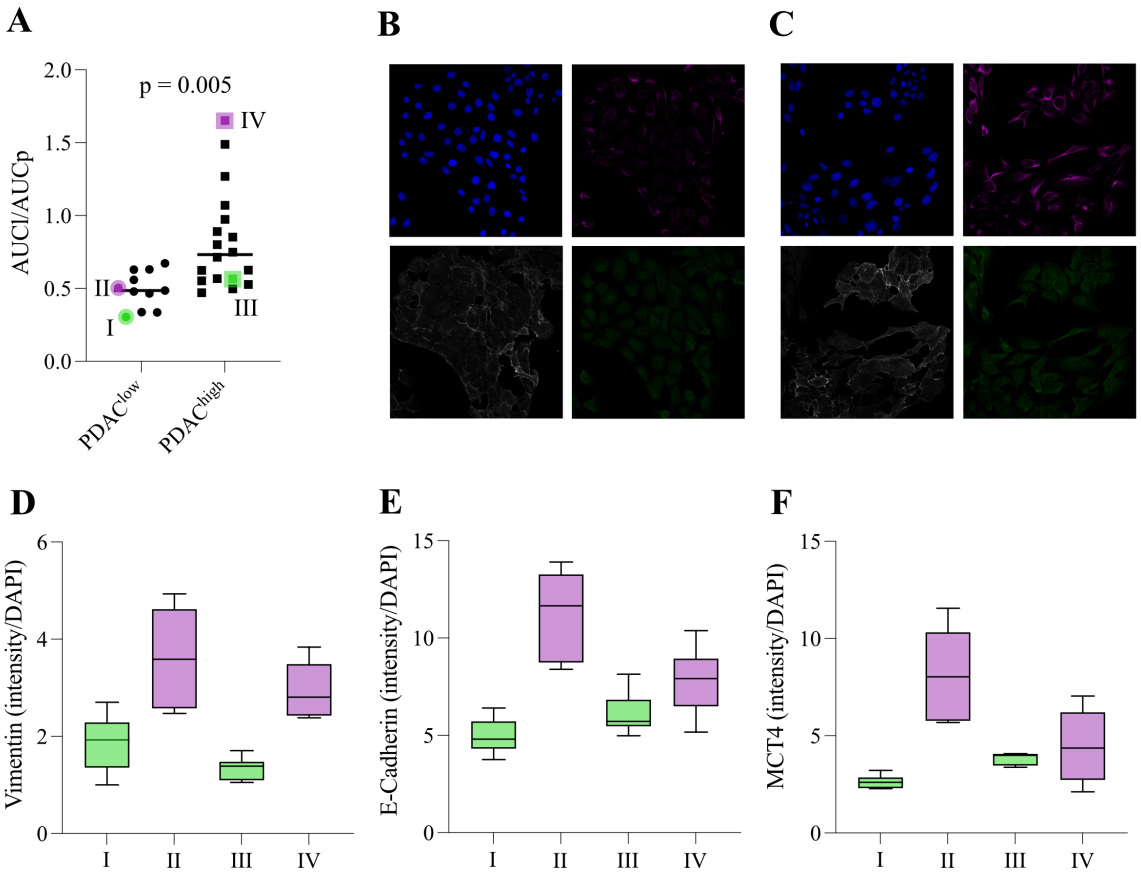

Fig.III-9: Expression patterns of cytology derived from endogenous mPDAC ***(A)*** *Explanatory plot of the origin/primaries of the cell lines (****B/C****) Respective biomarker expression (upper left = DAPI, upper right = Vimentin, lower left = E-Cadherin, lower right = MCT4) of* ***(B)*** *cell line I* ***(C)*** *cell line IV* ***(D)*** *Vimentin expression in I-IV* ***(E)*** *E-Cadherin expression in I-IV* ***(F)*** *MCT4 expression in I-IV*

4. Discussion

In this part a multimodal imaging protocol – including structural and metabolic imaging – was established and proven to be useful for the longitudinal tumor characterization.

Vast intra- and intertumoral heterogeneity was observed using different methods: DWI revealed significant microstructural differences and exhibited a wide range of detected ADC values observed in mPDAC. These findings obtained on the 7T Scanner with a substantially higher amount of b-values (3 at 1.5T and 15 at 7T) correlate well to our previous studies in endogenous mPDAC and confirm the

comparability of methods (Trajkovic-Arsic, Heid et al. 2017). Hyperpolarized 1-^{13}C-pyruvate MRSI revealed differing metabolic patterns ranging from low to very high lactate production and revealed an association to tumor cellularity. Similarly, also ^{18}F-FDG PET showed very heterogeneous metabolic inclines of the observed tumors. The high intra- and intertumoral heterogeneity was confirmed by histology, IHC and IF cytology. The mere existence of this vast diversity in tumors stemming from a GEMM is supportive of the similarities between the endogenous mPDAC model and human PDAC where heterogeneity is one of the main defining properties (Daemen, Peterson et al. 2015, Bailey, Chang et al. 2016). This supports a high translational value of this study and used model.

The strong association between ADC values and cellularity in PDAC was already reported in literature for this model (Heid, Steiger et al. 2017). The hypothesis behind it – dense cellular growth hindering free isotropic diffusion – is further supported by the observation that the intracellular compartment that does only marginally contribute to the $ADC_{12\text{-}1528}$ is proportionally more distinctive in more cellular tumors. Also the AUC_l/AUC_p is correlated to cellularity with highly cellular tumors showing more lactate production. This is consistent with observations made in related tumor entities and modalities (Hundshammer, Braeuer et al. 2018, Gallagher, Woitek et al. 2020). It is consistent with the hypothesis that increasing metabolic dysregulation and hypoxic conditions progress with tumor development – as cellularity does (see VII.5.3, Fig.VII-11) – and both are highly interconnected. As the signal of hyperpolarized 1-^{13}C-pyruvate decays with the T_1, it can only service fast measurements that are then dependent on perfusion within these two minutes. This is further supported by the observation that highly cellular tumors showed lower signal intensities of 1-^{13}C-pyruvate indicating lower perfusion. The missing confirmation of this in CD31 stained histology can have various reasons: First, the tissue was not perfusion fixed – therefore, exact interpretation of vessel sizes is not possible. Secondly, the CD31 positive pixel count is assumed as a proportional parameter to vessel size but as the area of a round vessel is calculated by the squared radius of it, small vessels – which are more often observed in parts of the tumor with ongoing active angiogenesis – can have a disproportionally high influence on the CD31 PPC.

As the tie between cellularity and AUC_l/AUC_p is intriguing, the Over- and Underperformers (see III.3.1, Fig.III-6) were identified. Compared to their respective ADC, they had AUC_l/AUC_p values that could not be explained merely by their cellularity. Therefore, either metabolism or perfusion could be a major influencing factor. That these tumors indeed differ in their metabolic phenotype was supported by different MCT4 expression patterns; the Overperformers also showed higher MCT4 expression. However, it is to note that the PPC and thereby calculated stained area of MCT4 staining is by its nature a parameter that is influenced by tumor cell density as the expression is not exclusively but mainly found in tumor cells. That is why a good overlap between areal MCT4 and AUC_l/AUC_p is still observed. In summary, our study indicates that multimodal/multiparametric imaging may be necessary to characterize and stratify PDAC correctly.

Moreover, our observations also position the AUC_l/AUC_p as a potentially valuable biomarker as it is the areal MCT4 expression that is associated with worse survival and quasi-mesenchymal subtype in human PDAC (Baek, Tse et al. 2014). That is why the circumstance that these tumors did not receive a ^{18}F-FDG PET scan is a limiting factor to the significance of that thought. The mere normalization of AUC_l/AUC_p with ADC values did not produce such a clear possibility of characterization. That could be attributed to a non-linear relationship between cellularity and AUC_l/AUC_p as well as a changing weighting of cellularity, metabolism and perfusion in different subtypes and stages of progressing disease.

In literature increasing evidence is found that MCT4 has disease-defining characteristics beyond increasing glycolytic flux (Kong, Nøhr-Nielsen et al. 2016, Lee, Hwang et al. 2021). Also in human PDAC, it is associated with a quasimesenchymal subtype, tumor invasiveness and worse survival. Therefore, the characterization of tumors into $MCT4^{low}$ and $MCT4^{high}$ is pathophysiologically justified. The good correlation of AUC_l/AUC_p to areal expression of MCT4 and GLUT1 is in part due to their dependence on cellularity.

This might explain why the SUV_{mean}/SUV_{max} of ^{18}F-FDG are not correlated with these parameters even though GLUT1 is functionally coupled to them. In literature this independence of PET derived parameters and cellularity has been described in human PDAC (Higashi, Tamaki et al. 1998, Tanimoto, Yoshikawa et al. 2010). As proposed in literature and supported by the results, MCT1 plays a secondary role as a relevant biomarker in PDAC (Kong, Nøhr-Nielsen et al. 2016).

The four cell lines mimicked the metabolic expression patterns of the primary tumors well. Also the association of Vimentin and MCT4 could be seen as a hint to its relevance in tumor cell transformation. Interestingly, in this endogenous model both were associated with E-Cadherin expression. To my knowledge, this has not been described before for this model and is therefore noteworthy as it contradicts observations in similar models (Wang, Dong et al. 2018). As E-Cadherin and Vimentin are generally attributed to the two differing subtypes of epithelial and quasimesenchymal tumors respectively, the biological relevance of this does not become clear from this experiment and requires further investigation.

The good correlation between IHC and results from IF cytology already suggests a certain metabolic stability of the tumor cells. That this is also true for PDAC in-vivo was reassured by stable metabolic measurements. This can be seen as a confirmation that the 1-^{13}C-pyruvate MRSI measurement is repeatable in vivo and no severe metabolic changes are expected during a time frame of 48 hours if no relevant changes in animal physiology are observed (see VII.5.3, Fig.VII-12). This may be regarded as an encouraging result for further therapy studies aiming to use metabolic data for therapy response monitoring or direct pharmacodynamic monitoring in case a direct metabolic inhibitor is used. This is relevant as pyruvate metabolism can be significantly altered following therapy (Aggarwal, Vigneron et

al. 2017, Michel, Zieliński et al. 2019). Moreover, 1-^{13}Cpyruvate MRSI is able to detect the Warburg shift, whereas ^{18}F-FDG PET may only detect increased glycolytic flux decoupled of its origin (Gutte, Hansen et al. 2015) – a valuable property that may be exploited.

5. CONCLUSION

Conclusively, this study demonstrated the establishment and feasibility of a reproducible micro-structural and metabolic imaging platform for endogenous murine PDAC. A high heterogeneity was observed as an inherent property of PDAC that poses large challenges to imaging and ultimately individualized therapy, but confirms the clinical relevance of the characterized animal model. As the placement of the AUC_l/AUC_p in the field of available biomarkers (see Fig.VII-20) was described in this work, it can be seen as a step to metabolic characterization of therapy response in different tumor subtypes and therefore individualized approaches. However, due to the strong dependency of the tumor biology on tumor cellularity, we propose to use metabolic imaging in combination with structural imaging methods.

IV. PART TWO: COMPREHENSIVE MORPHOLOGICAL CHARACTERIZATION AND QUANTIFICATION OF NUCLEAR PROPERTIES IN MPDAC AND THEIR TIES TO BIOMARKER EXPRESSION

1. INTRODUCTION

Evaluation of tumor cell nuclei is an integral part of cytological and histopathological examination. As nuclear atypia are indicative of malignant lesions, nuclear descriptors such as nuclear size, shape and heterogeneity are evaluated. Nevertheless, intra- and inter-observer variability remain problematic and potentially biologically meaningful information is lost when relying solely on qualitative assessment. In order to find nuclear morphologic parameters, nuclear segmentation in cytology and histopathologic slides is to be implemented: Doing this, threshold based techniques remain the most prevalent but are prone to under-segmentation of clustered nuclei. Therefore, they are often combined with *seed*-based analysis (Xu, Lu et al. 2017, Zhao, An et al. 2017). Nevertheless, nuclear segmentation remains difficult, especially with the goal of morphologic description as these separation techniques impact the afterwards measured nuclear morphology (see Fig.IV-1).

In this study a novel approach to nuclear segmentation is assessed, as morphologic characterization is dependent on morphologic preservation of nuclei during the segmentation process. Previously described techniques (including watershed and line of sight based segmentation) distort nuclear morphology because should nuclei overlap, the overlapping area is only attributed to one nucleus. Thereby parts of the other nuclei (or nucleus) in that respective cluster are cut out (see Fig.IV-1). That is why this study aims at improved morphologic preservation through a novel segmentation algorithm.

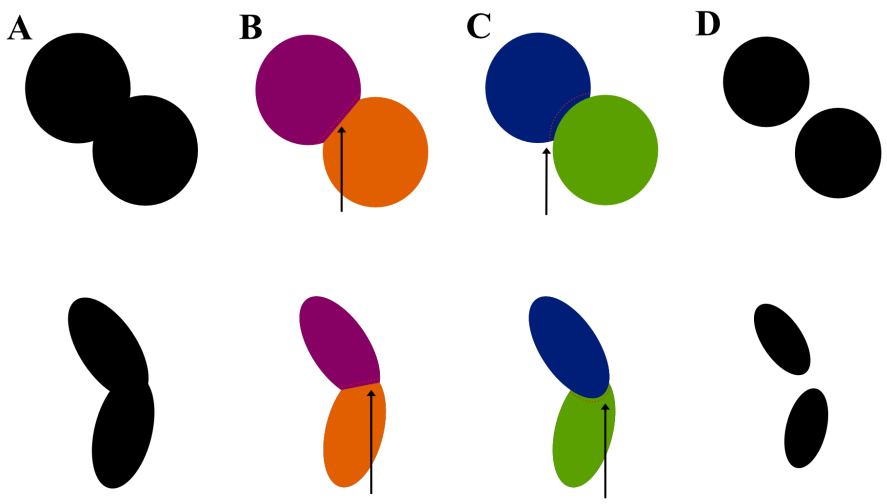

Fig.IV-1: Illustration of lacking morphological preservation of nuclei in common segmentation methodology ***(A)*** *Bw-image of overlapping circles (illustration of nuclei)* ***(B)*** *Segmentation results using a watershed algorithm (arrow indicates morphologic loss)* ***(C)*** *Segmentation results using a line of sight algorithm (arrow indicates morphologic loss)* ***(D)*** *Segmentation result using the algorithm proposed in this study – morphologic shape preservation with proportional reduction of nuclear area*

Successful nuclear segmentation allows for selective extraction of nuclear features. In biological image processing, biological relevance in different models has been attributed to histogram-derived parameters such as Mean, SD, Kurtosis, Skewness and morphologic descriptors such as nuclear Area, nuclear Eccentricity and nuclear Solidity. After the description of Grey-level-co-occurrence matrix (GLCM) derived texture parameters by Haralick et al. in 1973 (e.g. Contrast, Correlation, Energy and Homogeneity), they also have been added to the catalogue of important descriptors in biological image processing and their role has been evaluated in numerous studies (Jørgensen, Yogesan et al. 1996, Gupta, Gupta et al. 2010). In this protocol, these parameters are used to characterize nuclei in different disease models including cytology and histopathology slides of murine PDAC. These features are then used to assess the ties of nuclei characteristics to relevant biomarkers in PDAC that have been introduced above.

In Part One (III.), monocarboxylate transporter 4 (MCT4) has been described as a relevant metabolic biomarker in mPDAC. The expression of MCT4 was correlated to cellular metabolism and cellularity and thereby subtypes. Furthermore, MCT4 seems to play an important role in PDAC cancer cell migration as its inhibition/knockdown reduces invasiveness (Kong, Nøhr-Nielsen et al. 2016). Generally, the role of MCT4 for the occurring metabolic shift in PDAC is assumed greater than the one of MCT1 (Kong, Nøhr-Nielsen et al. 2016, Sukeda, Nakamura et al. 2019). MCT4 is also being evaluated as a metabolic therapeutic target in prostate cancer (Choi, Xue et al. 2016). The importance

of MCT4 for metabolic imaging such as 1-^{13}Cpyruvate MRSI has been investigated and confirmed in related tumor entities such as prostate and breast cancer (Gallagher, Woitek et al. 2020).

In this part of the work, the role of tissue biomarkers of PDAC (MCT4, GLUT1 and KRT81) were evaluated using murine PDAC cytology and histopathology. The patterns of biomarker expression were then evaluated regarding pertinent nuclear characteristics.

2. Materials & Methods

The study is descriptive and retrospective in terms of case selection. It involves different tumor models (orthotopically implanted and endogenously grown mPDAC) and several modalities (cytology + histology (H.E. & IHC stainings)). The following *Materials & Methods* section mainly focuses on performed procedures on these existing data sets. The image analysis workflow introduced starting from 2.3 is novel and therefore described in detail in this chapter.

2.1 Study Collective

The murine probes were collected during the imaging experiments partially described in Part One (III.). Four cell lines used for orthotopically implanted mPDAC (2 characterized as epithelial, 2 characterized as mesenchymal (Mueller, Engleitner et al. 2018)) and four cell lines derived from endogenously grown mPDAC (2 from tumors characterized by in-vivo imaging as highly glycolytic, 2 from tumors characterized by in-vivo imaging with signs of low glycolysis) were included in the study. Seven orthotopically-implanted tumors (3 epithelial, 4 mesenchymal) were extracted and H.E./IHC (MCT1, MCT4, GLUT1, CD31) stained.

2.2 Murine cytology (orthotopic & endogenous)

Primary pancreatic tumor cells were isolated from 4 GEMM: CK tumors in the Lab of Dieter Saur (2 epithelial, 2 mesenchymal) (Mueller, Engleitner et al. 2018) and 4 endogenously grown tumors were isolated from (GEMM: CKPlox) tumors by studious cutout of the tumor tissue and culturing of it under standard conditions. The established mPDAC cells were cultured in high glucose Dulbecco's Modified Eagle Medium (DMEM, Thermo Fisher Scientific, Waltham, USA) supplemented with 10% fetal bovine serum (FBS, Thermo Fisher Scientific, Waltham, USA) and 1% Penicillin/Streptomycin

(P/S, Thermo Fisher Scientific, Waltham, USA). For immunofluorescence (IF) staining, cells were cultured in DMEM supplemented with 5mM D-glucose (Thermo Fisher Scientific, Waltham, USA), 2 mM L-glutamine (Sigma-Aldrich, St. Louis, USA) 5% FBS for 48h prior experiments.

For immunofluorescence (IF) staining, cells were washed and fixed for 10 min at RT using 4% PFA, treated with 0.15% glycine for 5 min, permeabilized with 0.2% Triton-X 100 in PBS. After washing, cells were blocked for 1.5 h in 10% donkey serum and 0.1% BSA diluted in PBS. The primary antibodies were incubated overnight at 4°C in 0.1% BSA diluted in PBS Anti-CDH1 (1:200, AF748, R&D Systems), Anti-Vimentin (1:50, MAB2105, R&D Systems), Anti-MCT4 (1:100, rabbit, sc-50329, Santa Cruz Biotechnology). After washing, the secondary antibodies were incubated for 2.5 h at RT in the dark (donkey anti-goat AF488, donkey anti-rat AF594, donkey anti-rat AF680, 1:250, Invitrogen). Thereafter, cells were treated for 2 min with DAPI, washed and mounted. Slides were kept at 4°C until further analysis using the Leica TCS SP8 Confocal Microscope (Leica). The immunofluorescence staining was performed by K.P.

2.3 NUCLEAR SEGMENTATION AND ANALYSIS IN MURINE CYTOLOGY

The entire image processing and analysis algorithms were used to analyze 5-9 representative images of each cell line using MATLAB (R2018b) by Mathworks, Inc. (Natick, MA). The images were acquired at a resolution of 1024x1024 pixels and stored in TIF (tagged image file) format. No shade or other correction was performed on the images prior to processing.

Segmentation for cell counting was implemented using a novel second order thresholding method (LPA, see VII.4.6.1, Fig.VII-7) as standard thresholding techniques such as Otsu's method delivered unreliable results concerning nuclear counting. After reading the image the 2-dimensional image matrix of the blue channel is chosen (DAPI3) for the DAPI fluorescence molecule emits wavelengths in the blue spectrum. After that the LPA is implemented creating a loop segmenting the image with a preset number of thresholds (x) specified by an x-dimensional vector (ThresholdVector).

```
[x y] = size(DAPI3);
Start = 5;
TresholdVector = [Start:1:50];
[b sizeThresholdVector] = size(TresholdVector);
Resultsvektor = 0;

for k = 1:sizeThresholdVector
Threshold = TresholdVector(b,k);
DAPIT = DAPI3;

for i = 1:x
```

```
for j = 1:y

if DAPIT(i,j) > Threshold
DAPIT(i,j) = 255;
else DAPIT(i,j) = 0;
end

end

end

[LABELEDDAPI, numNuclei] = bwlabel(DAPIT);
Resultsvektor(1,k) = numNuclei;

end
```

Code IV-1: Implementation of LPA (1)

The nuclear counts at x thresholds are plotted and smoothed. Then the first low-point of the graph is selected using the function *islocalmin()*. Finally, the image is binarized using that threshold.

```
MIN = min(Resultsvektor);
ResultsvektorSmooth = smooth(Resultsvektor);
TF = islocalmin(ResultsvektorSmooth);
[row,col] = find(TF==1);
LowestCount = Resultsvektor(1, row(1,1));
[row1,col1] = find(LowestCount == Resultsvektor);
TT = 5+col1;
DAPITT = DAPI;
[x y] = size(DAPITT);


for i = 1:x

for j = 1:y

if DAPITT(i,j) > T;
DAPITT(i,j) = 1;
else
DAPITT(i,j) = 0;
end

end

end
```

Code IV-2: Implementation of LPA (2)

Through a subtraction of y pixels at the borders of nuclei (equals the mathematical operation of erosion using a square the size of y) a successful separation of overlying cells could be reached. This approach was even improved when successively increasing the threshold on a distance transform matrix of the segmented nuclei and simultaneous counting of the regions. As the threshold on the

distance transform map increases, more and more overlapping nuclei are separated. When the threshold further increases some nuclei are lost to under-segmentation. That is why the region counts with increasing thresholds were plotted. The local maximum was chosen and considered the final automated count (see Fig.IV-2).

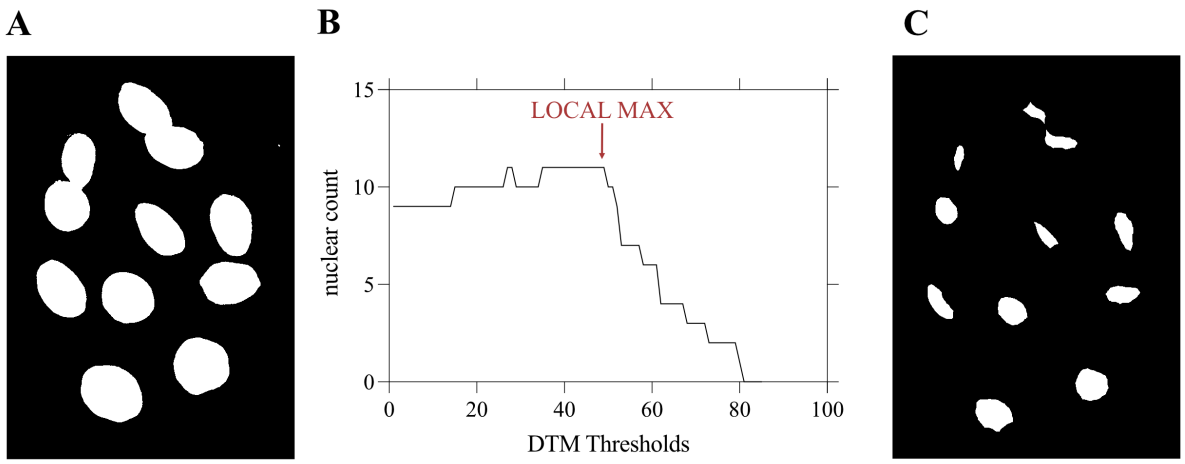

Fig.IV-2: Separating overlapping nuclei by distance transform matrix thresholding (A) Segmented nuclei by LPA (B) nuclear counts at increasing thresholds on distance transform matrix (DTM) (C) Segmentation used for nuclear count after segmenting at local maximum

Furthermore, a comprehensive analysis of nuclear morphological descriptors as well as the selective extraction of nuclear textural features was sought after.

Morphological descriptors of the segmented nuclei were extracted using the function *regionprops()*, especially including nuclear *Area*, *Eccentricity* (ratio of the distance between the foci of an ellipse and its major axis length). A value of 0 indicates a circular ellipse, while an *Eccentricity* of 1 indicates a line) and *Solidity* (part of the shape that is convex to the modeled elliptic center – Area of the region/Convex area; therefore, unrounded potentially dysmorphic nuclei are expected to have a higher *Eccentricity* than round nuclei).

The extraction of textural features was performed creating a synthetic image (DAPITexture) only consisting of the image information contained within nuclei.

```
for i = 1:x

for j = 1:y

if DAPITT(i,j) > 0
DAPITexture(i,j) = DAPI(i,j);
else
```

```
DAPITexture(i,j) = 0;
end

end

end



DAPITexture01 = DAPITexture(DAPITexture > 0);
[x1 y1] = size(DAPITexture01);
XX = sqrt(x1);
XX = floor(XX);
Xsquare = XX*XX;
DAPITexture01 = DAPITexture01(1:Xsquare,1);
TextureNuclearImage = reshape(DAPITexture01,[XX,XX]);
```

Code IV-3: Creating a synthetic image only containing nuclear area

From this synthetic image a grey-level co-occurrence matrix was created using the function *graycomatrix()* and the textural parameters *Contrast*, *Correlation*, *Energy* and *Homogeneity* were taken using the function *graycoprops()*.

Furthermore, histogram derived descriptors (*mean*, *SD*, *kurtosis* and *skew*) were derived from the synthetic nuclear image.

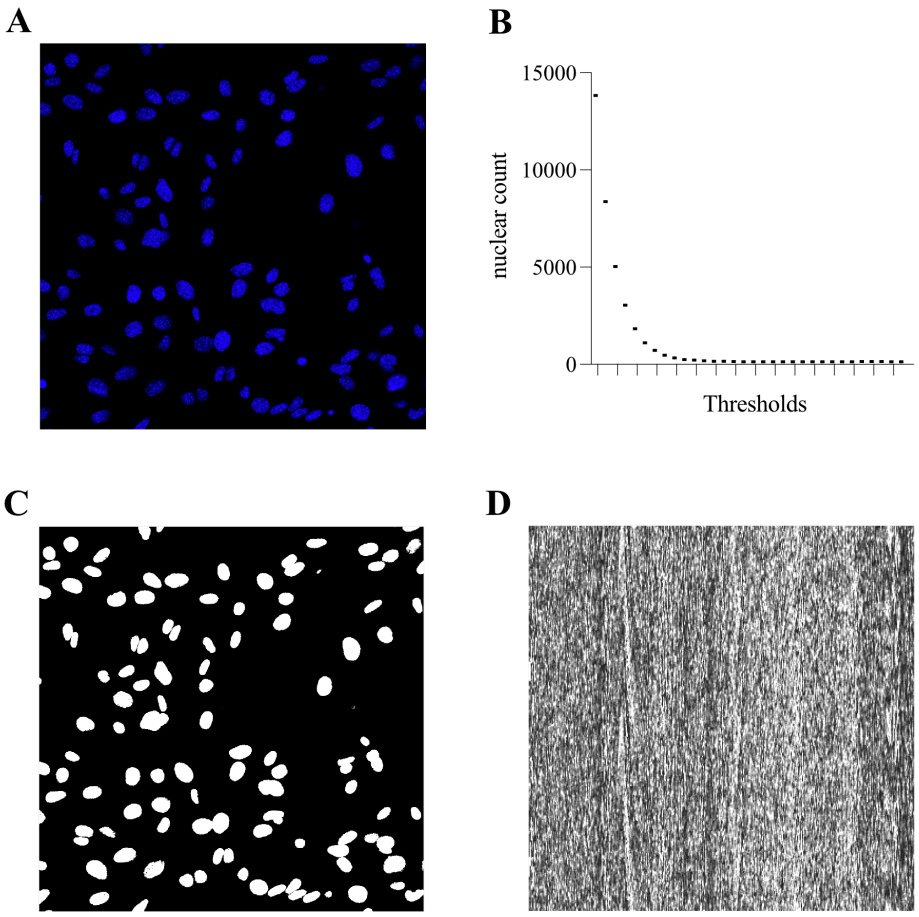

Fig.IV-3: Segmentation and virtual nuclear image ***(A)*** *DAPI-Image of nuclei* ***(B)*** *LPA-Graph* ***(C)*** *segmented image* ***(D)*** *virtual nuclear image (augmented)*

2.4 STAINING OF MURINE HISTOLOGY

Murine PDAC tissue samples were fixed in 4% PFA/PBS solution, dehydrated and paraffin-embedded (FFPE) according to the standard pathology core conditions of Technical University of Munich. FFPE slices of 2-4 µm were stained with (Mayer's hematoxylin and eosin (H&E), according to a standard protocol) for tissue visualization (1. Xylol 2x 2min; 2. 100% Ethanol 1 min; 3. 96% Ethanol 1 min; 4. 70% Ethanol 1 min; 5. Desalinated water 30 s; 6.Mayer's hematoxylin 8 min; 7. Rinse with water 10 min; 8. Eosin solution 5 min; 9. 96% Ethanol 25s; 10. Isopropanol 25 s; 11. Xylol 1,5 min).

For immunohistochemical (IHC) stainings slides were send to the Pathology department of the Technical University of Munich and stained in the laboratory of PD Dr. Katja Steiger. FFPE slices were pretreated 30 min with citrate buffer pH=6.0 and stained with antibodies against CD31. Antibody binding was detected using DAB as chromogen after pre-incubation with respectively Bond Polymer

Refine Detection Kit (Leica). Nuclei were counterstained with hematoxylin. All slides were digitalized using Aperio Scanner (Leica). For analysis representative images of all tumor regions were taken – large vessels were excluded, as nuclear feature extraction was the goal of this study.

2.5 NUCLEAR SEGMENTATION AND ANALYSIS OF MURINE HISTOLOGY

Nuclear segmentation of complex histologic images with compact growth patterns requires more intricate automated segmentation techniques. After reading the image the first channel of the RGB image was selected due to its high nuclear contrast after staining with hematoxylin. Prior to image segmentation, a Gaussian Filter was applied to reduce the influence of noise on the segmentation result. For nuclear segmentation, different approaches were chosen depending on the task. First, the LPA approach was implemented as described above. Here, nuclear segmentation was specific – overlapping nuclei were not separated. That is why the LPA-based segmentation was used to create the virtual texture image to extract texture and histogram-derived parameters.

For the morphological description of cells, a different segmentation technique was used. It is based on the observation that with increasing Gaussian filtering, more separated nuclear regions merge. Creating an additive image of increasing degrees of Gaussian filtering thereby enhances contrast at these merging zones. Then, a differential image of this additive image was created in 4 directions (0°, 90°, 180°, 270°) revealing an image depicting these merging zones and thereby separating conglomerate nuclei while maintaining the overall shape of the nucleus which is relevant for the morphologic description. The separation between nuclei using this technique was superior to the implemented watershed algorithm considering the number of successfully segmented nuclei as well as preserving their shape.

After Gaussian filtering, this image was treated with a Canny edge detection algorithm and then was binarized again. Then only negative areas within the edges of the cells were counted as positive in a binary image. This image represents the inner nuclear shape with incomplete separation of nuclei. Full separation was reached by adding a binarized distance transform an image (PEAKMAP, see Code IV-4). When a threshold was applied to this additive image the nuclei are separated while maintaining the nuclear shape as far as possible (illustrated in Fig.IV-4.).

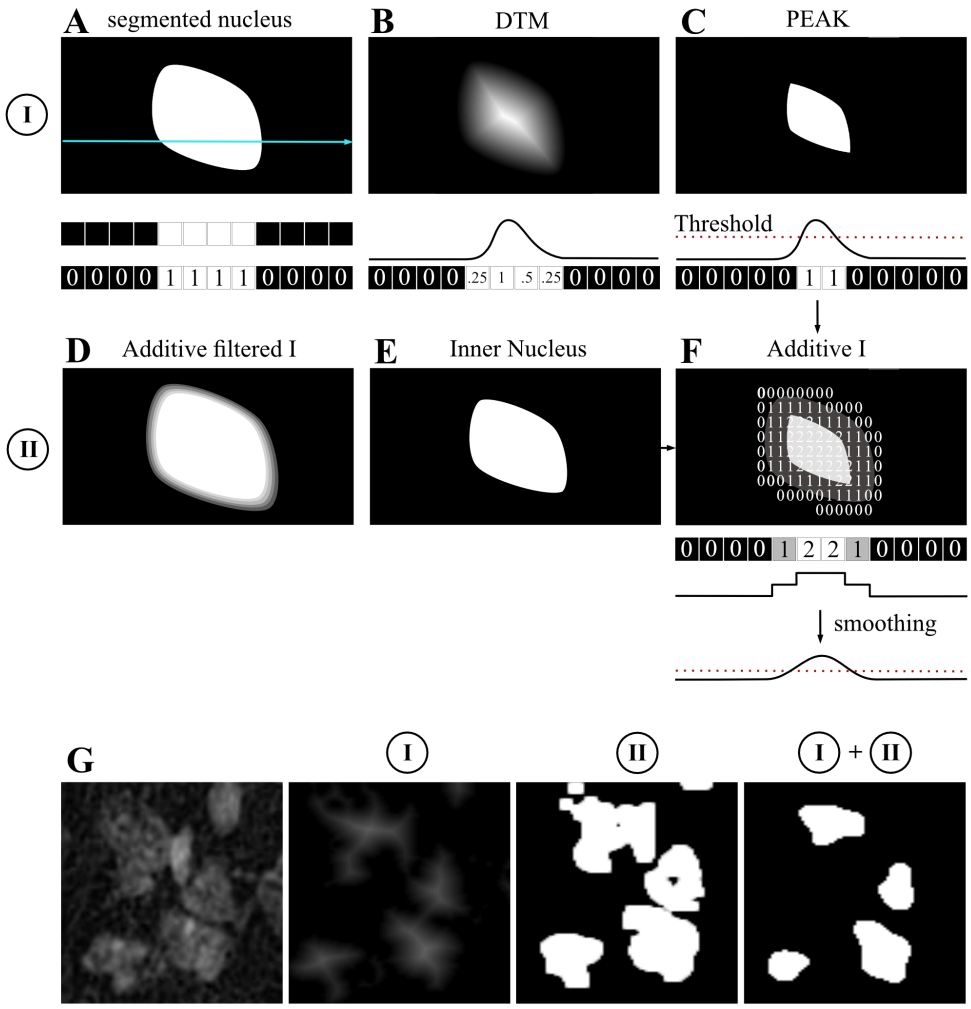

Fig.IV-4: Illustration of nuclear segmentation methodology for morphologic characterization in histology ***(A)*** *Segmented nucleus (using LPA)* ***(B)*** *Distance transform (DTM) image where the intensity values of the pixels are proportional to the distance from a non-positive pixel* ***(C)*** *Thresholded DTM image labeled PEAK with morphologic preservation but areal loss* ***(D)*** *Additive image of differential Gaussian filtering adding contrast to merging zones* ***(E)*** *Inner Area D* ***(F)*** *Additive Image of C and E* ***(G)*** *Summary of procedures I and II and creation of smoothed F (on the left)*

For cell counting, the shape of nuclei is not important, solely their number and therefore their reliable separation in nuclear conglomerates. This is accomplished via a distance transform after LPA segmentation creating an image (DTM) in which the intensity of pixels in a positive region is proportional to its distance form a negative region. Through thresholding a virtual image containing only the peaks of the nuclei is created which is suitable for nuclear counting.

```
DTM = bwdist(~DAPITT);
DTT = 8;
PEAKMAP = DTM;

for i = 1:x

for j = 1:y

if PEAKMAP(i,j) > DTT
PEAKMAP(i,j) = 1;
else
PEAKMAP(i,j) = 0;
end

end

end
```

Code IV-4: Implementation of a distance transform on a LPA segmented image

As strict quantitative description of cell morphology can remain difficult in this model, as the parameters of *Eccentricity* and *Solidity* are prone to errors from inaccurate segmentation, the quantitative assessment is accompanied by a descriptive morphological characterization.

2.6 STATISTICAL ANALYSIS

Statistical analysis was performed in GraphPad Prism (version 7 and 8, GraphPad Software Inc., San Diego, CA). For all statistical tests, a level of significance of 5% was used. A two sided Student's t-tests were performed for group comparisons of normally distributed quantities. The strength of association between quantitative measures was assessed by Pearson's (r, normally distributed data) correlation coefficient. Data presented as mean values including standard deviation or 95% confidence interval (95%-CI).

3. RESULTS

The presentation of results is structured as follows: In 3.1 the expression patterns of epithelial and mesenchymal cell lines are evaluated. 3.2 the quality of the automated nuclear segmentation is shown. 3.3 to 3.5 describe findings of morphologic analysis in different tumor models of PDAC.

3.1 EXPRESSION PATTERNS OF EPITHELIAL AND MESENCHYMAL CELL LINES

The expression patterns of MCT4 in cell lines were coherent with immunohistochemical data of the grown tumors. Staining for E-Cadherin, a marker for epithelial cells underlined their respective subtype (Mean E-Cadherin$_E$ [a.u.] = 4.980 ± 1.243 vs. Mean E-Cadherin$_M$ [a.u.] = 2.272 ± 0.251, see Fig. IV-5 B). A strong correlation between Vimentin – a marker of mesenchymal growth – and MCT4 expression was found in stained cell samples ($r = 0.874$, 95%-CI: 0.704-0.949, $p<0.001$) while cell lines from mesenchymal tumors showed higher Vimentin (Mean Vimentin$_E$ [a.u.] = 1.397 ± 0.280 vs. Mean Vimentin$_m$ [a.u.] = 2.471 ± 0.380, see Fig. IV-5 C) and MCT4 expression (Mean MCT4$_E$ [a.u.] = 2.870 ± 0.587 vs. Mean MCT4$_M$ [a.u.] = 3.923 ± 0.41, see Fig.IV-5 D). Furthermore, strong correlations between the mesenchymal marker Vimentin and MCT4 expression have been found in grown cell lines ($r = 0.874$, 95%-CI = 0.704 to 0.949, $p < 0.001$).

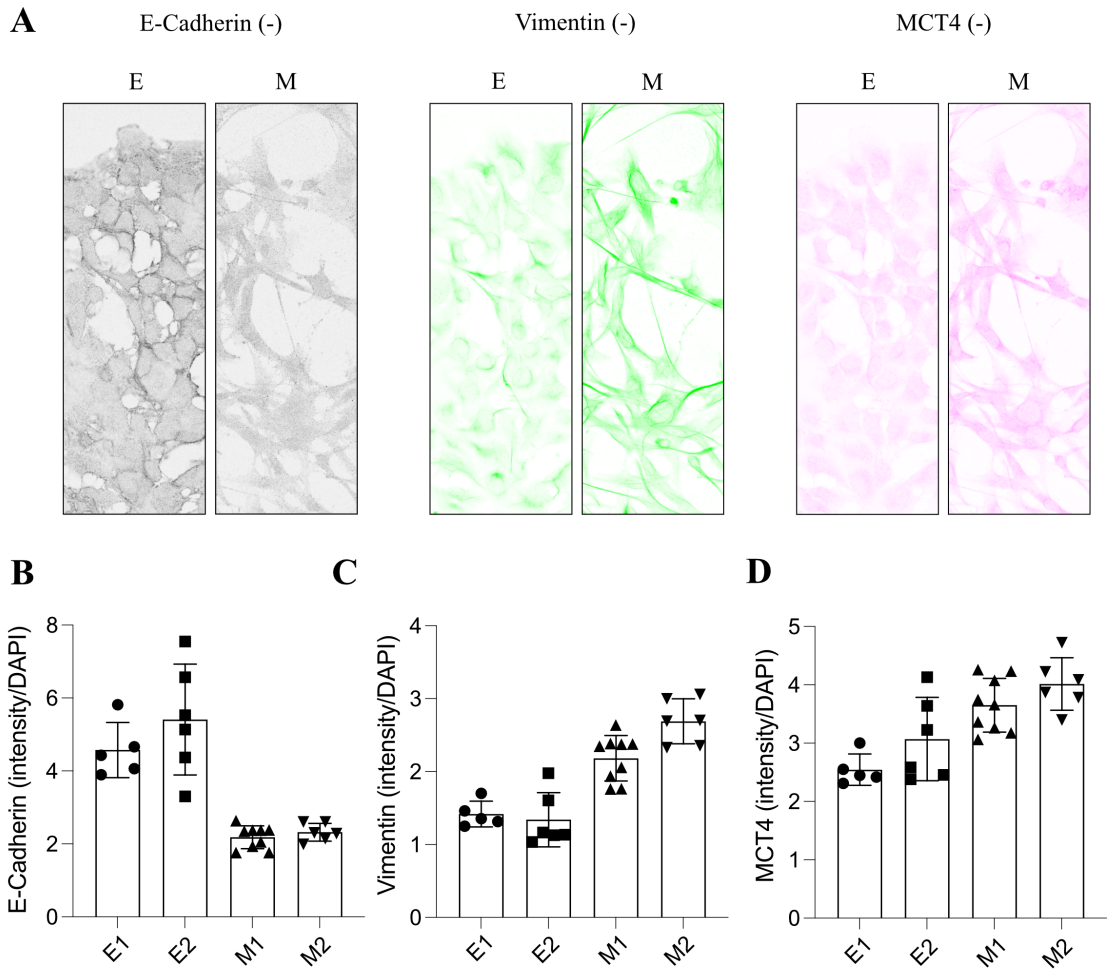

Fig.IV-5: Expression of biomarkers in cultivated cells with clear phenotype of mPDAC ***(A)*** *from left to right: negative image of E-Cadherin immunofluorescence in epithelial (E) and mesenchymal (M) cell lines, negative image of Vimentin immunofluorescence in epithelial (E) and mesenchymal (M) cell lines and negative image of MCT4 immunofluorescence in epithelial (E) and mesenchymal (M) cell lines* ***(B)*** *Expression of E-Cadherin in 4 cell lines (E1+E2 = epithelial cell line; M1+M2 = mesenchymal cell line)* ***(C)*** *Expression of Vimentin in 4 cell lines (E1+E2 = epithelial cell line; M1+M2 = mesenchymal cell line)* ***(D)*** *Expression of MCT4 in 4 cell lines (E1+E2 = epithelial cell line; M1+M2 = mesenchymal cell line)*

3.2 NUCLEAR SEGMENTATION

The nuclear evaluation is based on the need for reliable nuclear segmentation. Using the described image analysis workflow, automated nuclear counts in cytology (correlation with manual count: r = 0.993; 95%-CI: 0.968 to 0.998; p<0.001, see Fig.IV-6 C) and histology (correlation with manual count: r = 0.913; 95%-CI: 0.667 to 0.980; p<0.001, see Fig.IV-6 D) were satisfactory (counts were

compared in a representative subset including 10 images of cytology and 10 images of histology). In cytology as well as histology, the automated cell count of epithelial tumors did in average deviate more from manual cell count than mesenchymal tumors due to cell clustering and incomplete separation during the segmentation process (exemplary for cytology: Mean deviation in epithelial cell lines = 6.48% vs. Mean deviation in mesenchymal cell lines = 3.04%).

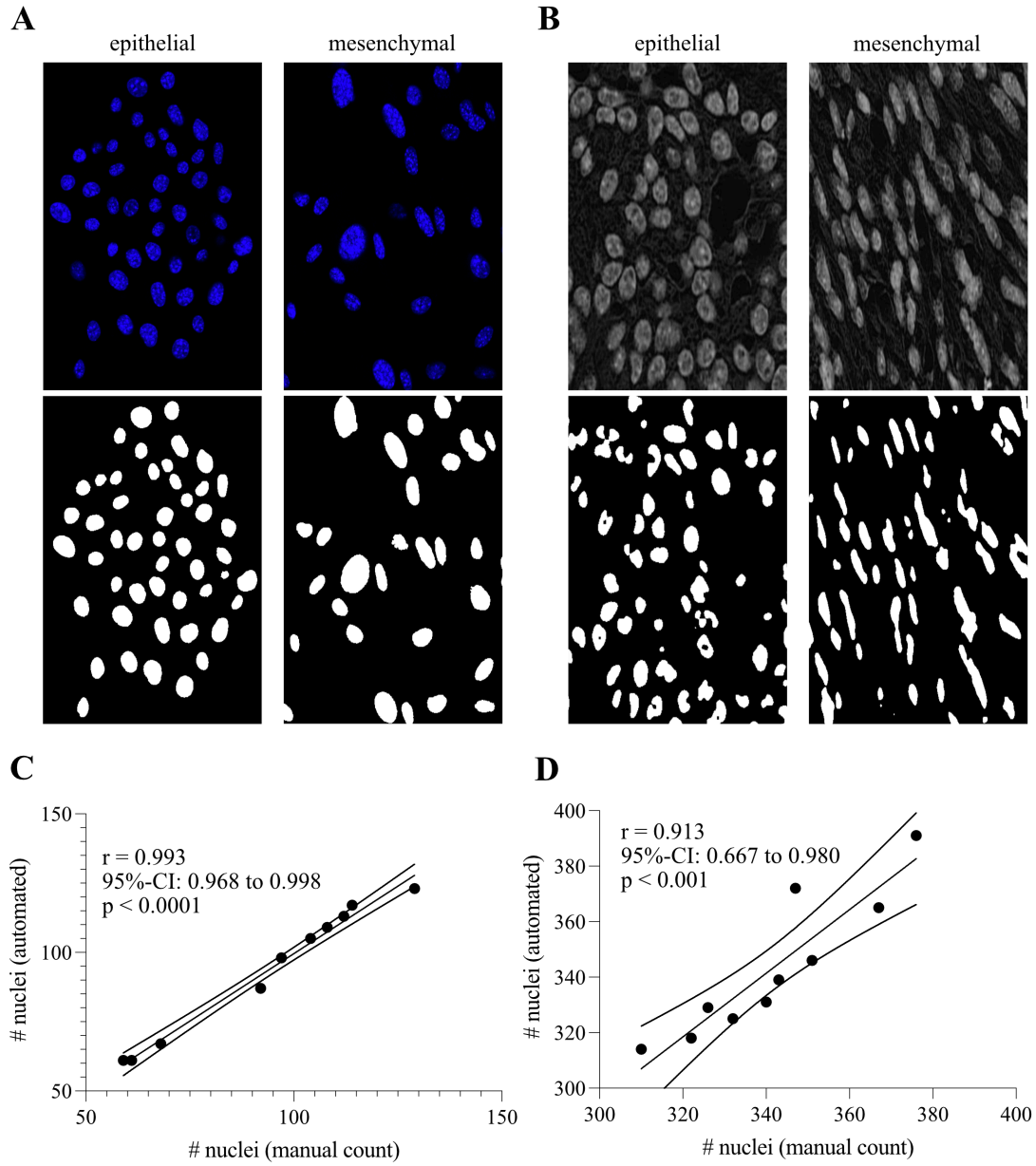

Fig.IV-6: Segmentation results and comparison between manual and automated nuclear count ***(A)*** *Segmentation in cytology of epithelial and mesenchymal cell lines* ***(B)*** *Segmentation in histology of orthotopically implanted PDAC* ***(C)*** *Comparison of nuclear count between manual and fully automated count in cytology* ***(D)*** *and histology of orthotopically implanted tumors*

These results indicate a successful separation of nuclei. As explained above morphological preservation parallel to successful separation of nuclei was aimed for in this image analysis workflow. This was particularly hard to achieve in the histology of orthotopically-implanted tumors as these tumors showed highly cellular growth with only marginal stromal recruiting. This led to many overlapping and distorted nuclei in the resulting histologic slides. However, satisfactory morphologic preservation was achieved as shown in Fig. IV-7. In this figure, it is illustrated which morphologies were counted as depicted correctly and incorrectly respectively. Less than 5% of nuclei examined were counted as incorrectly represented. Limits of the segmentation were observed in dense clusters of tumor cells often including more than 5 cells where epithelial tumors were affected more than mesenchymal tumors by this incomplete separation and therefore incorrect morphologic description of nuclei.

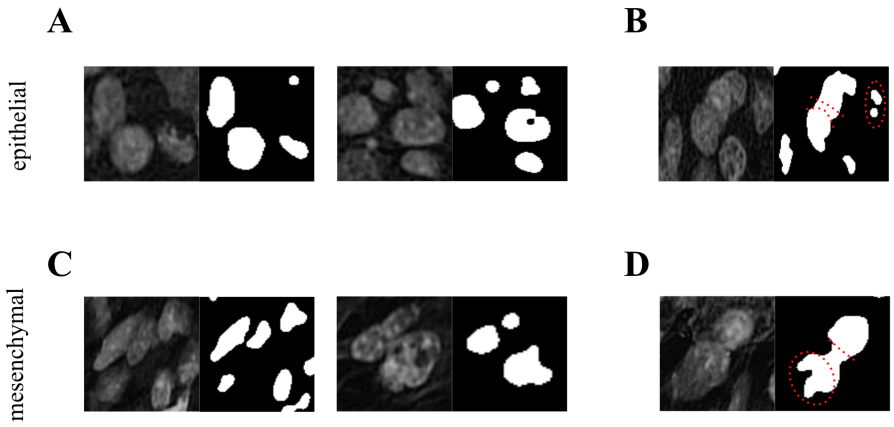

Fig.IV-7: Separation of tumor cell clusters with morphological preservation in histology derived from orthotopically implanted tumors ***(A)*** *Correctly separated and morphologically preserved epithelial tumor cells* ***(B)*** *Incorrectly (under-)segmented epithelial tumor cells (red lines indicate desired separation, red circles indicate erroneous segmentation)* ***(C)*** *Correctly separated and morphologically preserved mesenchymal tumor cells* ***(D)*** *Incorrectly (under-)segmented mesenchymal tumor cells (red lines indicate desired separation, red circles indicate erroneous segmentation)*

3.3 MORPHOLOGIC CHARACTERISTICS OF NUCLEI IN EPITHELIAL AND MESENCHYMAL PDAC

In the well-characterized cytology, relevant morphological nuclear differences between epithelial and mesenchymal cell lines could be mapped out (see Fig.IV-8). Nuclei of epithelial and mesenchymal cell lines differed significantly regarding their mean nuclear intensity ($p = 0.015$, Fig.IV-8 A), standard

deviation of nuclear intensity (p = 0.045, Fig.IV-8 A), nuclear *Eccentricity* (p < 0.0001, Fig.IV-8 B), nuclear *Solidity* (p = 0.002, Fig.IV-8 B), and GLCM derived *Contrast* (p = 0.020, Fig.IV-8 C) – with nuclear *Eccentricity* being the most selective parameter.

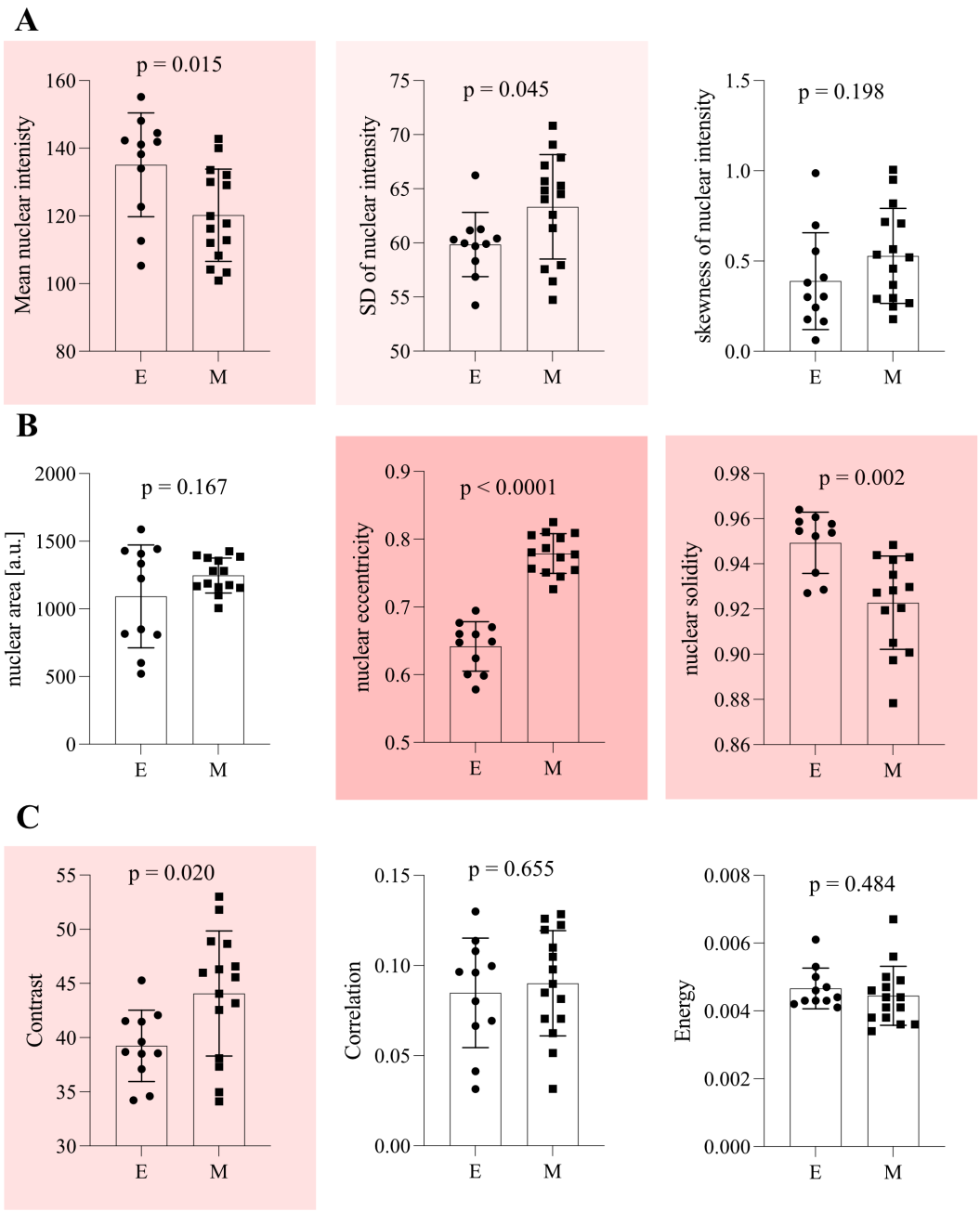

Fig.IV-8: Overview over important nuclear descriptors in epithelial (E) and mesenchymal (M) cell lines ***(A)*** *histogram derived descriptors* ***(B)*** *morphological descriptors* ***(C)*** *GLCM-matrix derived textural features as indicated*

A more heterogeneous morphological pattern could be observed in the histology of orthotopically-implanted tumors derived from the cell lines described. Here, the characteristics blended as cells transformed embedded in their respective microenvironment (see Fig. IV-10). No significant

differences could be seen clustering lesions into epithelial and mesenchymal ones (see Fig.IV-9 A-C). However, tendencies observed in the cell lines remained visible in the growing tumors – regions containing transitioning nuclei influenced the results of morphologic characteristics (in epithelial as well as mesenchymal tumors, see Fig.IV-12 & Fig.IV-13).

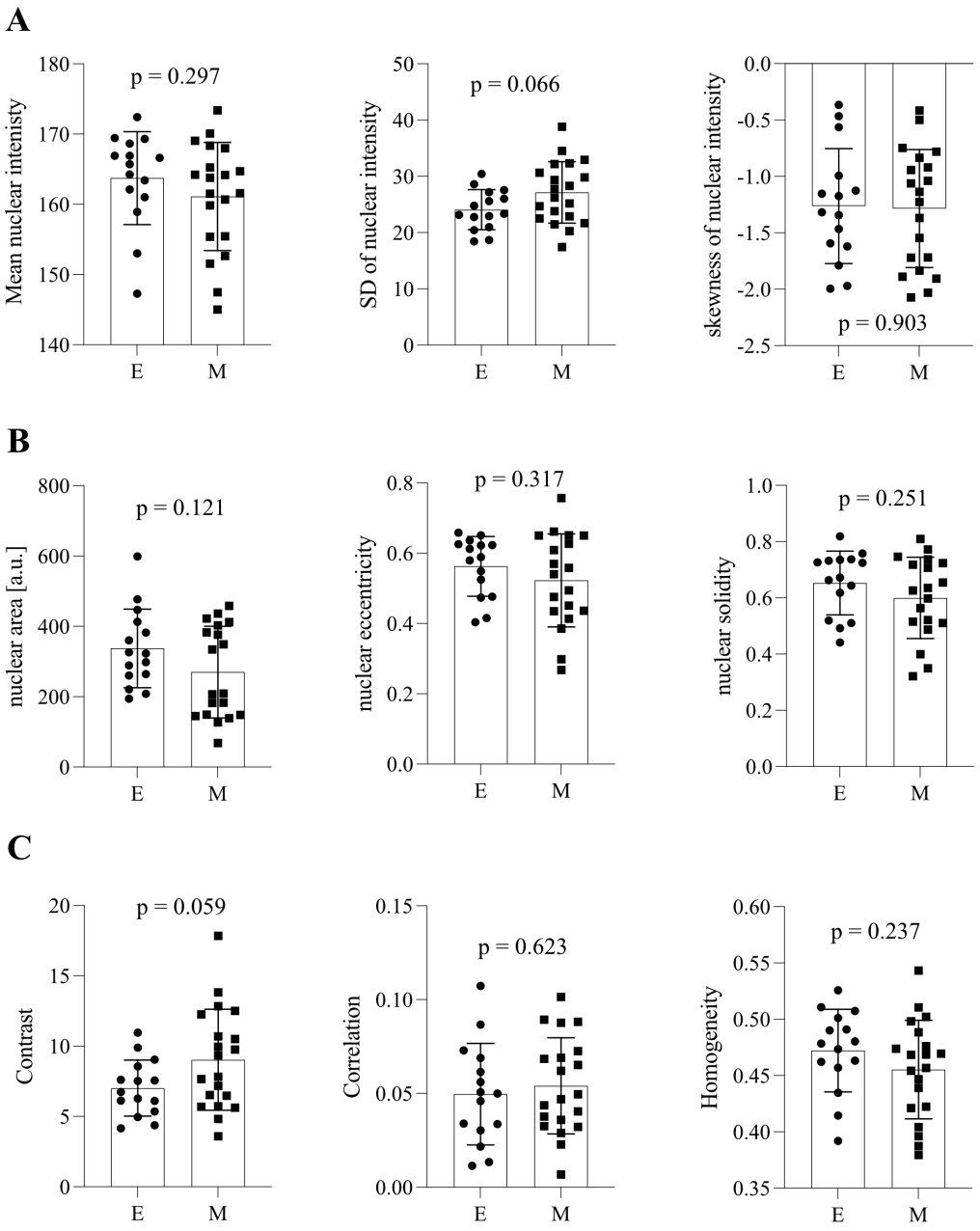

Fig.IV-9: Overview over important nuclear descriptors in epithelial (E) and mesenchymal (M) tumors ***(A)*** *Histogram derived descriptors* ***(B)*** *Morphological descriptors* ***(C)*** *GLCM-matrix derived textural features*

The morphologic transition of nuclei is further illustrated in Fig.IV-9. It can be stated that orthotopically-implanted tumors deriving from epithelial cell lines show locally contained

morphologic transition to elongated, unrounded morphology characteristic for mesenchymal growth. Also, tumors deriving from mesenchymal cell lines have specific regions where the nuclei exhibit round and regular morphology, which is typical for epithelial growth (see Fig.IV-10). These transitory zones are specific to a certain region of the tumor and cannot be attributed to the whole lesion.

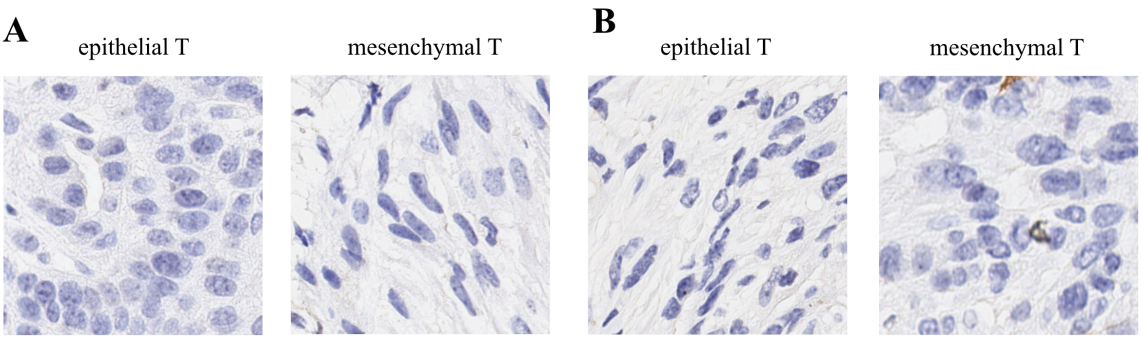

Fig.IV-10: Exemplary images of nuclear morphology in orthotopically-implanted tumors (T) derived from epithelial PDAC cells (epithelial T) and mesenchymal PDAC cells (mesenchymal T) – ***(A)*** *Main nuclear morphology prevalent in respective lesions with epithelial tumors showing round and mesenchymal tumors showing unrounded spindle shaped nuclei* ***(B)*** *Exemplary images of zones with morphologic transition – epithelial tumors containing nuclei with unrounded morphology and mesenchymal tumors showing epithelial nuclear morphology*

3.4 Association of nuclear morphology to biomarker expression in MPDAC cytology

As depicted in III, different relevant metabolic (including MCT4, GLUT1) and subtype-specific (E-Cadherin, Vimentin) biomarkers have been identified for murine PDAC. Mesenchymal cell lines revealed higher expression levels of Vimentin and MCT4 in-vitro whilst having lower and less membranous staining for E-Cadherin. In this study the ties between morphologic characteristics and biomarker expression have been explored – in the description below a focus is put on subtype specific morphologic descriptors such as Mean nuclear intensity, standard deviation of nuclear intensity, nuclear *Eccentricity*, nuclear *Solidity* and GLCM derived *Contrast*.

In the well characterized epithelial and mesenchymal cell lines a reciprocal relation between Vimentin/MCT4 expression and Mean nuclear intensity has been found (see Fig.IV-11 A). This did span epithelial as well as mesenchymal cell lines. Concerning E-Cadherin expression there was a linear reciprocal correlation with standard deviation of nuclear intensity observed. However, this was not true for mesenchymal cell lines with their constant low baseline expression of E-Cadherin (see Fig.IV-11 A). The morphologic descriptor of *Eccentricity* did show highly relevant subgroup

differentiation (see Fig.IV-11 B). However, no stringent association with biomarker expression was found (see Fig.IV-11 B). Nevertheless, it can be summarized that *Eccentricity* is positively correlated to Vimentin and MCT4 and reciprocally correlated to E-Cadherin expression (see Fig.IV-11 B). Although the texture derived parameter *Contrast* showed good differentiation between epithelial and mesenchymal tumors, it was not correlated to biomarker expression (see Fig.IV-11 C). A negative correlation between *Contrast* and E-Cadherin expression in epithelial cell lines was noted (see Fig.IV-11 C).

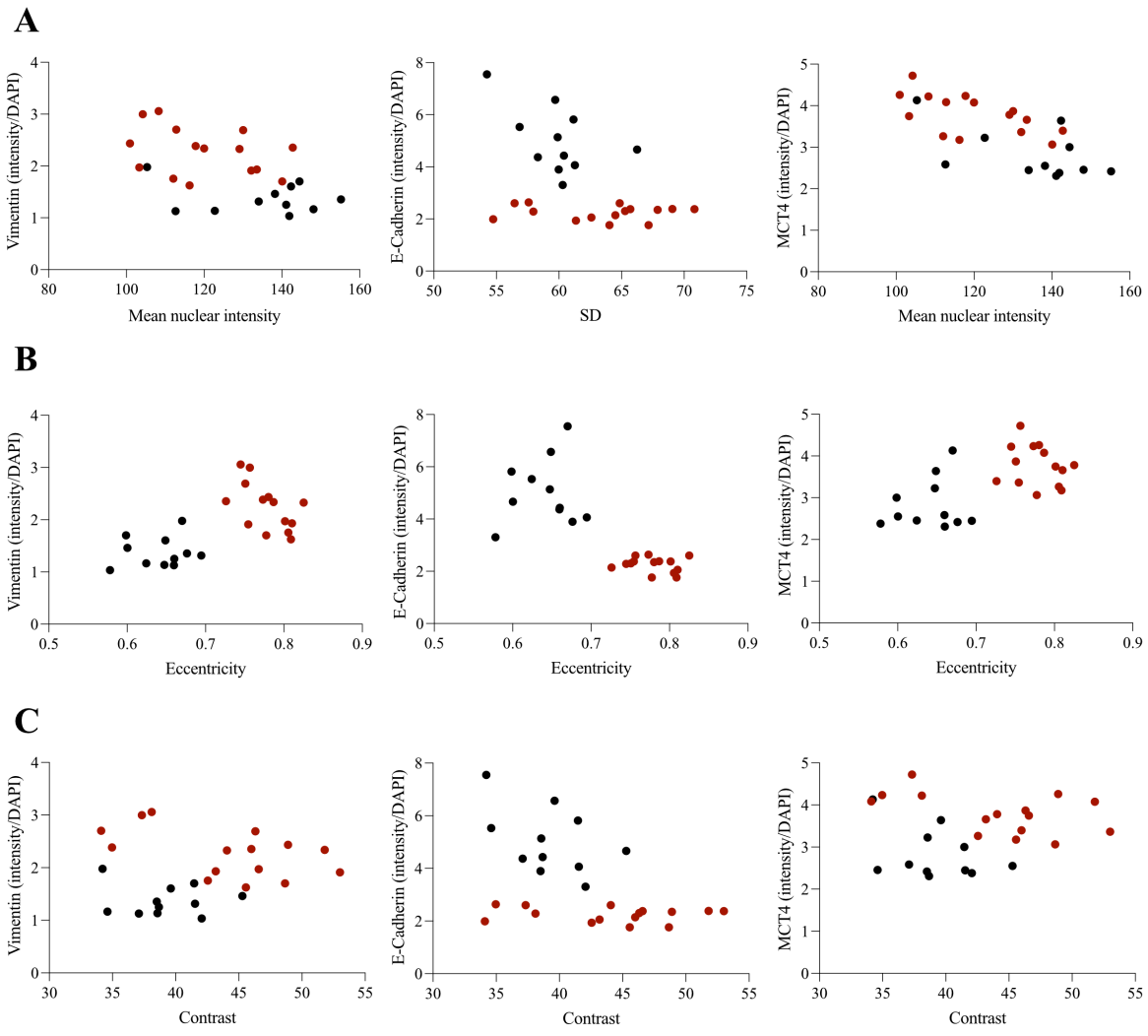

Fig.IV-11: Association of morphologic descriptors and biomarker expression in epithelial (black) and mesenchymal (red) cell lines ***(A)*** *association between the histogram derived Mean nuclear intensity and standard deviation of nuclear intensity (SD) with biomarker expression* ***(B)*** *association between the morphologic descriptor Eccentricity and biomarker expression* ***(C)*** *association between GLCM matrix derived textural descriptor Contrast and biomarker expression*

As explained these investigated cell lines are of dichotomous nature and therefore are of high power in illustrating feasibility and relevance of the implemented study protocol. However, they lack impactful

biological meaning for the morphologic description of nuclei of other tumor models such as human PDAC. That is why the investigation of morphological descriptors in cytology was extended to cell lines that were extracted from endogenous murine PDAC, which mimics the genesis of human PDAC more closely. These cell lines can be perceived not as dichotomous but can be characterized on a spectrum between epithelial and mesenchymal growth. Interestingly in the cell lines of this tumor model a direct correlation between E-Cadherin and MCT4/Vimentin expression was observed as explained above.

Histogram derived descriptors

	E-Cadherin			Vimentin			MCT4		
	r	95%-CI	p	r	95%-CI	p	r	95%-CI	p
Mean nuclear intensity	-0.08010	-0.5047 to 0.3757	0.7371	-0.3143	-0.6644 to 0.1490	0.1772	-0.2215	-0.6047 to 0.2451	0.3481
SD	-0.4955	-0.7693 to -0.06785	0.0263	-0.4863	-0.7643 to -0.05575	0.0297	-0.4805	-0.7612 to -0.04828	0.0320
Kurtosis	0.3242	-0.1382 to 0.6705	0.1632	0.4701	0.03483 to 0.7555	0.0365	0.4002	-0.05149 to 0.7159	0.0804
Skewness	0.02893	-0.4190 to 0.4655	0.9036	0.1814	-0.2839 to 0.5776	0.4440	0.09702	-0.3610 to 0.5173	0.6841

Table IV-1: Histogram derived descriptors and their correlation to biomarker expression in cytology of endogenously grown PDAC

Morphologic descriptors

	E-Cadherin			Vimentin			MCT4		
	r	95%-CI	p	r	95%-CI	p	r	95%-CI	p
Area	-0.8002	-0.9178 to -0.5538	<0.0001	-0.6469	-0.8470 to -0.2863	0.0021	-0.6895	-0.8673 to -0.3554	0.0008
Eccentricity	-0.7404	-0.8940 to -0.4311	0.0003	-0.5718	-0.8145 to -0.1588	0.0105	-0.5871	-0.8221 to -0.1812	0.0082
Solidity	-0.7244	-0.8868 to -0.4027	0.0005	-0.5802	-0.8187 to -0.1710	0.0092	-0.5803	-0.8187 to -0.1712	0.0092

Table IV-2: Morphologic descriptors and their correlation to biomarker expression in cytology of endogenously grown PDAC

GLCM derived texture descriptors (0°)

	E-Cadherin			Vimentin			MCT4		
	r	95%-CI	p	r	95%-CI	p	r	95%-CI	p
Contrast	-0.5354	-0.7906 to -0.1217	0.0150	-0.5386	-0.7923 to -0.1262	0.0143	-0.5331	-0.7894 to -0.1186	0.0155
Correlation	0.3371	-0.1240 to 0.6784	0.1462	0.3958	-0.05665 to 0.7134	0.0841	0.3815	-0.07339 to 0.7050	0.0969
Energy	0.3669	-0.09026 to 0.6964	0.1115	0.3273	-0.1348 to 0.6724	0.1590	0.3333	-0.1282 to 0.6761	0.1510
Homogeneity	0.5246	0.1068 to 0.7849	0.0176	0.5789	0.1833 to 0.8131	0.0075	0,5423	0.1312 to 0.7942	0.0135

Table IV-3: Texture descriptors and their correlation to biomarker expression in cytology of endogenously grown PDAC

As shown by Table IV-1 to Table IV-3, morphologic descriptors such as *Area*, *Eccentricity*, *Solidity* and nuclear texture parameters such as *Contrast* and *Homogeneity* are correlated significantly with biomarker expression. Cells with smaller nuclei showed a higher E-Cadherin, Vimentin and MCT4 expression (see Table IV-2). Interestingly, in this tumor model Vimentin and MCT4 expression of the cell line is reciprocally correlated to *Eccentricity* and *Solidity* (see Table IV-2). This is a highly significant finding, which is contrary to the findings in the well-characterized cytology as explained above. Furthermore, also the GLCM derived texture descriptor *Contrast* is negatively correlated on a significant level to MCT4 and Vimentin expression (see Table IV-3).

It is important to note that nuclear morphology in these cell lines is more heterogeneous than in the cell lines above as depicted in Fig.IV-12. Describing nuclear morphology, it seems the contribution to MCT4 and Vimentin signal strength is proportionally higher for unrounded nuclei, however the data on hand spares quantitative evidence for that observation.

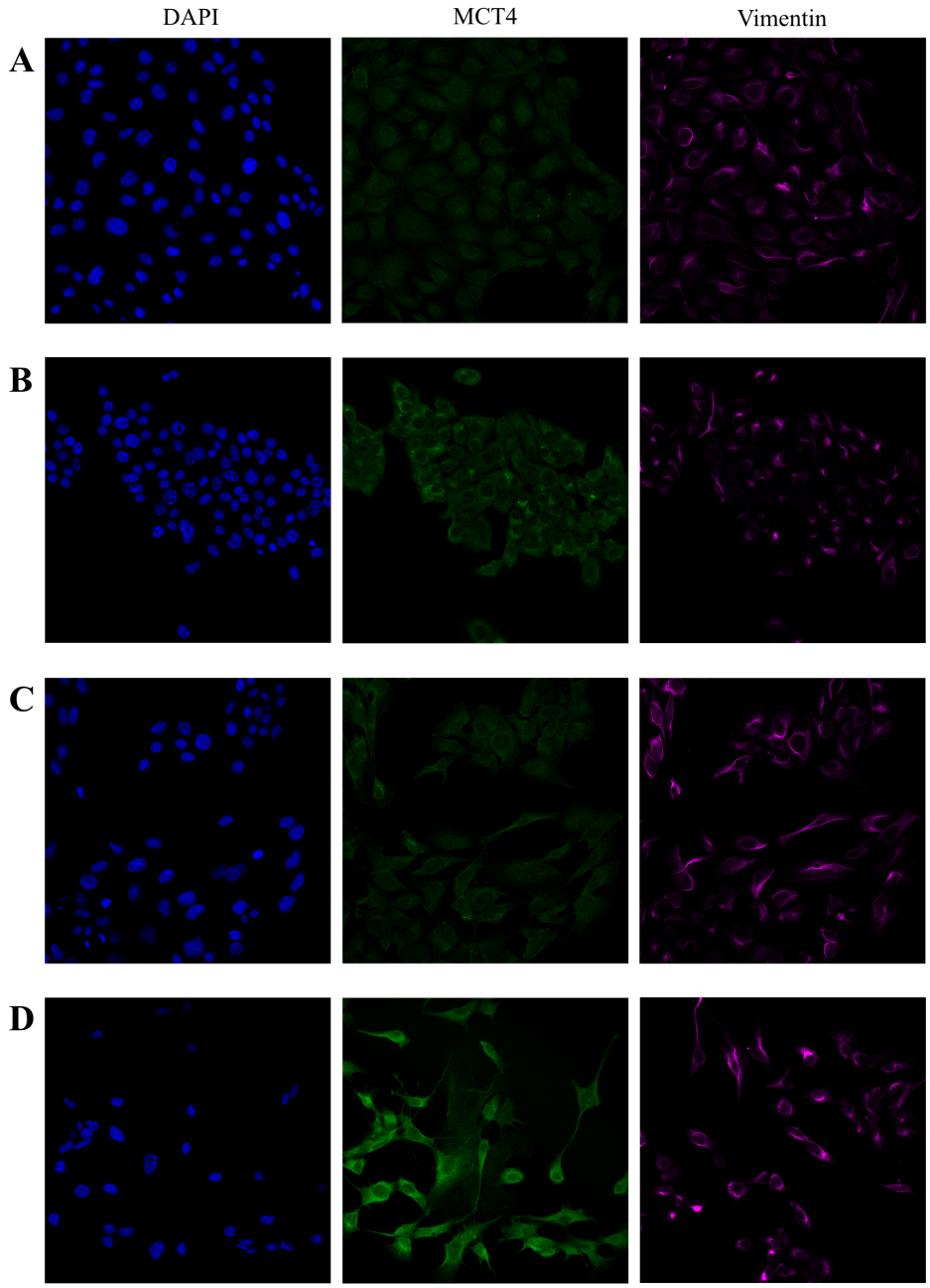

Fig.IV-12: Examples of biomarker expression independent of heterogeneous nuclear morphology ***(A)*** *round nuclei with respective low MCT4/Vimentin expression* ***(B)*** *round nuclei with high MCT4/Vimentin expression* ***(C)*** *unrounded nuclei with low MCT4/Vimentin expression* ***(D)*** *unrounded nuclei with high MCT4/Vimentin*

3.5 Association of nuclear morphology to biomarker expression in histology of murine PDAC

The biomarker expression of epithelial and mesenchymal tumors differed significantly regarding MCT4 (Mean $MCT4_E$ = 51 ± 8.06; Mean $MCT4_M$ = 74 ± 2.59; p = 0.006) as described in III. More precise, epithelial tumors did have a lower baseline expression of MCT4, while singular hotspots of high MCT4 expression (comparable to mesenchymal expression levels) were present. On the other hand mesenchymal tumors had higher baseline expression of MCT4 with contained areas of less MCT4 expression.

Values for nuclear morphology e.g. *Eccentricity* averaged over the entire tumor region are distorted as tumors present high internuclear heterogeneity. That is why correlations of *Eccentricity* and MCT4 expression (r = -0.249; 95%-CI = -0.844 to 0.620; p = 0,590) and *Eccentricity* and GLUT1 (r = -0.374; 95%-CI = -0.879 to 0.528; p = 0.408) expression have limited meaning.

However, when taking a differentiated look at the biomarker expression and nuclear morphology ties between morphologic transition and biomarker expression (MCT4 and GLUT1) can be found. As illustrated in Fig.IV-12 and Fig.IV-13 in 5 from 7 tumors the location of maximal nuclear *Eccentricity* (measured with automated image analysis) was congruent with the location of the highest levels of MCT4 expression (see tumors I, III, IV, V, VII in Fig.IV-12 and Fig.IV-13).

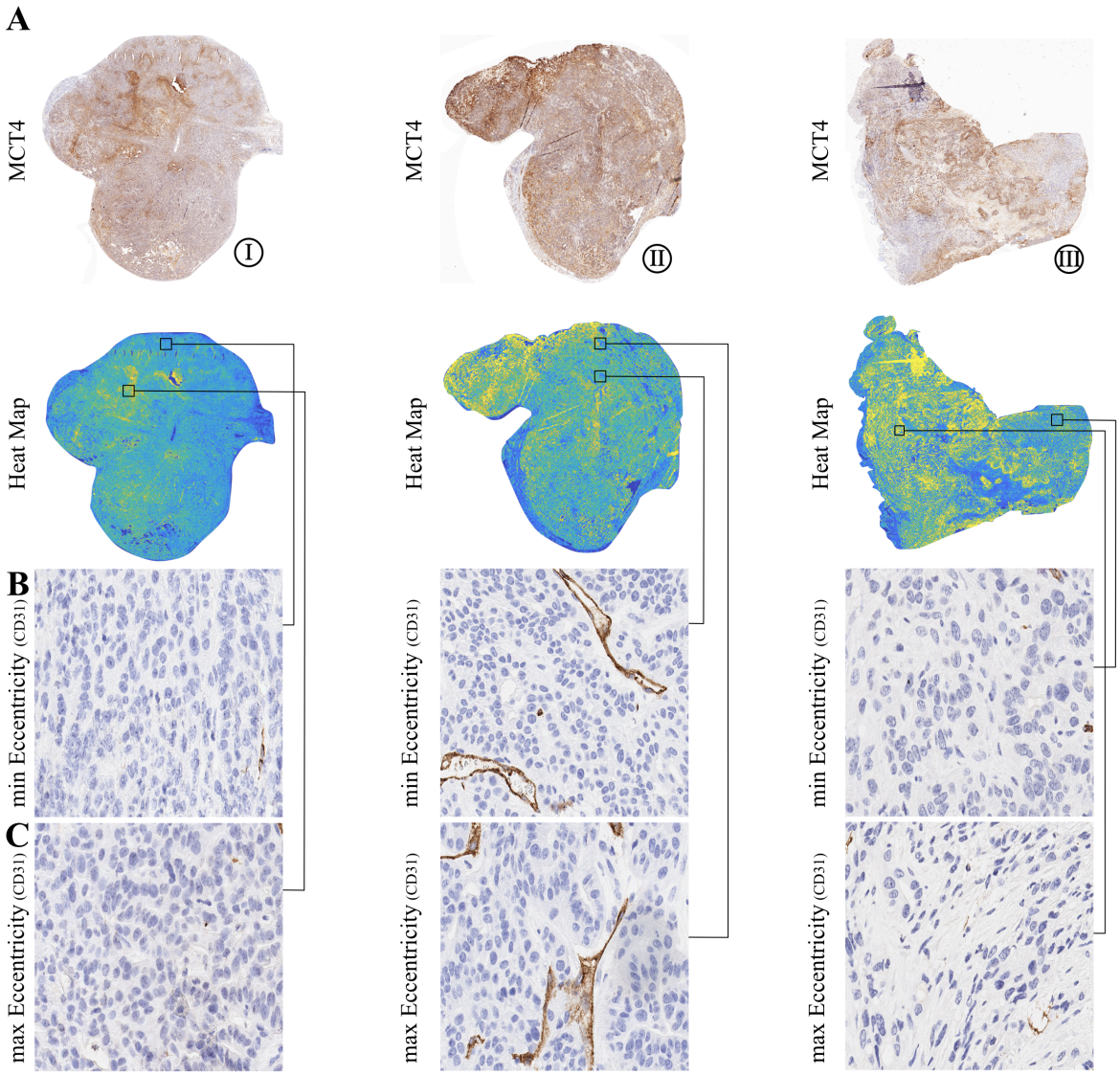

Fig.IV-12: Association between MCT4 expression and nuclear eccentricity in orthotopically implanted tumors derived from epithelial cell lines ***(A)*** *MCT4 staining – tumor region and corresponding heat maps (yellow = higher MCT4 staining, blue = lower MCT4 staining)* ***(B)*** *Location of minimal intratumoral nuclear Eccentricity (location in tumor region indicated by black indicators, image is taken from a respective slide stained for CD31)* ***(C)*** *Location of maximal intratumoral nuclear Eccentricity (location in tumor region indicated by black indicators, image is taken from a respective slide stained for CD31)*

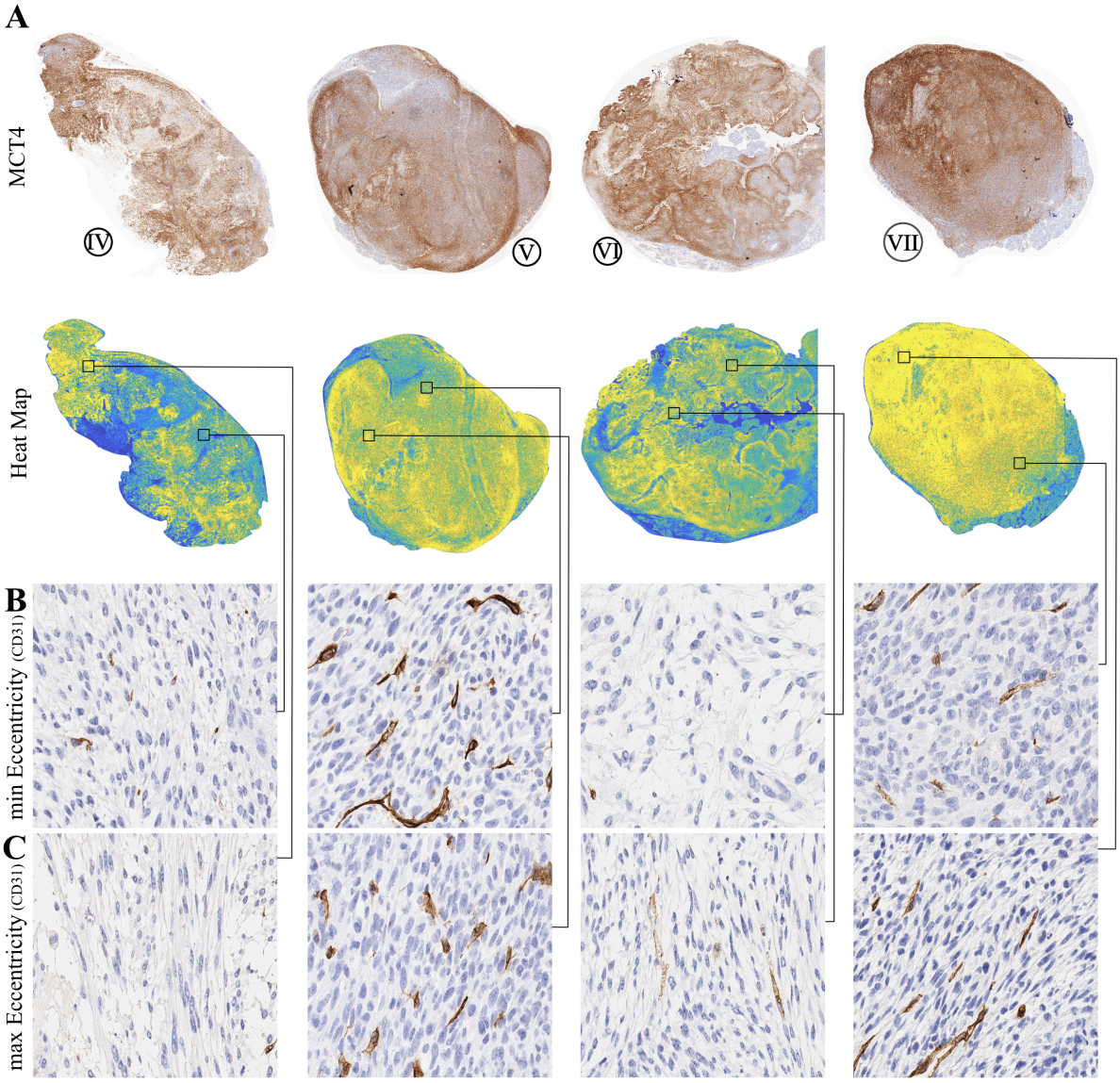

Fig.IV-13: Association between MCT4 expression and nuclear eccentricity in orthotopically implanted tumors derived from mesenchymal cell lines ***(A)*** *MCT4 staining – tumor region and corresponding heat maps (yellow = higher MCT4 staining, blue = lower MCT4 staining)* ***(B)*** *Location of minimal intratumoral nuclear Eccentricity (location in tumor region indicated by black indicators, image is taken from a respective slide stained for CD31)* ***(C)*** *Location of maximal intratumoral nuclear Eccentricity (location in tumor region indicated by black indicators, image is taken from a respective slide stained for CD31)*

This cannot be shown directly for tumors II and VI as these exhibit high diffuse baseline expression of MCT4. Areas of maximal nuclear *Eccentricity* in these tumors did not coincide with areas of maximal MCT4 expression – nevertheless a trend towards morphological transition and MCT4 expression has also been observed in these tumors.

4. DISCUSSION

Quantitative nuclear morphometrics play only a marginal role in PDAC for now. To my knowledge, this is the first study to comprehensively assess parameters of nuclear morphology spanning multiple disease models of PDAC. Although the relevance of nuclear morphology in the assessment of biomarker expression in pancreatic cancer has been acknowledged, it is mainly performed semi-quantitatively (Handra-Luca, Hammel et al. 2014). Furthermore, the success of for adequate patient stratification of automated nuclear analysis in other tumor entities such as cervical cancer (Cheng, Hsieh et al. 2013) emphasizes the need for a more comprehensive morphometric description of this disease.

In this study it has been shown that with the proposed algorithm a nuclear segmentation with a similar precision than previously described algorithms can be reached (Xu, Lu et al. 2017). Additionally, this algorithm potentially allows for more exact morphologic characterization due to improved morphologic preservation. Nevertheless, under-segmentation remains a problem, which led to a more precise morphologic characterization of nuclei in mesenchymal tumors than in epithelial tumors. This small but measurable incline makes the morphologic results in this work biased towards overestimating the complexity of epithelial nuclei. Therefore, subgroup differentiation by nuclear morphometry is expected to improve with more reliable nuclear segmentation.

It has been shown in this study that nuclei of the epithelial and mesenchymal subtype of PDAC exhibit differing morphology. This is coherent with data on the different subtypes and among others their transcriptional patterns for cell adhesion proteins (Collisson, Bailey et al. 2019). It was interesting to describe the morphological changes of nuclei of well-characterized cell lines after orthotopic transplantation as they underwent a transition in vivo. This can be seen as support of the vast heterogeneity of PDAC even in this very controlled model. Nuclei of both morphologies existed side-by-side – partially separated locally – in this tumor model. As the orthotopic tumors did only marginally recruit desmoplastic stroma, erroneous inclusion of stromal morphology did not influence the results in this study.

Furthermore, in cytology of mPDAC the ties of nuclear morphology to MCT4, Vimentin and E-Cadherin expression have been described. This is sensible regarding the biology associated with these markers for also MCT4 plays an important role in cellular transformation (Kong, Nøhr-Nielsen et al. 2016). Here, a complex pattern of morphology derived descriptors and biomarker expression have been found depending on the origins of the cell lines. The endogenously derived cell lines expressing high levels of E-Cadherin and Vimentin are very interesting as they contradict the dichotomous thought of PDAC subtypes. It is possible that these cells were in the process of transition and therefore *"still"* expressing high levels of E-Cadherin and *"already"* expressing high levels of Vimentin and E-

Cadherin. This would also be plausibly supported by the high nuclear heterogeneity within these endogenous cell lines and the high differences in metabolic behavior between these cell lines that was measured in Part One (III.). It is to note that further studies including a higher number of cell lines would be required to approach this observation. However, considering the inherent ties of nuclear morphology and cellular biology, further insights into this topic will prove valuable.

In murine histology, biomarker expression was also linked to nuclear morphology. It has been shown that MCT4 expression was mainly observed in regions containing unrounded and eccentric nuclei. This justifies stating a certain tie between MCT4 and mesenchymal growth in this model, which is consistent with results obtained from human PDAC cell lines (Baek, Tse et al. 2014).

5. CONCLUSION

This study comprises comprehensive selective and automated nuclear characterization in different disease models of PDAC. It is descriptive, illustrating a connection between nuclear morphology and cellular biology that may be exploited diagnostically as the molecular subtypes of PDAC gain more influence into therapeutic decision making in the wake of individualized medicine. Additionally, it positions MCT4 as a biomarker associated with mesenchymal growth. Furthermore, the proposed nuclear segmentation method works reliably and may contribute to advances in this topic but will profit from improved nuclear segmentation.

V. PART THREE: MCT4 IN HUMAN PDAC AND ITS ASSOCIATION TO IMMUNOHISTOCHEMICALLY DETERMINED SUBTYPES

1. INTRODUCTION

In Part One (III.) it has been shown that metabolic imaging signals are correlated to areal MCT4 expression measured in IHC. Regarding 1-^{13}C-pyruvate MRSI, MCT4 is a relevant substrate transporter for lactate in- and efflux and potentially limiting for the pyruvate to lactate conversion rate – similar to what has been observed in cervical cancer (Rao, Gammon et al. 2020). The role of MCT4 in PDAC exceeds other transporters of the MCT family (Kong, Nøhr-Nielsen et al. 2016). Furthermore, expression of MCT4 itself has been attributed to the mesenchymal subtype of PDAC and associated with worse survival in different models (Baek, Tse et al. 2014) and as shown in Part Two (IV.) it is tied to morphologic characteristics of the tumor cells. That is why, a closer look into the role of MCT4 in human PDAC and its association with tumor subtypes is pressing, if 1-^{13}C-pyruvate MRSI is to be translated into the clinic.

In 2016 Noll et al. introduced IHC of HFN1A (hepatocyte nuclear factor 1 homebox A) and KRT81 (Keratin 81) as potential surrogate markers for tumor subtype in PDAC. They found that HFN1A was associated with the exocrine-like subtype and comparably good survival, while KRT81 was indicative of the quasimesenchymal subtype and worse survival. Tumors that did not show significant staining for either marker were named “double negative”, were attributed with the classical subtype and exhibited intermediate survival (Noll, Eisen et al. 2016). Building on these results, Muckenhuber et al. proposed a diagnostic algorithm further clarifying subtype classification (Muckenhuber, Berger et al. 2018) and made similar observation regarding survival of the patients. Additionally, Kalimuthu et al. proposed a morphologic evaluation algorithm using H.E. stained histology of PDAC that was also indicative of translational subtypes differentiating between gland-forming and non-gland-forming components which were associated with the classical and quasimesenchymal subtype respectively (S, Wilson et al. 2020).

In this study, randomly selected patients from the cohort of Muckenhuber et al. were chosen and their tumors were stained for H.E., KRT81 and MCT4. It is the aim of this study to evaluate the ties between morphological and immunohistochemically determined subtypes of human PDAC and their relation to MCT4 expression in order to gain insights into the role IHC staining for MCT4 may play in the future as a biomarker and biological reference for metabolic imaging in PDAC.

2. MATERIALS & METHODS

This study is descriptive, exploratory and retrospective regarding case selection. It involves different staining modalities (H.E. and IHC). The human probes were chosen at random from TMAs stemming from the collective created by Muckenhuber et al. (2018). Therefore, detailed information about the patient collective may be found there. The following Materials and Methods section focuses on the performed procedures on these datasets.

2.1 STUDY COLLECTIVE

The study collective is congruent with the one described in Muckenhuber et al (2018): 262 individuals with primary resected PDAC between 1991 and 2006 that received partial pancreatoduodenectomy at the Charité University Hospital (Berlin, Germany) were included in the histologic analysis. The data usage was approved by the Institutional Review Board (IRB; ethics committee) of the Charité University (EA1/06/2004). Secondly, 130 individuals that underwent elective pancreatic resection at the department of Surgery at the Klinikum rechts der Isar of the Technical University of Munich (Munich, Germany) between 2007 and 2011 (The data usage was approved by the Institutional Review Board (ethics committee) of the TU Munich, Germany (documents no. 1926/2007 and 126/2016 S)) and 125 patients with histologically proven PDAC that received primary chemotherapy (data usage was approved by the IRB (ethics committee) of the University of Heidelberg - nr. 160277) were considered.

Histologic analysis was performed on 5 TMAs gained from the study collective. The TMAs were prepared the following: Two to three tumor cores (1.0mm – 1.5mm) of representative tumor areas – chosen by a pathologist – were newly arranged in a paraffin block.

From these 10 patients with a HFN1A positive tumor, 10 patients with a double negative and 10 patients with a KRT81 positive tumor were randomly selected and their tumor cores analyzed. Three tumors (one of each group) were not present in the TMAs as expected; therefore, they were omitted and analysis was performed on 9 tumors of each subgroup respectively in order to prevent subjective case selection.

2.2 IMMUNOHISTOCHEMISTRY

TMAs of the collective described in Muckenhuber et al. (2018) were stained with Mayer's hematoxylin and eosin (H.E.), according to a standard protocol for tissue visualization (1. Xylol 2x 2min; 2. 100% Ethanol 1 min; 3. 96% Ethanol 1 min; 4. 70% Ethanol 1 min; 5. Desalinated water 30 s; 6.Mayer's hematoxylin 8 min; 7. Rinse with water 10 min; 8. Eosin solution 5 min; 9. 96% Ethanol 25s; 10. Isopropanol 25 s; 11. Xylol 1,5 min).

For immunohistochemical (IHC) stainings human TMAs were send to the Pathology department of the Technical University of Munich and stained in the laboratory of PD Dr. Katja Steiger. FFPE slices were pretreated 30 min with citrate buffer pH=6.0 and stained with antibodies against GLUT1 (rabbit, 115730, 1:750, Abcam, USA), MCT4 (rabbit, sc-50329, 1:150 for mPDAC, mouse sc-376140 1:150 for hPDAC, Santa Cruz Biotechnologies, USA) and KRT81 a Bond RXm system (Leica Biosystems, Wetzlar, Germany). Antibody binding was detected using DAB as chromogen after pre-incubation with respectively Bond Polymer Refine Detection Kit (Leica). Nuclei were counterstained with hematoxylin. All slides were digitalized using Aperio Scanner (Leica).

2.3 ANALYSIS OF HISTOLOGY AND IHC

Representative images of the tumor cores were taken and classified morphologically regarding their growth pattern as proposed by Kalimuthu et al. (2019) into gland-forming (conventional or tubulopapillary growth pattern) and non-gland-forming (composite or squamous). Due to the sole evaluation of the tumor cores, the evaluation was slightly adapted from the one described in Kalimuthu et al. (2019) as the structure defining morphology was chosen without determining quadrants.

For immunohistochemical subtyping the definite classification by Muckenhuber et al. was chosen. Medium or strong staining for HFN1A was decisive for classifying a tumor as *HFN1A positive*. If over 30% of the tumor cells by eyeball-evaluation were *KRT81 positive*, the tumor was classified as such. When both criteria were not met, the tumor was classified as *double negative*.

Regarding MCT4 staining it was measured quantitatively using a Positive pixel count (PPC) from the IAT further described in the Appendix (VII.4) as well as qualitatively determining MCT4 positive tumors with medium or strong staining of tumor or stromal cells for MCT4.

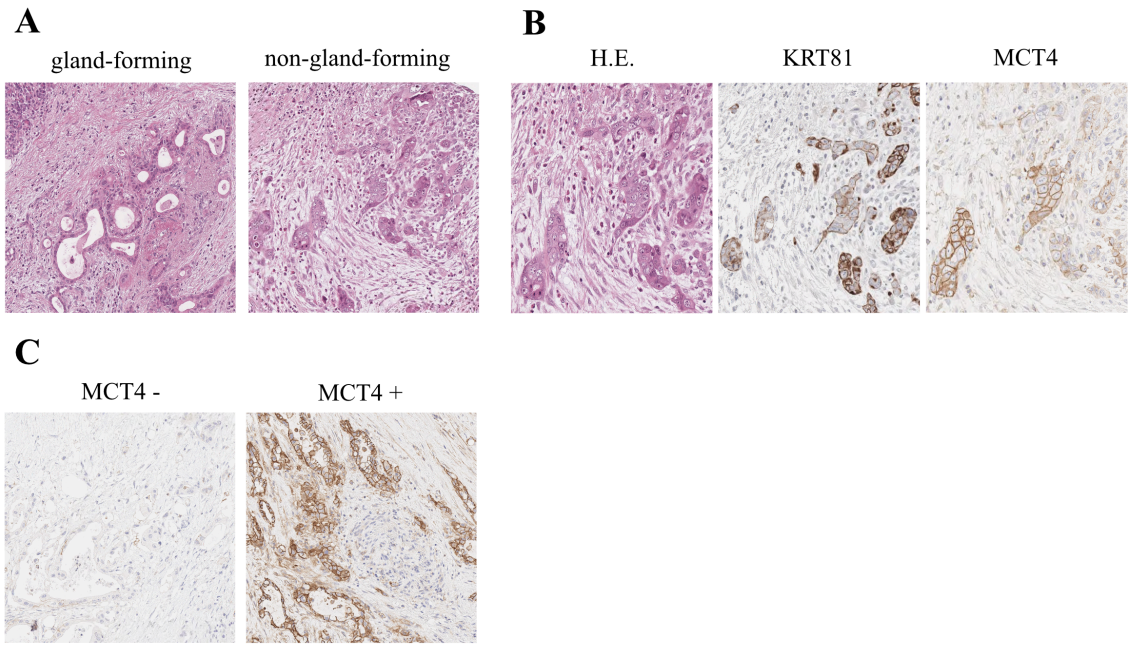

Fig.V-1: Classification and evaluation of tumors ***(A)*** *Morphological classification into gland-forming and non-gland-forming* ***(B)*** *Corresponding staining and analysis of H.E., KRT81 and MCT4* ***(C)*** *Examples of MCT4 negative and MCT4 positive tumors*

2.4 Statistical analysis

Statistical analysis was performed in GraphPad Prism (version 7 and 8, GraphPad Software Inc., San Diego, CA). For all statistical tests, a level of significance of 5% was used. A two sided Student's t-tests were performed for group comparisons of normally distributed quantities. Data presented as mean values including standard deviation or 95% confidence interval (95%-CI).

3. Results

A correlation between morphologic growth patterns and subtypes determined by IHC can be found

The data shows an association between morphological growth patterns derived from the descriptions of Kalimuthu et al. (2019) and subtypes based on IHC first hinted by Noll et al. (2016). From 27 evaluated human PDACs, 9 were classified as HFN1A positive, 9 as double negative and 9 as KRT81

positive. Of these, 16 tumors were defined by gland-forming growth of the tumor cells and 11 were defined by non-gland-forming growth (see Fig.V-2 A).

Gland-forming growth (conventional or tubulopapillary - associated with longer survival) is more frequently the defining pattern in HFN1A positive or double negative tumors. In contrast, KRT81 positive tumors are mainly defined by non-gland-forming growth (composite or squamous) of tumor cells. However, a portion of tumors exceeds the classification matrix of either nomenclature as tumors with non-gland-forming growth are also found in HFN1A positive and double negative tumors and vice versa (see Fig.V-2 B).

MCT4 expression is strongly associated with morphologic subtypes previously described by Kalimuthu et al.

MCT4 expression is significantly correlated to morphologic growth patterns ($p = 0.035$) such as gland-forming and non-gland-forming growth (see Fig.V-2 C). Also a strong overlap of MCT4 expression patterns and IHC defined subtypes HFN1A positive, double negative and KRT81 positive could be found (see Fig.V-2 E). Interestingly, only a few outliers were observed and they indeed showed different biological characteristics than the rest of the study collective. One tumor with high MCT4 expression that was classified as gland-forming in terms of morphology did show only marginal tumor expression of MCT4 but relevant MCT4 expression in adjacent stroma. Only one other tumor of the study collective amongst the KRT81 positive tumors did show high levels of stromal MCT4 expression. Two other outliers in terms of unusually high MCT4 expression were identified amongst the HFN1A positive and double negative tumors. They were both characterized by non-gland-forming growth, which was identified as rather unusual for these tumor subtypes (see Fig.V-2 D & F).

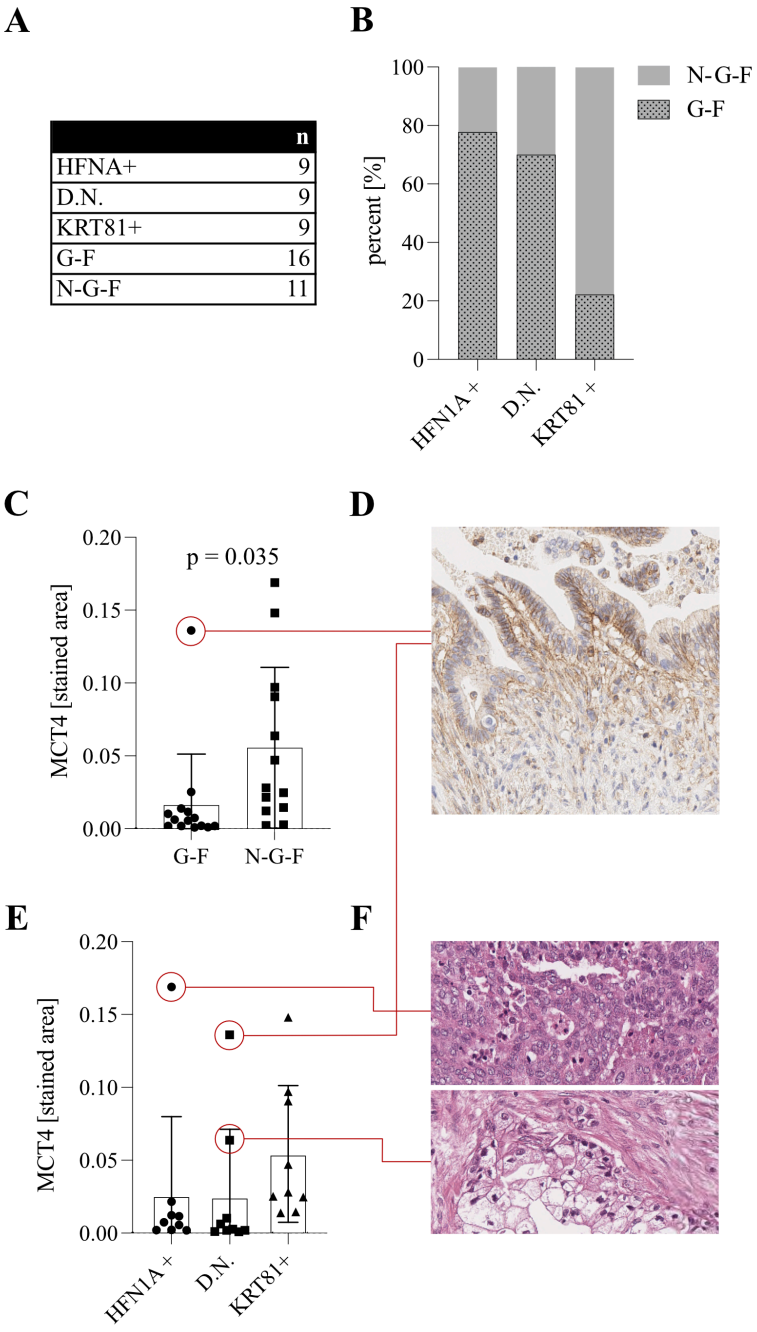

Fig.V-2: MCT4 expression in association to established histologically determined subtypes of hPDAC ***(A)*** *Tabular overview over established subtypes in the study collective (D.N. = double negative, G-F = gland-forming, N-G-F = non-gland-forming)* ***(B)*** *Association of gland-forming (G-F) and non-gland-forming growth (N-G-F) with IHC determined subtypes* ***(C)*** *MCT4 expression in gland-forming (G-F) and non-gland-forming (N-G-F) tumors* ***(D)*** *MCT4 staining with stromal emphasis of outlier in C (marked by red circle)* ***(E)*** *MCT4 expression in IHC determined subtypes* ***(F)*** *H.E. stained histology of outliers in E (marked by red circle)*

Distinct spatial expression patterns of KRT81 and MCT4 suggest specific biological meaning

The quantitative data derived from the study collective was indicative of an association of MCT4 and KRT81. However, a closer look into corresponding tumor packs in the differentially stained slides revealed that although KRT81 and MCT4 were correlated in their quantitative expression levels, they were merely expressed spatially separated from each other. In pancreatic cancer the subcellular distribution of KRT81 in tumor cells is cytoplasmic with often pronounced staining at the cellular borders. Staining for MCT4 mainly reveals membranous color reactions, as it is a substrate transporter located in the outer cell membrane. Nevertheless, mainly in stromal or some tumor cells also a cytoplasmic staining of MCT4 can be found. These considerations lead to the observation that membranous staining for MCT4 is associated with no or at least only cytoplasmic staining for KRT81. Should KRT81 staining be pronounced at the tumor cell borders, MCT4 staining was mainly found in the cytoplasm. In tumor cell clusters that were both MCT4 and KRT81 positive, the regions of intense staining for these two biomarkers were not overlapping but would be separated (see Fig.V-3 A-C).

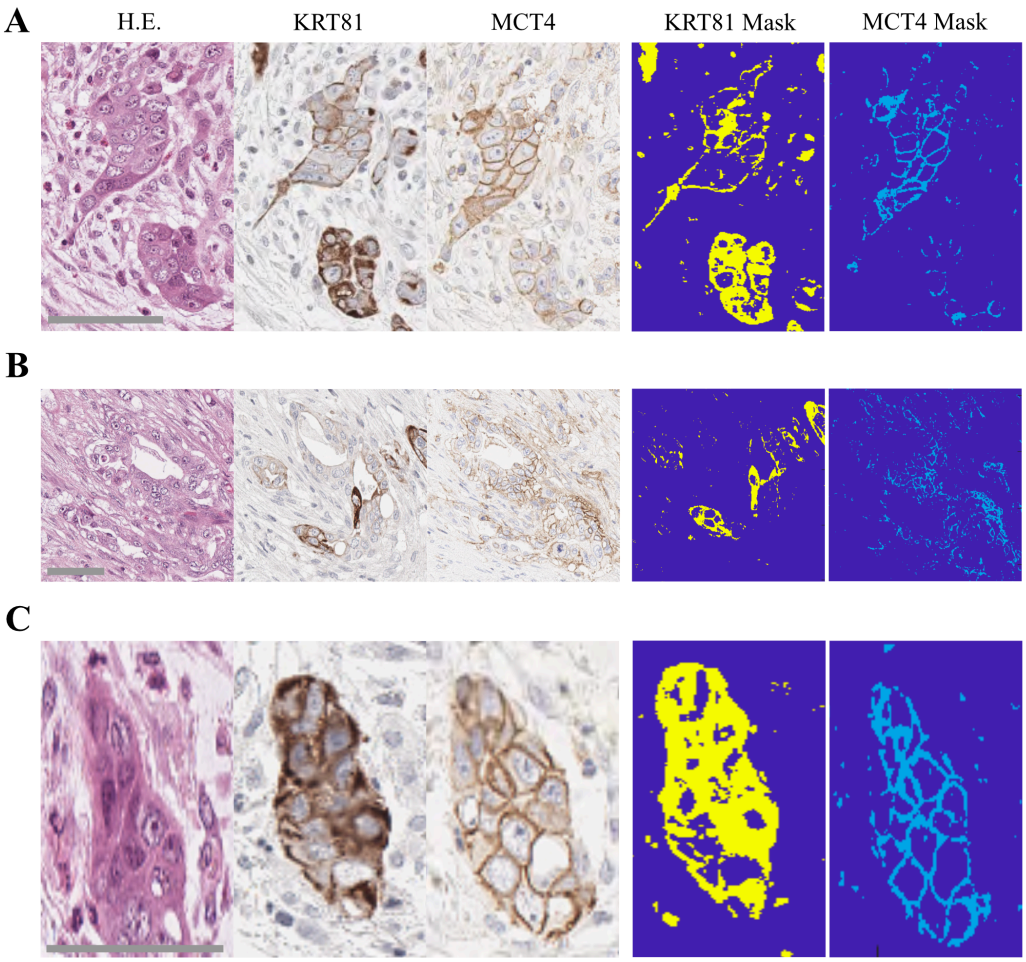

Fig.V-3: Spatial distribution of KRT81 and MCT4 staining (grey scale-bar equals 75 µm) ***(A-C)*** *Examples of corresponding tumor nests stained with H.E. (left) and (from left to right) for KRT81 and MCT4 and their respective masks that illustrate the differential expression patterns of KRT81 and MCT4*

4. Discussion

In this work, an association between spatial MCT4 expression (measured in IHC) and known subtypes of human PDAC was shown. MCT4 expression coincides with non-gland-forming growth of tumor cells and levels of KRT81 expression. Therefore, it is demonstrated that increasing levels of MCT4 expression are indicative of more malignant subtypes and worse survival. This is congruent with results published previously for pancreatic cancer (Baek, Tse et al. 2014, Kong, Nøhr-Nielsen et al. 2016). Furthermore, it has been shown that there is a significant overlap between morphologically

determined subtypes (S, Wilson et al. 2020) and subtypes defined by IHC expression (Noll, Eisen et al. 2016, Muckenhuber, Berger et al. 2018).

This data classifies MCT4 as a biomarker not only indicative of metabolism but further disease defining characteristics. The prognostic value of MCT4 expression has been described for tumor as well as stromal expression (Baek, Tse et al. 2014). Therefore, MCT4 may even have advantages over mere morphological or IHC based subtyping as the discussed outliers (Fig.V-2 D & F) demonstrate. Limits in terms of diagnostic meaning of this study can be seen in the relatively small sample size and the retrospective study design.

5. CONCLUSION

To conclude, it has been shown by these evaluations and literature that MCT4 can be considered a valuable biomarker with diagnostic and prognostic value for human PDAC. Furthermore, the previous chapters of this work highlighted the relevance of MCT4 as an ex-vivo reference for metabolic imaging. This leads to the conclusion that in the wake of individualized medicine and tumor characterization, the ongoing establishment of metabolic imaging in standard diagnostics and pressing need for substantial predictive biomarkers in PDAC, the immunohistochemical determination of MCT4 expression status will gain meaning in the future.

VI. CONCLUSION

In this work the feasibility and biological meaning of 1-^{13}C-pyruvate MRSI in endogenous murine PDAC was evaluated. As a potentially powerful metabolic imaging modality measuring the pyruvate-to-lactate conversion rate in vivo, 1-^{13}C-pyruvate MRSI has already been translated into the studies of human prostate cancer (Nelson, Kurhanewicz et al. 2013, Tayari, Heerschap et al. 2017). Nevertheless, its broad application in human PDAC will be dependent on diagnostic power due to high technical requirements and elaborate execution of data acquisition. Therefore, this work sought to identify the biological basis of the measured conversion rate and found that in-vivo data could be referenced to MCT4 expression of pancreatic tumors. This positioned MCT4 at a theoretical lever, as the future relevance attributed to 1-^{13}C-pyruvate MRSI could be dependent on the diagnostic specificity of MCT4 and its future meaning as a biomarker in human PDAC. Therefore, Parts Two (IV.) and Three (V.) sought to further characterize this biomarker with its ties to morphologic determinants and its expression patterns in human PDAC. It is concluded that MCT4 is a viable candidate for a prognostic

ex-vivo biomarker for human PDAC and a suitable reference for 1-^{13}C-pyruvate MRSI data. Nevertheless, several identified obstacles will have to be overcome on the way to clinical application of 1-^{13}C-pyruvate MRSI. These are mainly summarized by the vast structural heterogeneity of human PDAC, its low tumor cellularity compared to murine models, its high recruiting of desmoplastic stroma and its low as well as locally differing perfusion. These factors combined will render interpretation of 1-^{13}C-pyruvate MRSI data complex in human PDAC. Therefore, I believe that the implementation of multimodal imaging protocols involving the assessment of morphologic, micro-structural and metabolic determinants and the consideration of the patients' specific clinical data will be the only way to sensibly characterize human PDAC in vivo and thereby set directions for individual therapeutic options.

VII. APPENDIX

1. CONTRIBUTIONS

Undoubtedly science is a team effort. That is why contributions of people working with me are noted and acknowledged below:

IV. Part One	
Irina Heid and Geoffrey Topping	Parts of 1-^{13}C-pyruvate MRSI measurements
Sybille Reder and Markus Mittelhäuser	^{18}F-FDG PET imaging
Katja Peschke	IF staining of cell culture
Katja Steiger and Iryna Skuratovska	Immunohistochemical staining of histological slides
Irina Heid	Valuable scientific input regarding the planning and implementation of the experiments as well as data interpretation
Rickmer Braren	Valuable scientific input regarding interpretation of obtained data
VI. Part Two	
Katja Peschke	Maintaining and IF staining of cell culture
Katja Steiger and Iryna Skuratovska	Immunohistochemical staining of histological slides
Irina Heid	Valuable scientific input regarding data interpretation
VII. Part Three	
Katja Steiger and Iryna Skuratovska	Immunohistochemical staining of histological slides
Alexander Muckenhuber	Providing TMAs & subtype classification
Irina Heid	Valuable scientific input regarding experimental setup and data interpretation

Table VII-1: Contributions

2. MAGNETIC RESONANCE IMAGING

Protons are positively charged and spin around their own axis. When a magnetic field is applied the spins align parallel or anti-parallel with the magnetic field. Slightly more spins align parallel because the parallel alignment is a state of lower energy. The energy difference between the parallel and anti-parallel state is proportional to the gyromagnetic ratio, Planck constant and the strength of the magnetic field. Therefore, the stronger the applied magnetic field is, the more spins are aligned parallel to the magnetic field. That is why the sum of all single spins in a magnetic field can be described as a vector (sum of all parallel and anti-parallel vectors) parallel to that field.

For the spinning proton is a moving charge it can induce a current in a receiver coil. The frequency of that current is the same as the precession frequency of the spin in the magnetic field (= Lamor frequency). The Lamor frequency is proportional to the gyromagnetic ratio and the magnetic field. Therefore, the frequency of the induced current is lower in a magnetic field with lower magnetic flux density and higher in a stronger magnetic field.

MRI is based on the principle that a body is introduced to a steady magnetic field (B_0). The spins align with the magnetic field: A magnetization parallel to the magnetic field (M_z) is being built up.

By applying a radiofrequency-pulse at Lamor frequency the spins can be excited. By adjusting power and duration, the magnetisation may be flipped e.g. 90° into the xy-plain (M_{xy}). There, the spins induce a current into a receiver coil with Lamor frequency.

Relaxation describes in which manner the spins return to their steady state after the excitation. With increasing time magnetisation returns into the Z-direction. As the projection of the magnetisation on the xy-plain decreases the MR-signal diminishes. The time constant describing the velocity of the longitudinal relaxation (increasing M_z) is called T_1. The MR-signal decreases faster than M_z is returning. This is due to transversal relaxation. After the excitation spins precess in coherence with each other. Due to spin-spin interactions the spins dephase. The time constant describing the loss of M_{xy} is called T_2.

As the relaxation of Protons in macromolecules is very fast, only protons of water molecules generate the vast majority of measurable MR-signal.

2.1 T_2-WEIGHTED MRI

The sequences of T_2-weighted images are designed in a manner that the signal is mainly influenced by transversal relaxation. Echo-Time (TE) describes the time span from the excitation of the spins to the

measurement of the echo. The T_2 of tissues is different due to their structure. They mainly range from 30-100 ms. To receive an image where the contrast is mainly based on the differences in transversal relaxation rates a measurement is suitable where some tissues show high relaxation whereas others show little transversal relaxation. As transversal relaxation is the main cause for MR-signal loss, TE is a good parameter to adjust the influence of T_2 on image contrast. However, T_1, proton density and other properties (perfusion, diffusion etc.) still have a large influence on the generated image.

2.2 DIFFUSION-WEIGHTED MRI

Diffusion-weighted imaging (DWI) measures the displacement of water molecules in tissue. As the displacement is dependent on the microstructural composition of tissue (such as cell membranes, the distribution of cellular compartments, perfusion and macromolecules), DWI may give important insights into the structure of PDAC.

Diffusion of molecules is caused by random collisions of molecules in movement. Fick's law describes diffusive flux being dependant on the concentration gradient and the diffusion coefficient. But even in thermal equilibrium random movement of molecules (Brownian Motion) causes non-directional diffusion, however there being no net flux on a bigger scale.

Generally, in order to generate a Spin Echo (SE) two RF pulses are applied. The first RF pulse tilts magnetisation in the transverse plain. There spins dephase as described above. Due to inhomogeneities of the external magnetic field some spins precess faster (if they are exposed to a greater local magnetic field) than others (T2*). When a 180° RF-pulse is applied this system reverts. The spins that precess faster are now not in front of the other spins but behind. But as the T2*-effects are still present, this system is symmetrically reversible. Once the faster precessing spins "catch up" the spins show phase coherence. A SE can be measured as described by Brewer et al. in 1984.

When gradients are applied, spins at different positions experience different magnetic fields and therefore show different precession. If spins diffuse, the above-mentioned reverse symmetry is decreased. The MR signal of the SE is reduced. It can be followed that the more spins diffuse the smaller the measurable MR-signal of the SE gets as explained by Carr et al. in 1954.

There are three major possibilities to influence the effects of diffusion on the MR-signal: Strength (G) and duration (∂) of the applied gradients and the time interval between them (Δ).

This sensitivity to diffusion is quantified by the b-value as defined by Stejskal et al. in 1965:

$$b = \gamma^2 * G^2 * \delta^2(\Delta - \delta/3)$$

Formula VII-1: b-value

By acquiring multiple diffusion-weighted-images with differing b-values, the apparent diffusion coefficient (ADC) can be calculated. Thereby, the influence of other contrast determining parameters is drastically diminished.

The b-value quantifies the influence of diffusion on signal intensity. The higher the b-value, the more diffusion weighting is performed. With higher b-values the signal intensity decreases. There are deviations from the expected monoexponential shape of signal decay in low and high b-values. Considering low b-values, this deviation from the expected shape of the curve can be explained by flowing blood. This entails the possibility to estimate perfusion of the tissue (Riches, Hawtin et al. 2009). Deviations in the range of high b-values can be explained by the separation of extra- and intracellular (and intranuclear) compartments with different diffusion properties (Mulkern, Barnes et al. 2006).

Above, Brownian motion was described as a random motion of all molecules proportional to temperature. If the movement is truly random and a large number of molecules are observed, the squared displacement of molecules is proportional to the observation time as described by Einstein in 1905. The distribution of the squared displacement can be characterized by a Gaussian curve. In-vivo free isotropic diffusion is impaired by bio-membranes and structural proteins. Therefore, the mean squared displacement of water molecules is reduced. Conclusively obstacles of diffusion that result in reduced ADC values can provide valuable insights into the architecture of the tissue.

A basic pulse sequence of DWI is described above. Gradients are used so that spins of different position, precess at different frequencies. If there were no movement of spins, phase coherence would be restored after the second gradient pulse. An intense SE would be measured. However, all spins show random movement. The further they get displaced the stronger the phase dispersion gets. This leads to a decrease in signal amplitude depending on displacement and therefore apparent diffusion.

As the squared displacement is proportional to the observation time, the observation time is one factor to increase diffusion weighting. This is expressed in the b-value (see above). When multiple signal amplitudes are measured with different b-values, a bi-exponential model can fit the ADC-value (Langkilde, Kobus et al. 2018).

$$S(b) = S_0 * e^{-ADC*b}$$

Formula VII-2: 2-Parameter model of ADC

In tissues, there are structural barriers that hinder free isotropic diffusion. Membranes, organelles and macromolecules may be considered the most prominent. Knowledge of a tissues' content of such barriers provides valuable insights. The more barriers a tissue contains, the lower its ADC value is set out to be. That is why solid cancerous tissue often displays lower ADC values than healthy tissue. In healthy tissue, extracellular matrix allows water molecules to diffuse with little obstacles. In cancerous tissue the impact of cancer cells increases the hindering aspect of cell membranes on diffusion. Cancer cells show a different shape, tighter growth pattern and therefore higher density than stroma cells.

Especially in mPDAC activated stroma cells and immune cell infiltration can lead to relevant deviations from that simple consideration. Furthermore, water filled ductal structures may increase ADC values measured in neoplastic tissue. Furthermore, fibrosis, edema, necrosis and intratumoral vessels play important roles considering diffusive restriction.

As described above the observed signal decay observed in spin echo experiments is mainly attributed to diffusion. But there are also other contributors. Different compartments (intracellular, extracellular, intravascular) show varying displacement of spins. Blood flow displaces spins faster than the diffusion rate in the extravascular space. Therefore, ADC values fitted with low b-values include influence of microvascular perfusion, whereas ADC values fitted with high b-values will only show marginal influence of perfusion. In the following a parameter (ADC_{perf}) value indicative of microvacular perfusion was proposed (Teruel, Goa et al. 2016).

$$ADC_{perf} = ADC_{0,200} - ADC_{200,700}$$

Formula VII-3: ADC_{perf}

Equivalently in this work a perfusion sensitive ADC will be referred to calculated as shown below:

$$ADC_{perf} = ADC_{12,215} - ADC_{418,1529}$$

Formula VII-4: ADC_{perf} equivalent

Based on a similar proposal the simplified perfusion fraction = SPF (Cao, Suo et al. 2017) is calculated as follows:

$$SPF = ADC_{perf}/ADC_{12,215}$$

Formula VII-5: SPF

2.3 1-^{13}C-PYRUVATE MRSI

1-^{13}C-pyruvate MRSI is an imaging modality that exploits the variation of resonance frequency of ^{13}C when it is incorporated in different molecules (such as pyruvate, lactate and alanine). Thereby, the conversion from pyruvate (that is injected) to lactate (and alanine) can be measured over time. As these reactions lie at an important fork in metabolism, the characterization of these metabolic properties may have important implications for PDAC classification.

The differentiation of 1-^{13}C-Pyruvate and its metabolites is possible as the electrons surrounding the ^{13}C-nuclei partially shield the nuclei from the external applied magnetic field and thereby changing its local properties. This results in changes of resonance frequencies of the nuclei dependant on local electron density, which is determined by bindings and geometry of the examined molecule.

As resonance frequencies are proportional to the gyromagnetic ratio and the strength of the magnetic field, local changes of the magnetic field result in changes of resonance frequencies.

This variation of resonance frequency caused by different incorporation of the same nuclei in different molecules is referred to as chemical shift (Harris, Becker et al. 2002). In the analysed spectra of this work the relevant metabolites 1-^{13}C-pyruvate, 1-^{13}C-alanine and 1-^{13}C-lactate are displayed.

The receivable signal is dependent on degree of polarisation, concentration of the metabolites, flip angle, repetition time, number of RF-pulses and T_1-relaxation time.

With the development of dynamic nuclear polarisation (DNP) it has been rendered possible to gain highly polarized nuclear spins in solution (Ardenkjaer-Larsen, Fridlund et al. 2003). This has made in vivo studies with ^{13}C-labeled molecules possible by overcoming the lack of sensitivity resulting from low concentrations compared to ^{1}H. To achieve the described hyperpolarized state of the nuclear spins, 1-^{13}C-pyruvate is mixed with a stable radical, (which provides free electrons) and cooled to ~1K with a high magnetic field applied. Then microwave irradiation transfers the free electrons' polarisation, which at this temperature and magnetic field approaches 100%, to the ^{13}C-nuclei (Ardenkjaer-Larsen, Fridlund et al. 2003). The dissolution process with heated TRIS-buffer yields a solvent at room temperature with considerable polarisation left that is directly injected into the mouse's tail vein and

enables time resolved chemical shift imaging. For polarisation is lost in dependence to T_1-relaxation time, imaging of 1-^{13}C-pyruvate is limited to fast reactions, including its reduction to lactate, its transamination to alanine or its decarboxylation catalysed by PDH.

1-^{13}C-pyruvate is a common substrate for metabolic studies, for it has a relatively long T_1 relaxation time, good solubility in water, its uptake and reaction kinetics are fast and it plays a central role in glycolytic metabolism.

After being injected into the tail vein, 1-^{13}C-pyruvate is transferred into the cells mainly via the monocarboxylate transporter 1 and 4 (MCT1 & MCT4). Then it can either be reduced to lactate, transferred to alanin or decarboxylated and enter the TCA-cycle. These first steps occur in every tissue of the animal. Of particular interest is the conversion to lactate. Lactate then is mainly being secreted by the tissue (e.g. liver, kidney, erythrocytes, tumor) and enters the blood flow again. Cancerous tissue which is known to use glycolysis for energy supply even in the presence of oxygen (aerobic glycolysis) often shows higher expression/activity of MCT1 and LDHA is therefore expected to absorb more lactate and metabolize it further. That is why tumors maybe could be characterized by their lactate signal as it hints MCT1, MCT4 and LDHA expression, which are important variables in tumor evaluation as described above.

An approach to quantify the conversion of 1-^{13}C-pyruvate to 1-^{13}C-lactate is the $AUC_{lactate}/AUC_{pyruvate}$ (AUC_l/AUC_p). As the utilized multiframe CSI (=1-^{13}C-pyruvate MRSI) sequence has a temporal resolution of 5-6 s the “area under the curve” is approximated by the cumulative sum of the signal intensities at different time steps.

A direct comparison of scans with differing SNR with a fixed time span is not sensible due to the calculation used to approximate the AUC_l/AUC_p. The cumulative sum of signal of a measurement with a low SNR and short signal over noise is proportionally more influenced by noise than a scan with high a SNR and longer signal over noise.

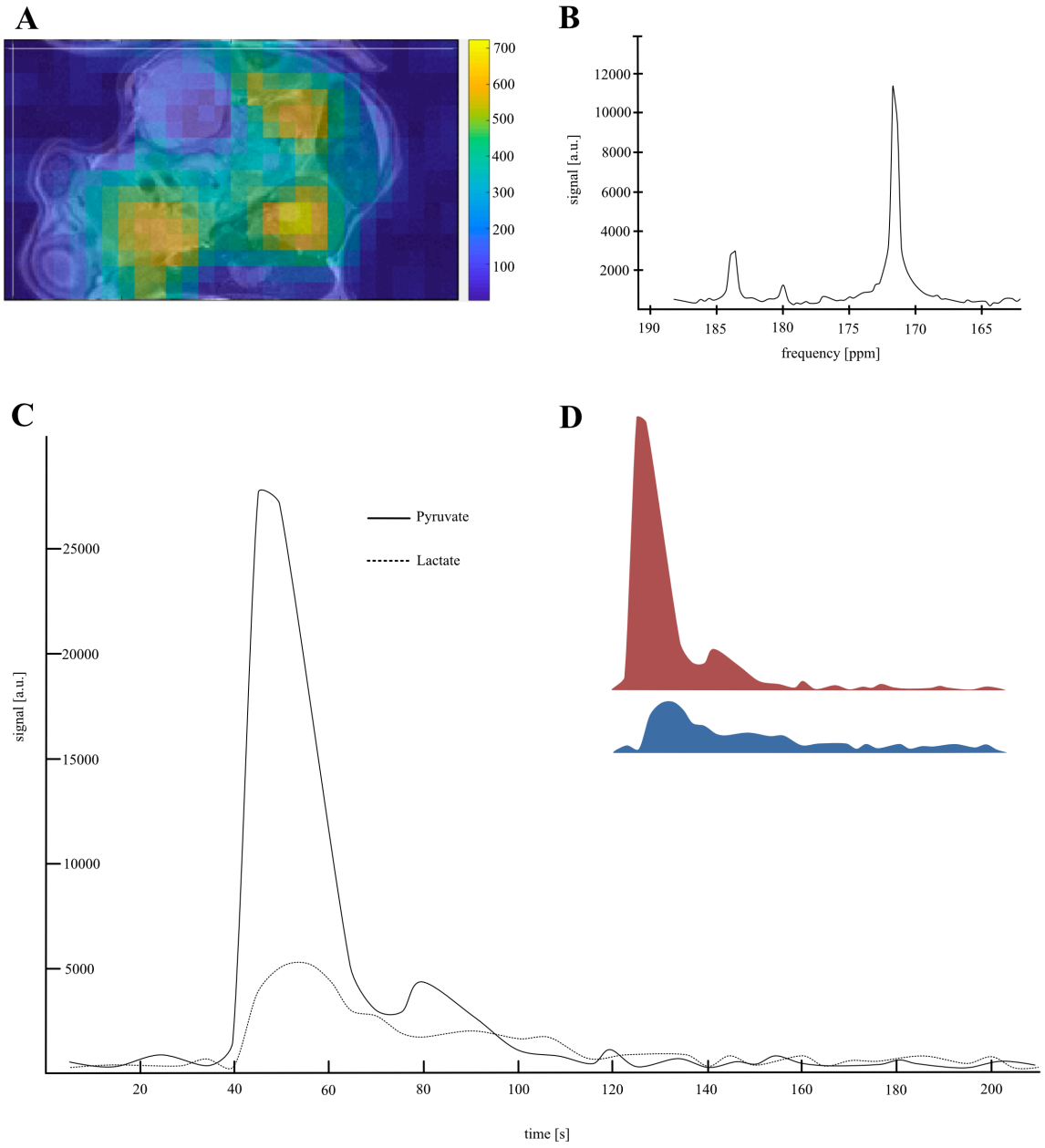

Fig.VII-1: Introduction to 1-^{13}C-pyruvate MRSI ***(A)*** *1-^{13}C-lactate abdominal image of a mouse* ***(B)*** *Spectrum of a tumor region acquired after injection of hyperpolarized 1-^{13}C-pyruvate. The peaks from left to right correspond to 1-^{13}C-lactate, 1.^{13}C-alanine and 1-^{13}C-pyruvate* ***(C)*** *Temporal display of the signal intensity of 1-^{13}C-pyruvate and 1-^{13}C-lactate acquired by multi-frame CSI* ***(D)*** *Coloured visualization of the AUC of 1-^{13}C-lactate (blue) and 1-^{13}C-pyruvate (red)*

3. POSITRON-EMISSION TOMOGRAPHY

PET imaging may localize positron emission in tissue after the injection of a positron-emitting nuclide. As in this work, mainly the role of glycolysis is analyzed, ^{18}F-FDG PET is an established platform to quantify PDAC's glucose uptake. In this chapter PET Imaging and ^{18}F-FDG are introduced.

PET is a functional imaging modality, using the pharmacokinetic properties of labelled tracers to gather functional information about the tissue of interest.

It uses the characteristics of β^+-decay of radionuclides in the body. An unstable nucleus emits a positron when a proton decays into a neutron, a positron and a neutrino. In the body the positron has a very limited life span: After loss of kinetic energy it will bind an electron just before annihilation. Annihilation describes the process of the mass of the electron and the positron being completely transformed into electromagnetic energy. This energy is emitted with photons. In the vast majority of cases it is two photons with an energy of 511 keV are sent out in the opposite direction because of energy and momentum conservation. Given this annihilation process, the described geometric pattern allows localisation of the annihilation site, which is due to the short-lived positron close to the emission site of the photon.

Nuclides with β^+-decay that are frequently used for PET are amongst others ^{18}F, ^{11}C, ^{13}N, ^{15}O, ^{62}Cu, ^{64}Cu, ^{68}Ga and ^{82}Rb. To produce a PET tracer, molecules of biological relevance are labelled with a radionuclide. The PET tracer is injected into the body. Depending on its pharmacokinetic it will be distributed in the body. Tissues with tracer accumulation will show a higher number of annihilations than parts with tracer depletion.

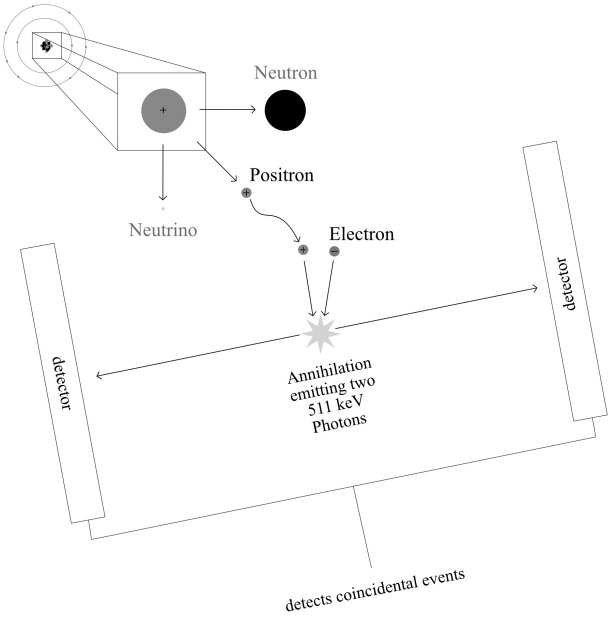

Fig.VII-2: Principles of PET

^{18}F decays via Positron-emission (HL = 110 min) as explained in further detail above. Glucose labelled with ^{18}F (=^{18}F-fluor-2-desoxy-glucose) is commonly used as PET tracer as it exploits the diagnostic possibilities that malignant tissues often have an enhanced glucose metabolism.

Among others, the widespread KRAS mutations lead to increased glycolytic flux, underlining the relevance of ^{18}F-FDG as a tracer for PDAC. First, it is transported by convection within the blood stream reaching tissues during the enrichment phase. Second, it is absorbed by cells via glucose-transporters. Then it is phosphorylated but cannot be metabolised by glycolytic enzymes downstream of this reaction. Due to the phosphorylation it is also hindered from exiting the cell (= metabolic trapping). Therefore ^{18}F-FDG accumulates in tissues of increased glycolytic flux.

However, multiple limitations arise from these thoughts. First, increased ^{18}F-FDG uptake is not specific to malignancies. It is also found in inflammatory processes (Murakami 2011). Therefore it is not surprising that uptake values often show non-satisfactory separation between PDAC and chronic pancreatitis due to similar molecular pathways being activated (Evan, Hah et al. 2017).

4. Image Analysis Tool

4.1 Interface

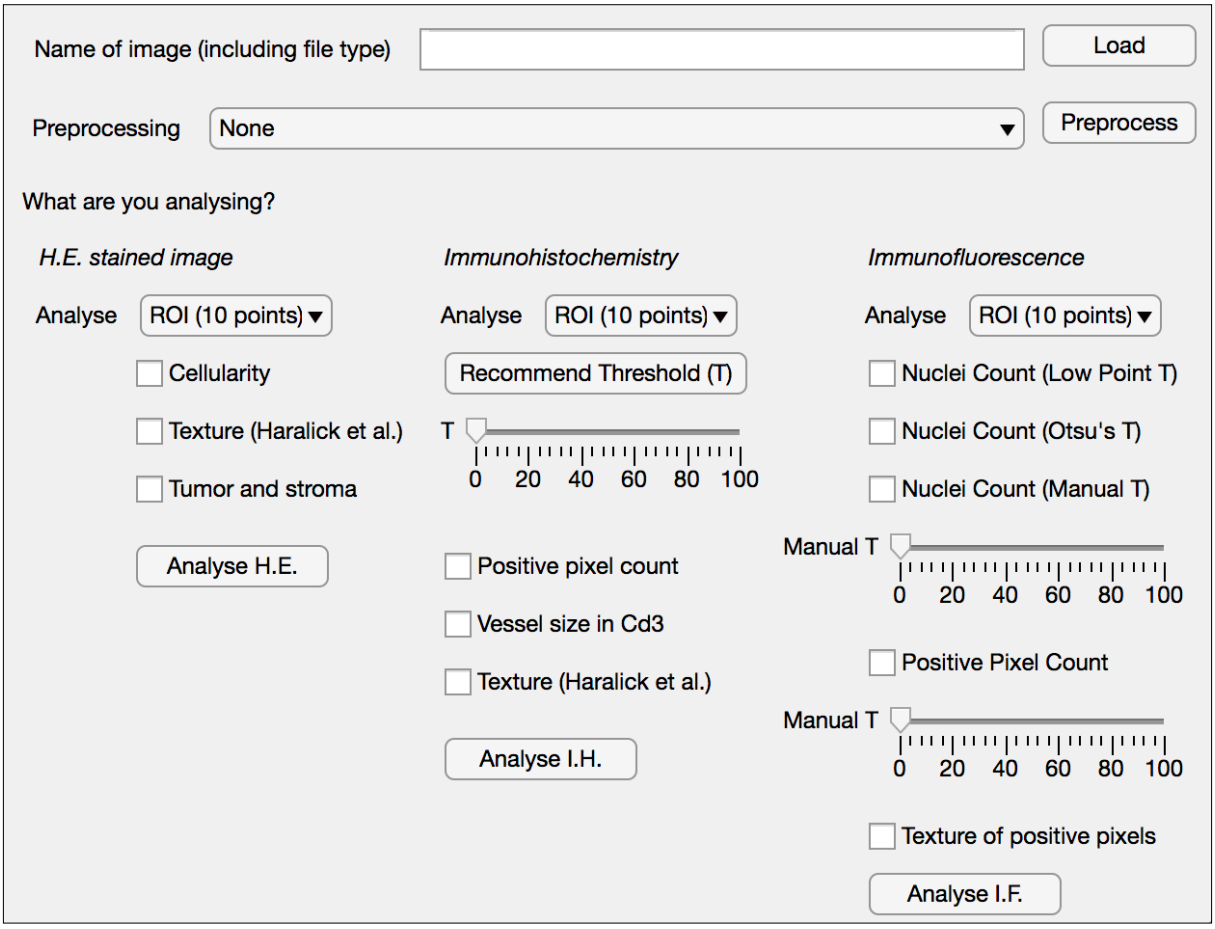

Fig.VII-3: Interface of the Image Analysis Tool

4.2 Pre-Analysis

After reading the image, preprocessing can be performed if wanted. Using the tool, it can be chosen from linear normalization and Gaussian filtering.

Linear normalization in this context adjusts the pixels in a desired range. This range can be adjusted using the desired minimum and maximum values. It is calculated using the following formula:

$$I_n = (I - Min_n)\frac{Max_n - Min_n}{Max_o - Min_o} + Min_n$$

Formula VII-6: Linear normalization

where I_n is the new pixel intensity, I is the old pixel intensity, Max_n is the new maximum value (e.g. 255), Min_n is the new Minimum value (e.g. 0), Max_o is the old maximum and Min_o the old minimum value.

Gaussian filtering is a filtering method to smooth a picture and deprive it of single noisy pixels, unwantedly influencing quantification results. It is performed with the built-in function *imgaussfilt(I,s)*, where the function filters an Image (I) with a 2-D Gaussian smoothing kernel with a standard deviation of s (sigma).

4.3 Analysis of H&E stained images

The analysis of H.E. stained images in this context was implemented to analyze the number of nuclei and cellular area in the image as well as receiving information about Haralick's texture parameters.

4.3.1 Cellularity

As proposed by Konstandiou et al. (Konstandinou, Glotsos et al. 2018) segmentation for nuclei was implemented by transforming the RGB image to grayscale. Then a Gaussian filter is applied. Additionally specific thresholding for nuclei was implemented: In order to do that the image was thresholded at x different thresholds. Values were plotted and the threshold of the plateau chosen. Then small regions out of 1.5 standard deviations were excluded to account for false positive regions. An output image using that threshold was generated including mostly the segmented nuclei.

4.3.2 Texture analysis

In the image analysis tool the GLCM derived texture descriptors ***Contrast*** – measures the local variations in the gray-level co-occurrence matrix – ***Correlation*** – measures the probability occurrence of the specified pixel pairs – ***Angular second moment*** – a marker of homogeneity – and ***homogeneity*** – measures the closeness of distribution in the GLCM – were included using the function graycoprops() by MATLAB.

4.4 Analysis of Immunohistochemistry

In the analysis of immunohistochemistry positive pixel count has an important status as it reliably quantifies the areal stain present. Areal stain does not necessarily correlate with antigen presence, especially when thresholding is done poorly or incoherently. That is why different implemented thresholding techniques are presented below as well as image processing for positive pixel count. As it often arises in related projects, the measurement of vessel lumina in CD31-stained images is also implemented in the tool and explained below.

4.4.1 Thresholding

Thresholding is the key step when quantifying immunohistochemical data using positive pixel count. Its importance and susceptibility to error is described in literature (Johnson and Walker 2015) but not broadly acknowledged. Little differences in defining a threshold can change results as a relevant subpopulation of pixels can be discarded or falsely included. That is why tedious attention to same laboratory conditions, antibodies, incubation times is crucial but can be in vain if thresholding is done poorly. In the Image analysis tool, the user can choose between manual thresholding (using the same threshold for a study set is imperative) and automated thresholding. As this suggests automated thresholding does not use the same threshold in every analysis but defines a threshold from a plot of the prospective number of positive pixels at different thresholds. This plot equals a cumulative threshold spectrum (CTS) as proposed by Johnson et al. If two subsets are compared, also their CTS may be compared for a more robust discrimination. If automated threshold is clicked, the threshold t-units after the steepest point of the CTS (in presetting t = 5) is chosen.

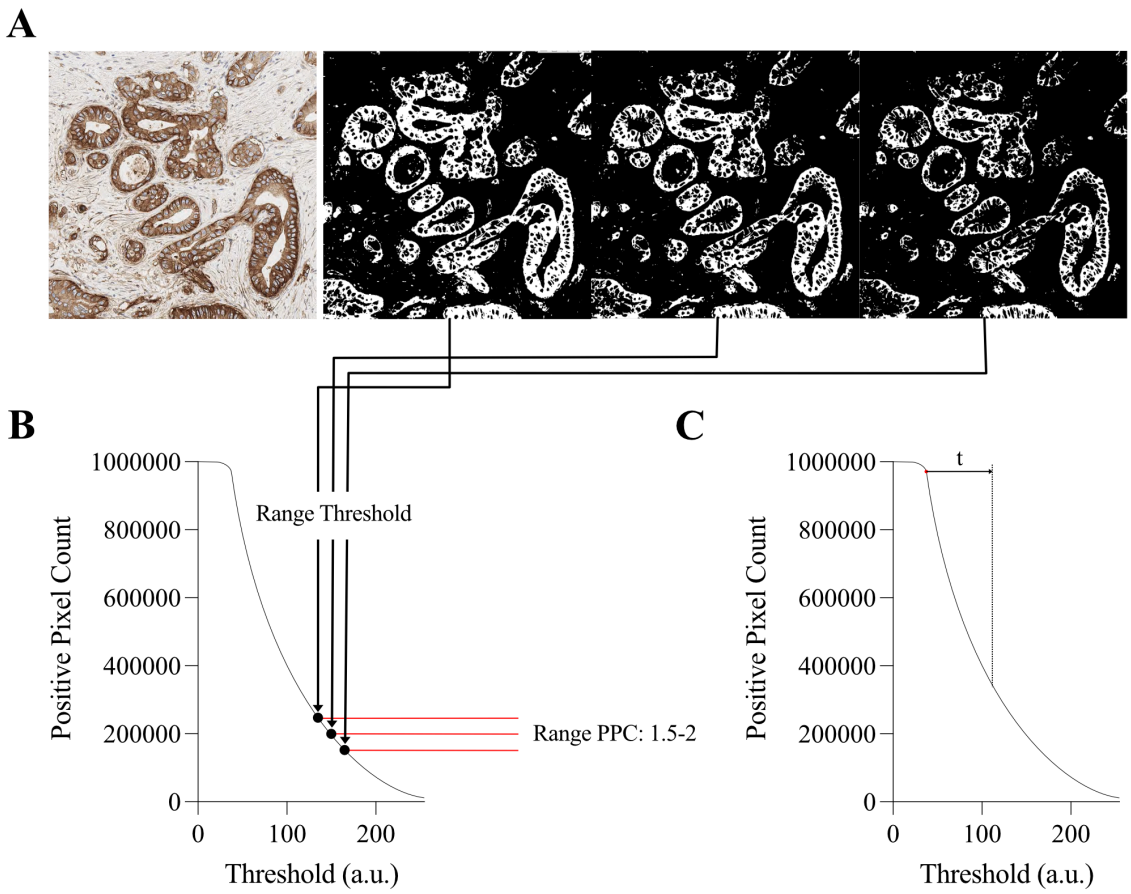

Fig.VII-4: Illustration of thresholding arbitrariness and implemented automated thresholding ***(A)*** *depicts possible and justifiable thresholding range by an individual examiner* ***(B)*** *Illustration of influence of differing thresholds on PPC* ***(C)*** *Illustration of Offset by t from turning point*

4.4.2 Cellularity

As the hematoxylin stain of nuclei is blue, a nuclear image is best generated removing the red color portion of the image. Subtracting the intensity values of the red channel from the ones of the blue channel of the image after Gaussian filtering does this. Using a Canny edge detection algorithm and filling the regions surrounded by the classified edges delivers a clear image showing nuclei. Their number is evaluated as well as their size and circularity. With this procedure a good correlation (r = 0.995, 95%-CI: 0.976-0.999) and little deviation (Mean Error = 4.9%) between manual and automated count was found.

Cellularity is then used to describe the number of pixels in relation to all that are occupied by nuclei. Histogram data such as Mean, Median, Standard Deviation, Skewness and kurtosis as well as textural

data (*Contrast*, *Correlation*, *Angular second moment*, *Homogeneity*; see IV.2.6.22) can be selectively drawn from the nuclei.

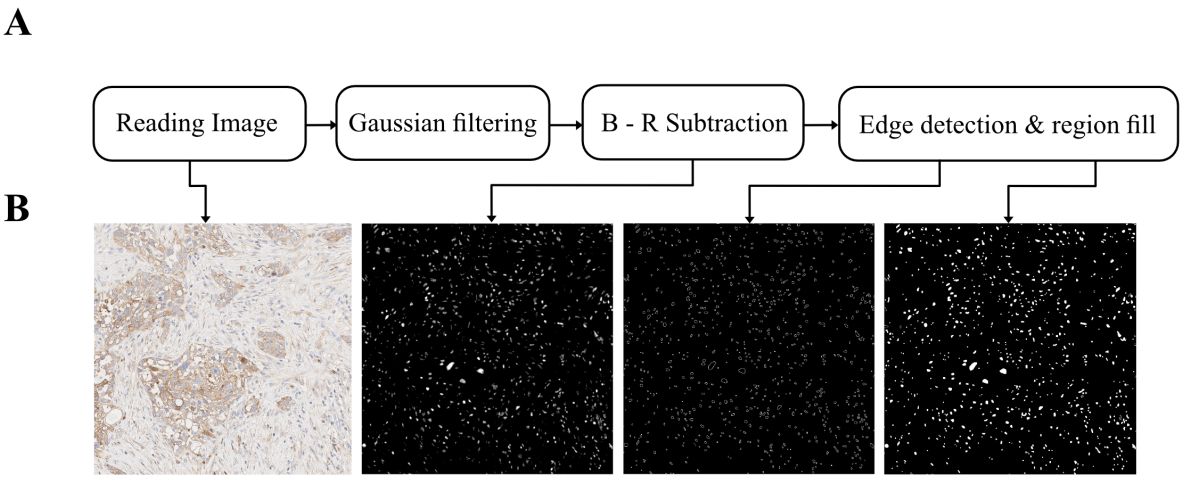

Fig.VII-5: Workflow for assessing cellularity in images of IHC ***(A)*** *Workflow* ***(B)*** *Exemplary images respective to workflow depicted in A (indicated by arrows)*

4.4.3 Quantification of Immunohistochemical Staining

Usually immunohistochemical stain is quantified using a positive pixel count (PPC). Thereby it is postulated that areal stain is proportional to antigen presence. It has been shown that this assumption is not entirely correct. However PPC's performance is satisfactory when evaluating expression on a larger scale or entire tumor region as in our context. It is implemented by counting all pixels classified as positive via thresholding methods explained above. Furthermore, staining can be quantified using staining intensities. This approach however is prone to error caused by inhomogeneous noisy staining. That is why only PPC is used to describe antigen expression in this study.

4.5 Measuring vessel size in CD31-stained images

In order to be able to assess sizes of vessel lumina in perfusion-fixed CD31-stained images a function was added to the analysis tool. In order to achieve that 2 masks are generated from the read image. One is generated using thresholding for the CD31 staining. This one can also be used to do a PPC of the CD31 staining that can be proportional to vessels present. This is helpful if the tissue is not perfusion fixed. Applying Canny's edge detection algorithm on an image that was segmented for

CD31 positive areas generates the second mask. By filling out the holes generated by the edge detection a binary image is rendered. Now pixels can be assigned a value conditional to their inclusion in positive areas of the first mask delivering an image depicting only vessel lumina: Their size and shape can be quantified. In a validation run including 5 representative images stained with CD31, a good correlation between manually outlined lumina and automatically measured vessels was found (r = 0.987, 95%CI = 0.813-0.999, p = 0.002).

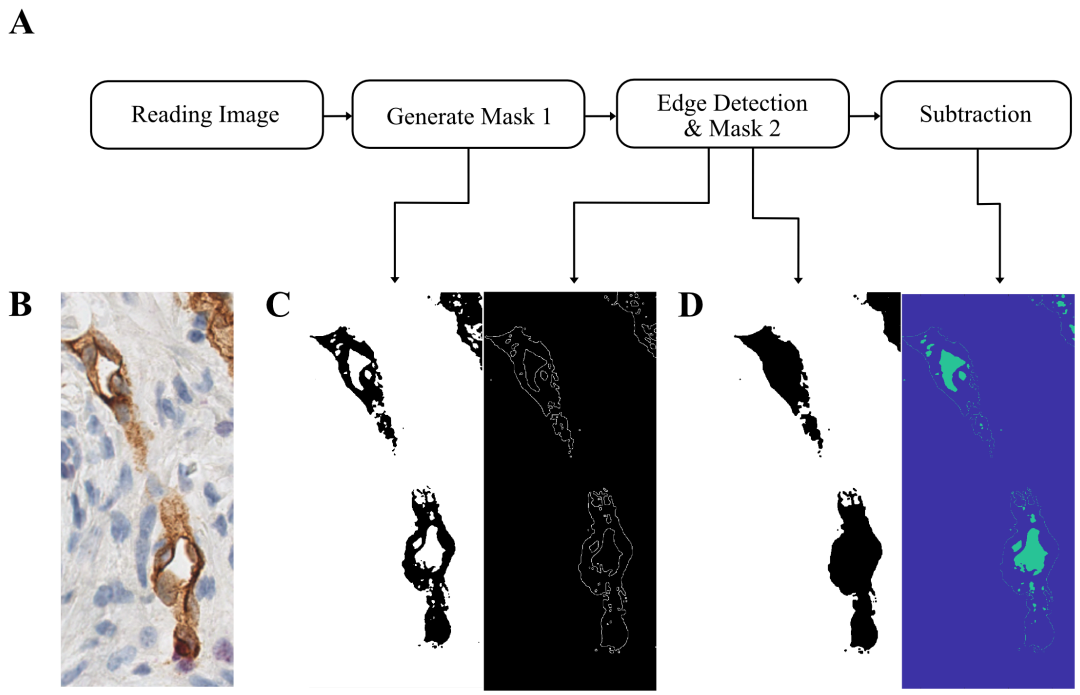

Fig.VII-6: Approximating vessel size in CD31-stained images ***(A)*** *Workflow* ***(B)*** *Exemplary images to respective workflow (context indicated by arrows)*

4.6 Analysis of Immunofluorescent (IF) zytology

4.6.1 Counting Cells

Automated counting of cells in culture requires adequate preprocessing, reliable automated thresholding and prudent interpretation of results. Regarding preprocessing, in this case a Gaussian filter is applied (sigma 0.2).

Widespread thresholding methods for standardized analysis include Otsu's method for thresholding. It works by minimizing interclass variance performing well separating cells and background. However, in the context of automatically counting cells, this method is prone to error caused by noise and the affiliated splitting of positive regions. In this script it is implemented using the built-in graythresh()-

function of MATLAB. As depicted in Fig.VII-7, Otsu's method of thresholding renders unsatisfactory precision (Mean difference to manual count of nuclei = 90 ± 90.8).

Therefore another novel second order thresholding method was developed and validated. Second order in this context means, that the thresholding method relies on the prospective number of positive regions counted and determines the threshold using that information. The method was created from observing counting results at different thresholds applied. Using thresholds that are too low, grants stains of noise the status of positive regions and therefore the count will be numerous. Higher thresholds will also overestimate the cell count present, as negative regions within the nuclei will split these positive regions. Therefore, the threshold retrieving the lowest number of positive regions excludes the possibility of noise being unwillingly counted and negative regions dividing nuclei. To achieve this, cell counts are determined for a preset number of thresholds (x) specified by an x-dimensional vector. Measurements are plotted for control and the first low point is determined using the function islocalmin(). This approach will be referred to as the Low-Point-Approach (LPA) further on. Merging regions remain a problem when only using LPA. That is why it was extended by a second thresholding technique: Using Canny's edge detection algorithm, a binarized image was generated using the threshold found using LPA. Then a periodically increasing number of pixels is subtracted from the margins of positive regions. Thereby groups of nuclei are separated while single nuclei are still counted. If plotted the clear point of inflection indicates the truest cell count. The performance of these cell counting techniques was compared using a dataset of 25 representative images. LPA delivers results nearest to manual count (relative Difference (D) to manual count = 0.05 ± 0.05) while LPA + the subtraction approach (ST) works better than single LPA if there are large areas of overlapping nuclei.

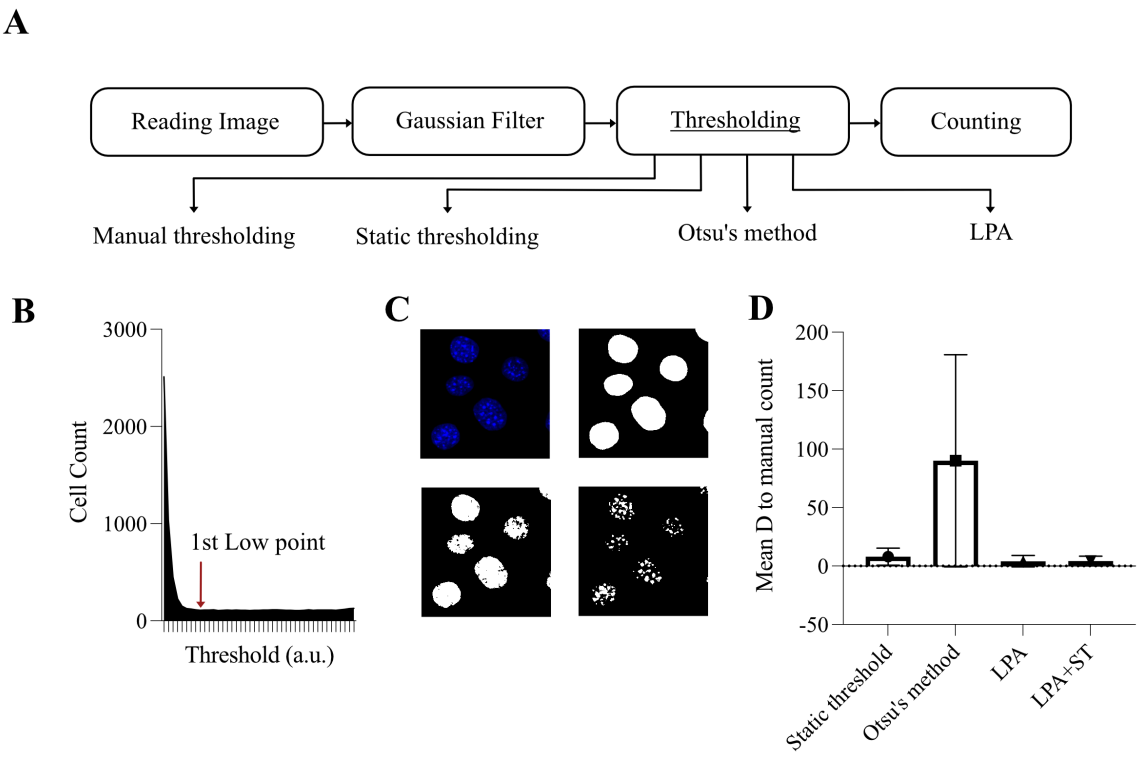

Fig.VII-7: Counting nuclei in DAPI-stained images ***(A)*** *Workflow* ***(B)*** *Exemplary illustration of LPA (arrow indicates automatically selected low point)* ***(C)*** *Illustration of different thresholds applied to a DAPI-stained nuclear image (upper left) – with increasing threshold (upper right → bottom left → bottom right)* ***(D)*** *Performance of different common automated thresholding methods*

4.6.2 Determining Signal Intensities and Positive Pixel Count

Signal intensities (I) were taken as the grey values that were assigned to a pixel in the respective RGB channel. The tool allows extraction of the cumulative sum of all pixel intensities present, as well as referenced values such as intensity per nucleus or intensity per DAPI signal.

Positive Pixel Count (PPC) is a parameter of present staining not being weighted by stain intensity. Therefore this parameter is robust to distortion by areas of particular high or low staining. This is biologically relevant as staining intensity is only to a limited extend proportional to antigen presence. PPC is implemented using a loop classifying pixels in positive or negative dependent of the threshold T. T can be assigned manually or using thresholding techniques described above.

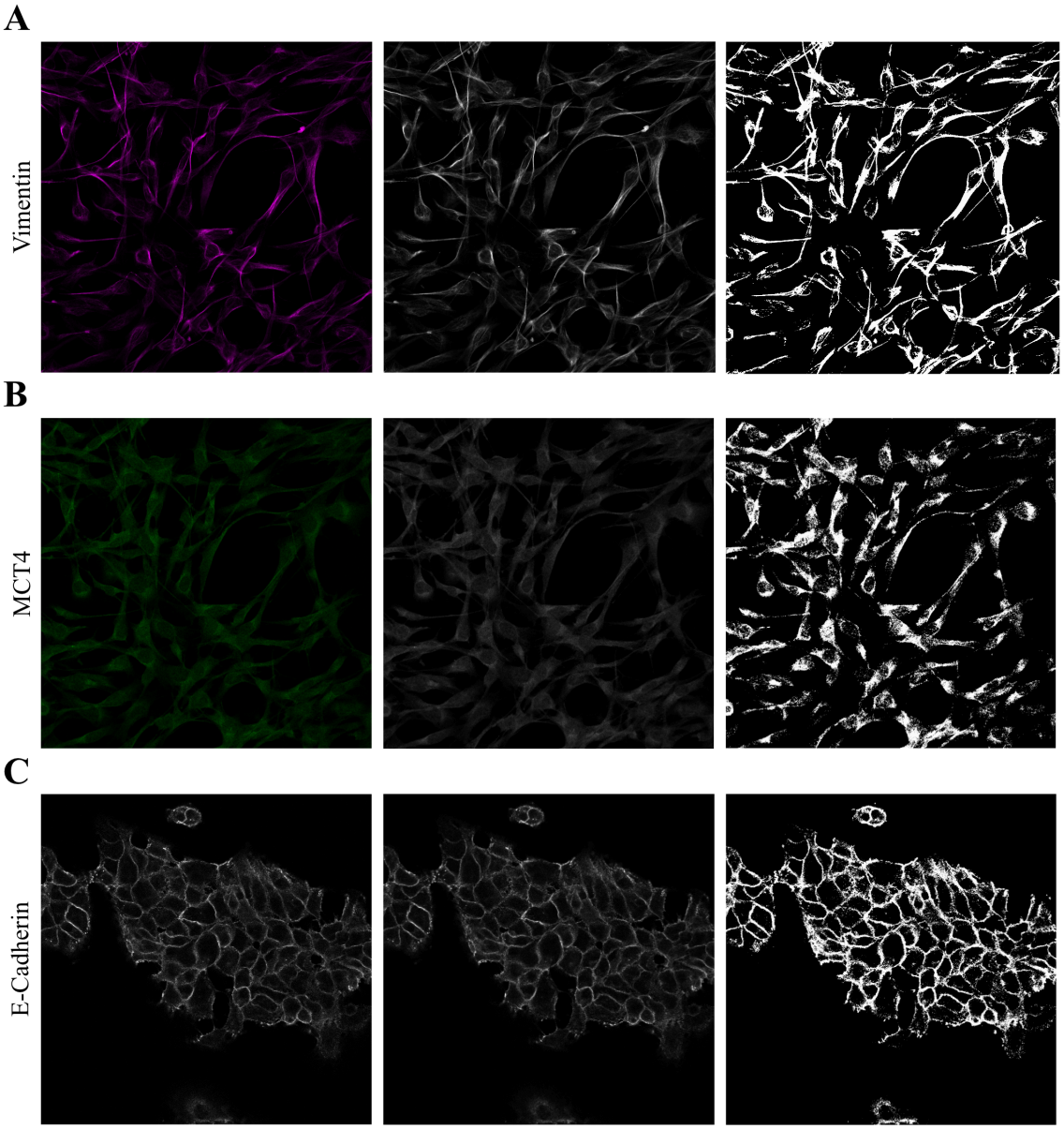

Fig.VII-8: Positive Pixel Count on immunofluorescent stained cytology ***(A)*** *From left to right: RGB-image of Vimentin signal, single channel image of Vimentin signal and automatically thresholded image of Vimentin signal used for PPC* ***(B)*** *From left to right: RGB-image of MCT4 signal, single channel image of MCT4 signal and automatically thresholded image of MCT4 signal used for PPC* ***(C)*** *From left to right: RGB-image of E-Cadherin signal, single channel image of E-Cadherin signal and automatically thresholded image of E-Cadherin signal used for PPC*

4.7 AVAILABILITY

The complete MATLAB code for the preprocessing tool may be received upon request (under mm.moritz.mayer@gmail.com).

5. ADDITIONS TO PART ONE

The following paragraphs devote themselves to depicting more detailed analysis of the endogenous tumors. This includes data on growth kinetics, perfusion of the tumors as well as data on the influence of technical and biological parameters on imaging results.

5.1 CHARACTERISTICS OF ENDOGENOUSLY GROWN MPDAC

Compared to orthotopic mPDAC, endogenously grown tumors from this GEMM displayed a high inter- and intratumoral heterogeneity. We observed the juxtaposition of ductal and epithelial to mesenchymal and undifferentiated growth within a single tumor region. Furthermore, the tumors revealed large regions of desmoplastic stroma similar to human PDAC. Depending on genotype different growth kinetics could be observed using anatomic T_2-weighted imaging: CKPlox mice developed a tumor with the minimal size of 5x5x5mm^3 around the sixtieth day, CKP+/- and CKP+/-T mice took significantly longer ($p < 0.001$) and developed their tumors around the hundredth day (see VII.5.1). A weak correlation was found in CKPlox mice between the time since birth and the number of tumorous lesions found ($r = 0.394$, see VII.5.1).

In anatomic T_2-weighted MRI not only neoplastic growth could be evaluated. Solid tumor growth was displayed hypointense in T_2w while preneoplastic lesions were displayed hyperintense. It was used to assess tumor growth, tumor morphology and thereby select suitable tumors for further imaging. All tumors identified by MRI were solid PDAC. Tumors were subdivided based on their tumor cellularity and morphology. Tumor cellularity was evaluated examining tumor cell clusters greater equal to 1mm^3 as established by Heid et al. (Heid, Steiger et al. 2017)Tumors with high tumor cellularity meaning over 40% of cells in a defined cluster were considered tumor cells were named PDAC^{high}. Equivalently, tumors in which tumor cellularity was below 40% were classified as PDAC^{low}.

The involved genotypes of GEMM CKPlox, CKP+/-, CKP+/-T all produced tumors with very high, medium and low tumor cellularity. Furthermore, all described phenotypes ranging from ductal or cribriform to sarcomatoid and undifferentiated were found without a perceptible connection to a certain genotype (Heid, Steiger et al. 2017). Mice of the genotype CKP+/-T produced preneoplastic

lesions with more cystic phenotype (IPMN). However, solid tumor growth led to histology comparable to mice of the genotype CKPlox and CKP+/-. As previously described (Heid, Münch et al. 2022) tumor progression was accompanied by a loss of ductal structures and an increase of tumor cellularity.

5.2 Assessment of tumor growth using T_2-weighted MRI

T_2-weighted MRI provides reliable information about tumor volume. It is also a safe tool to distinguish solid tumor growth from preneoplastic lesions. Solid tumor growth was displayed hypointense in T_2w while preneoplastic lesions were displayed hyperintense. It was used to assess tumor growth, tumor morphology and thereby select suitable tumors for further imaging.

In an effort to quantify the mere descriptive characteristics that were used to assess tumor growth, several parameters have been drawn from histogram analysis including mean, standard deviation (SD), relative standard deviation (%SD) and kurtosis. Preneoplastic lesions could be distinguished from solid tumor growth by SD with preneoplastic lesions presenting high SD because of high heterogeneity. Further quantitative differentiation of tumors based on histogram parameters was not possible. SD, relative SD and kurtosis merely showed minimal correlation with parameters for cellularity (ADC and histologic evaluation). Nevertheless, through good histological correlation, further texture analysis may prove valuable.

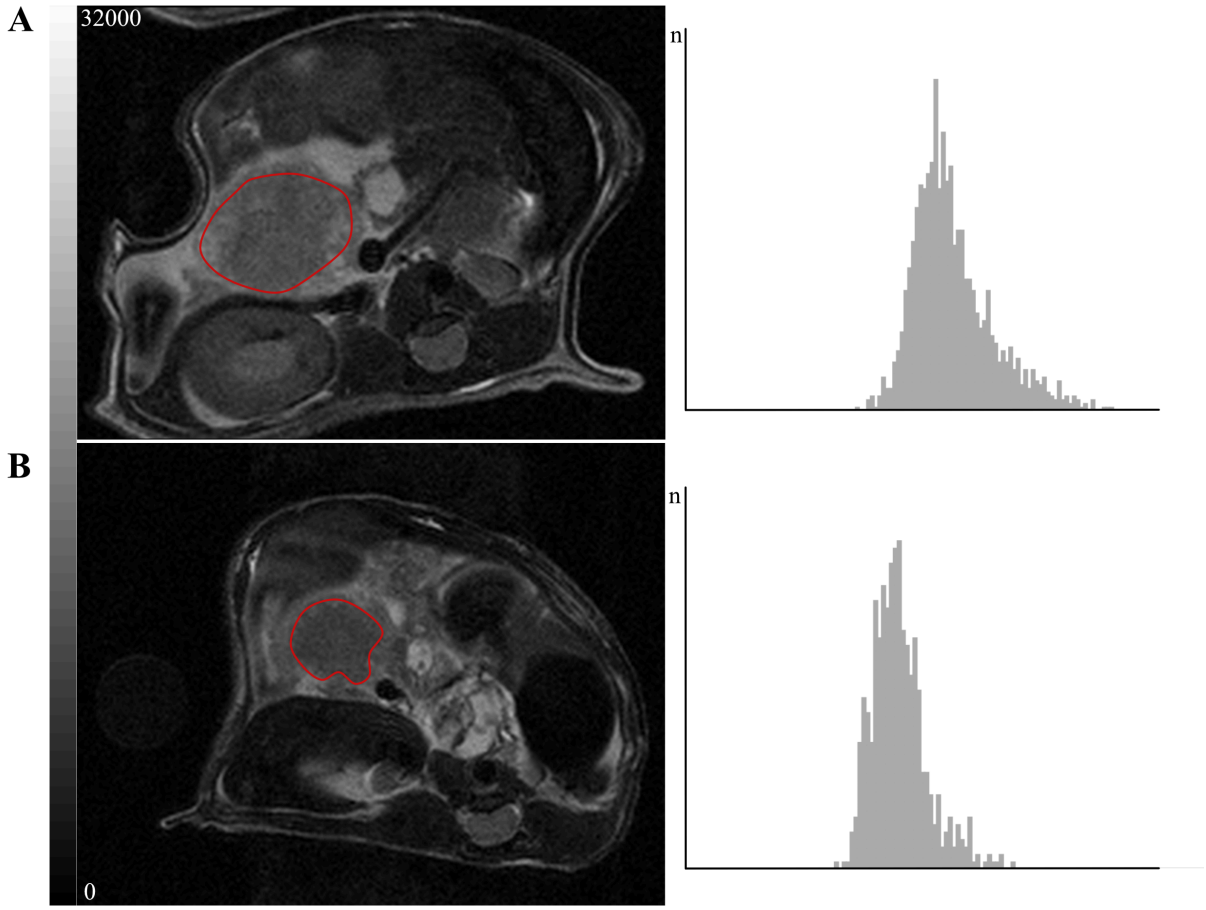

Fig.VII-9: Histogram analysis of tumors in T_2-weighted MRI ***(A,B)*** *T_2-weighted abdominal scan (left) and the corresponding histogram (right) of the tumor region (circled red)*

As expected the growth kinetics of CKPlox differed significantly from CKP+/- and CKP+/-T. A tumor of the size of at least 5x5x5mm^3 marked the start point of multimodal imaging. The age of the mice until they have developed such tumor is significantly lower in CKPlox than in CKP+/- and CKP+/-T (Fig. VII-10).

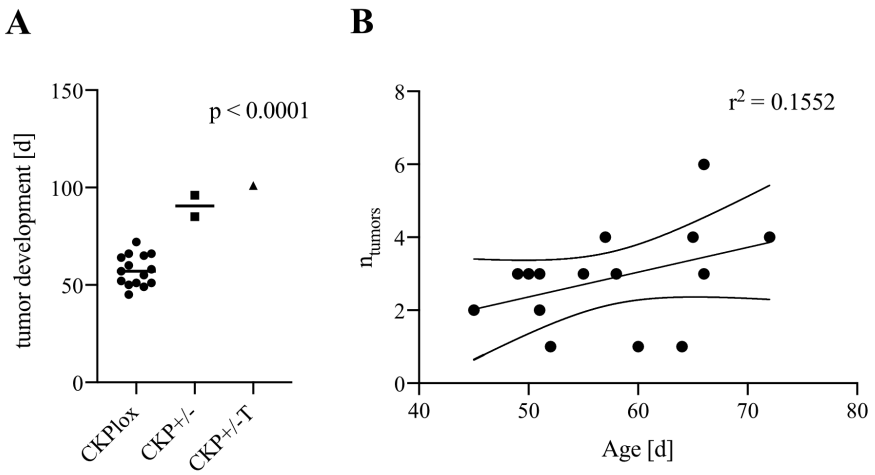

Fig. VII-10: Growth kinetics of mPDAC ***(A)*** *displays days until development of a 5x5x5mm³ tumor corresponding to each genotype* ***(B)*** *displays association of number of separate tumor lesions and age of the mice (CKPlox)*

5.3 STRUCTURAL AND METABOLIC STABILITY OF ENDOGENOUS MPDAC

The stability of tumors within 48 hours was evaluated using DWI, hyperpolarized 1-^{13}C-pyruvate MRSI and ^{18}F-FDG PET. As presented in chapter VII.2.2 the ADC value measures isotropic diffusion in tissue and is correlated to tumor cellularity. Therefore, it was evaluated as a longitudinal parameter to capture tissue composition in a protocol including 24, 48 and 72 hours as well as longer developments reaching up to 17 days (see Fig.VII-11). There was no relevant difference between the values of 0 and 48h (Mean Deviation = 1.3% ± 3,2%). Therefore, we consider the ADC constant within shorter time frames (see Fig.VII-11 A-C). During tumor progression a decrease in ADC – indicating an increase in cellularity – was observed in almost all tumors over a longer period of time (see Fig.VII-11 D-G). It was observed that at an ADC between 1100 and 1300 $\mu m^2/s*10^6$ tumors reached a steady state from which a further decrease of ADC was not observed. At this state, necrosis or edema in some tumors led to a slight increase in ADC values again. Instability of the ADC parameter due to errors or changes in the experimental setup has been obviated through breathing control and central position of the tumor.

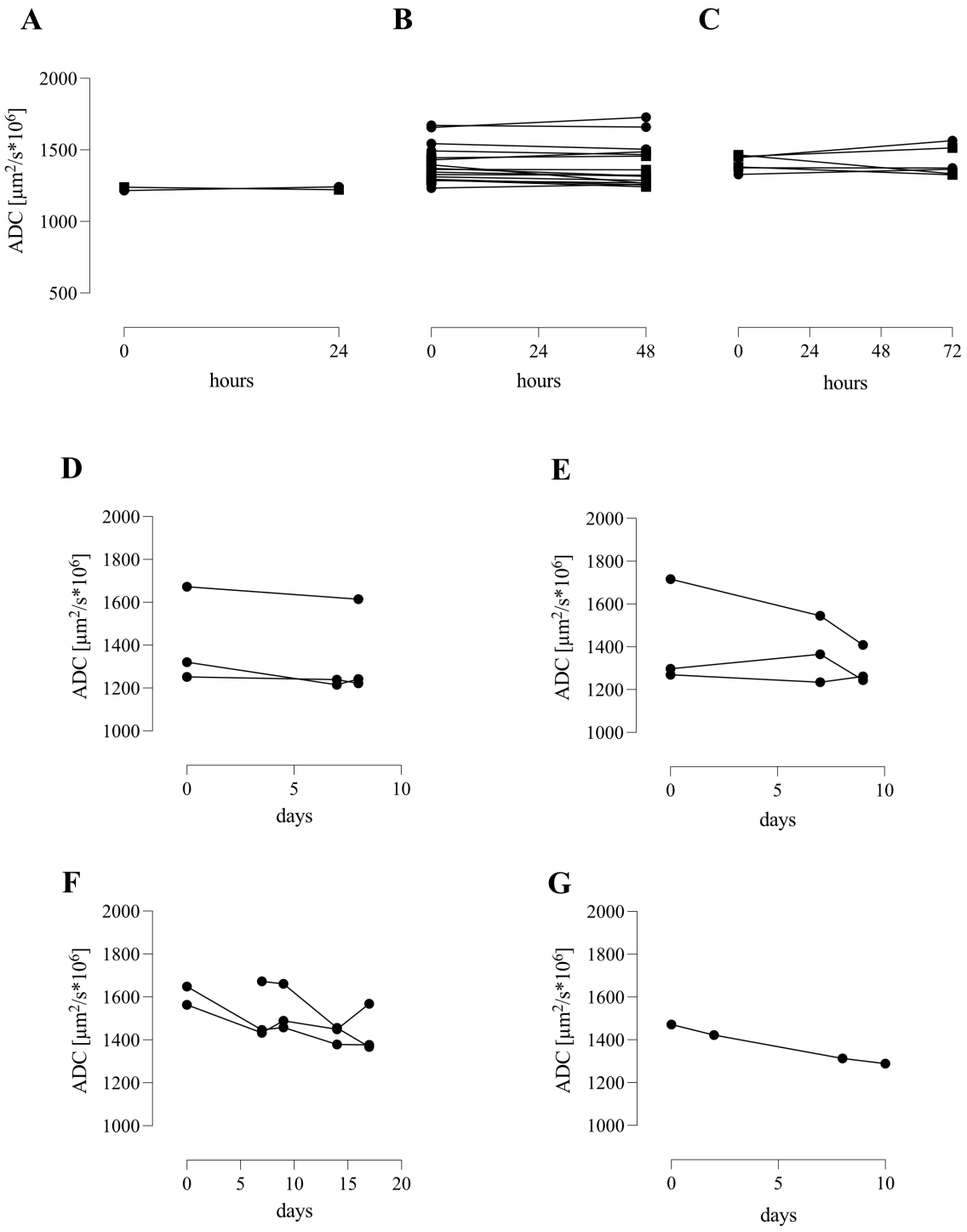

Fig.VII-11: Longitudinal DWI ***(A)*** *Longitudinal measurements of ADC in endogenous PDAC over 24 hours* ***(B)*** *Longitudinal measurements of ADC in endogenous PDAC over 48 hours ($n_{regions}$ = 17)* ***(C)*** *Longitudinal measurements of ADC in endogenous PDAC over 72 hours* ***(D)*** *Longitudinal measurements of ADC in a mouse with endogenous PDAC over 8 days* ***(E)*** *Longitudinal measurements of ADC in a mouse with endogenous PDAC over 9 days* ***(F)*** *Longitudinal measurements of ADC in a mouse with endogenous PDAC over 10 days* ***(G)*** *Longitudinal measurements of ADC in a mouse with endogenous PDAC over 17 days*

As there are a couple of transient factors influencing metabolism and its measurement, metabolic stability over a time period of 48 hours was evaluated in this study using both hyperpolarized 1-^{13}C-pyruvate MRSI and ^{18}F-FDG PET. Using hyperpolarized 1-^{13}C-pyruvate MRSI only minor changes in AUC_l/AUC_p values were observed in a 1 hour (one mouse 0h: AUC_l/AUC_p = 0.297; after 1h: AUC_l/AUC_p = 0.285) to 48 hour time frame (see Fig.VII-12 E). Two mice were measured with hyperpolarized 1-^{13}C-pyruvate MRSI spanning longer time frames. Within nine days one mouse was measured three times using 1-^{13}C-pyruvate MRSI and showed a constant AUC_l/AUC_p in the tumor measured (Day 0: AUC_l/AUC_p = 0.653; Day 7: AUC_l/AUC_p =0.753; Day 9: AUC_l/AUC_p = 0.755). This finding is supported by the other tumor that also showed no major shift in AUC_l/AUC_p (Day 0: AUC_l/AUC_p = 0.527; Day 7: AUC_l/AUC_p =0.509; Day 9: AUC_l/AUC_p = 0.569). As in this dataset the 1-^{13}C-pyruvate signal intensities are correlated stronger to the AUC_l/AUC_p than hyperpolarized 1-^{13}C-lactate signal intensities, it is noteworthy that the 1-^{13}C-pyruvate signal intensities have a stronger influence on the calculated AUC_l/AUC_p than the 1-^{13}C-lactate signals especially considering measurements were performed with a SNR between 5 and 15. In this model, we observed an association between tumor size (measured in anatomic T_2-weighted MRI) and AUC_l/AUC_p (r = 0.818, see VII.5.9, Fig.VII-17) in the evaluated tumors. This was not due to partial volume artifacts as no correlation between amount of voxels and AUC_l/AUC_p was seen (r = 0.045, see VII.5.5, Fig.VII-17). Nevertheless, the low resolution of a voxel in the metabolic imaging may limit detailed interpretation in this regard. That the tumors are metabolically stable after 48 hours is supported by the ^{18}F-FDG PET measurements where the values were constant over 48 and 72 hours (see Fig.VII-12 D). However, one mouse that received these measurements was excluded because of severe weight loss that met termination criteria and a proportional drop in SUV_{mean}.

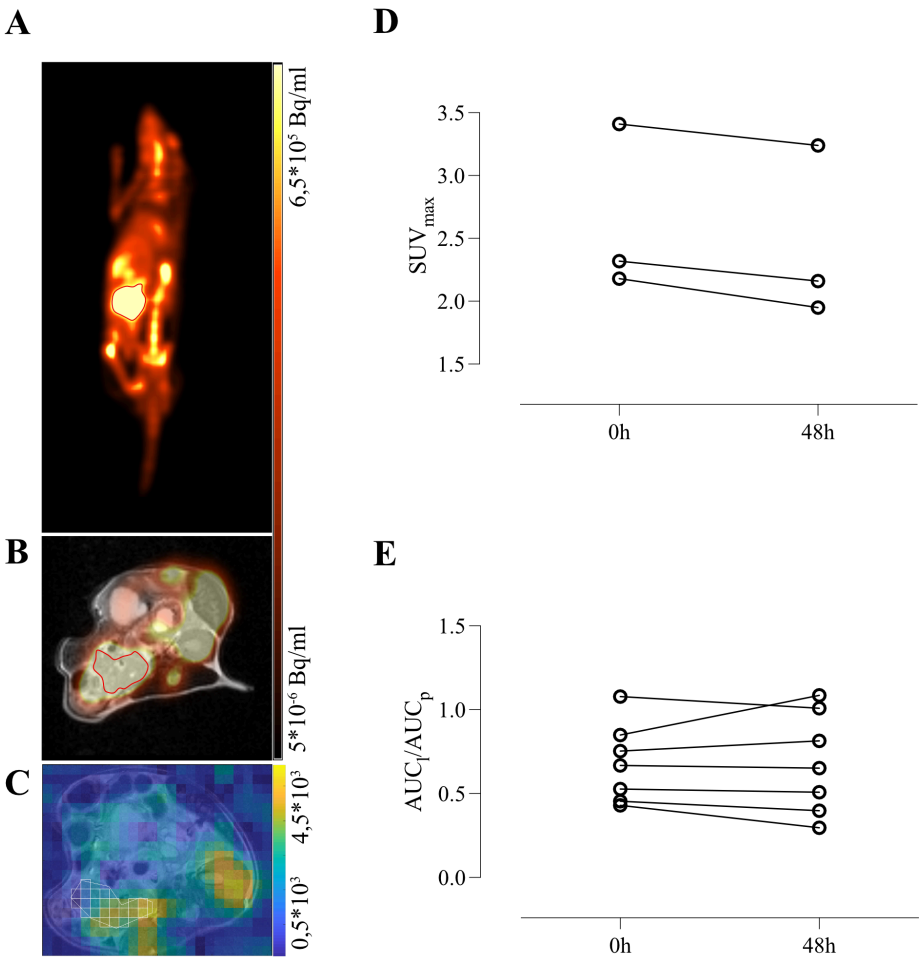

Fig.VII-12: Longitudinal metabolic imaging ***(A)*** *Exemplary coronar* ^{18}*F-FDG PET scan* ***(B)*** *Axial* ^{18}*F-FDG PET image over the corresponding* T_2*-weighted anatomic imaging* ***(C)*** *Hyperpolarized 1-*^{13}*C-pyruvate MRSI – lactate image* ***(D)*** *Longitudinal* SUV_{max} *values 48h* ***(E)*** *Longitudinal* AUC_l/AUC_p *values 48h*

5.4 ADC_{PERF} AND MICROVASCULAR PERFUSION

Microvascular perfusion plays a huge role in the tissues milieu. It can be assessed with low b-value ADC maps which are sensitive to capillary perfusion when compared to high b-value ADC maps which are mainly only sensitive to diffusion. Comparing those, the effects based on the capillary perfusion may be approximated. The values calculated for the ADC_{perf} and SPF have limited meaning for this study, but interesting implications for future experiments, which will be further discussed below.

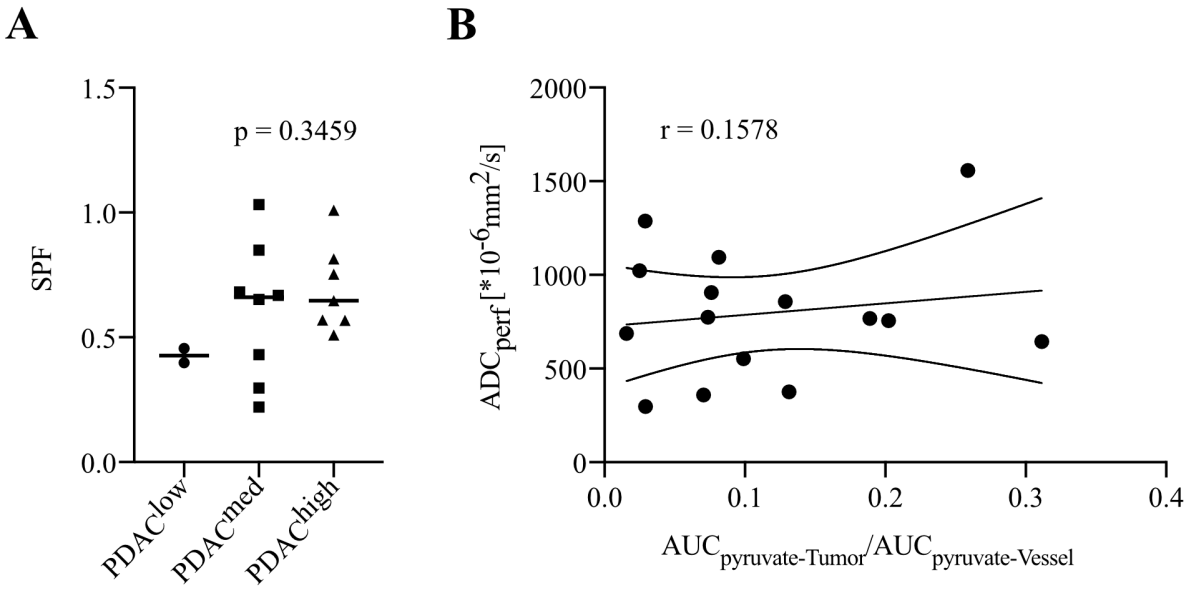

Fig.VII-13 – ADC_{perf} and SPF ***(A)*** *SPF of tumors plotted with subtypes indicative of tumor cellularity* ***(B)*** *Correlation of ADC_{perf} with an exemplary marker of perfusion ($AUC_{pyruvate}$ of the tumor divided by $AUC_{pyruvate}$ of the Vena cava inferior*

5.5 Point Spread function and partial volume artifacts

Point spread function and partial volume artefacts can have a great influence on the calculated AUC_l/AUC_p. The selection of ROIs was made considering such artefacts. It is to assume that high pyruvate signal intensities from the vessel lead to low AUC_l/AUC_p in tumors close to the vessel and that high lactate signal intensities in the kidney lead to higher AUC_l/AUC_p in tumors close to the kidneys.

There was no correlation found between distance from the tumor margin to a major vessel, from the tumor centre to a major vessel, from the tumor margin to the kidneys or from the tumor centre to the kidneys (Fig. VII-14). This indicates that the selection of ROIs considering those artefacts did not add a systematic error in the data evaluation.

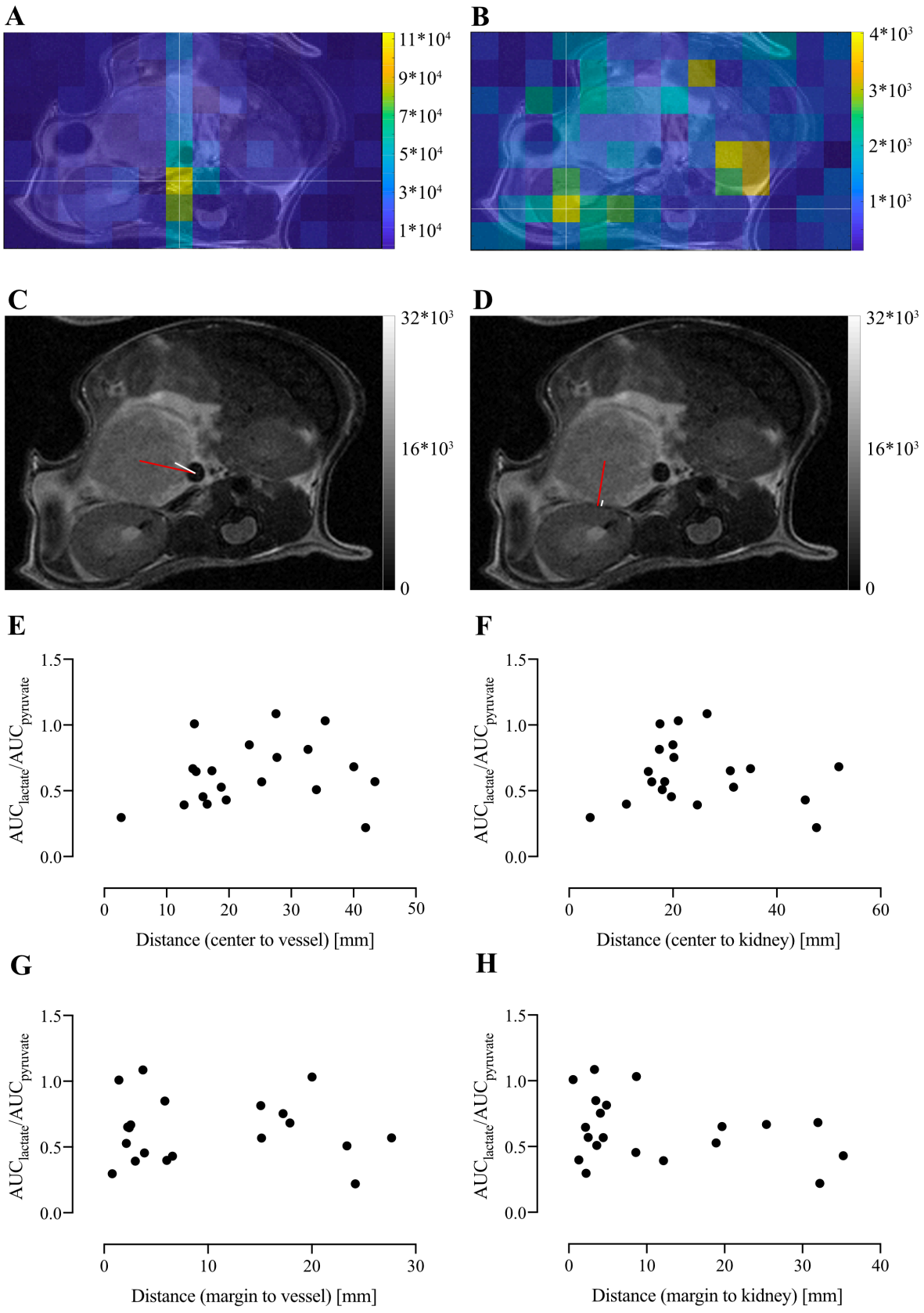

Fig. VII-14: Point spread function and partial volume artefacts ***(A)*** *1-^{13}C-pyruvate abdominal image displaying point spread function artefact from Vena cava inferior* ***(B)*** *1-^{13}C-lactate abdominal image displaying partial volume artefact from kidney* ***(C)*** *Measurement of distances (red = center to vessel;*

white = margin to vessel) ***(D)*** *Measurement of distances (red = center to kidney; white = margin to kidney)* ***(E-H)*** *Correlation of AUC_l/AUC_p with parameters expressing possible susceptibility to artefacts*

5.6 REFERENCE TISSUES

In order to translate metabolic measurements into the clinic, interinstitutional comparability of the read-out parameters is vital. One first simple approach to reach better comparability would be to introduce a reference tissue. This was thought to reduce the influence of variables from one scan to another.

A good reference tissue should bear information about the scan (e.g. signal intensity). Furthermore, it should be of constant perfusion and metabolism as it should serve as a reference and thereby should exhibit as little variation in its own metabolism as possible. Additionally, it would be ideal if the reference tissue was on the same height as the tumor because then it can be also be evaluated from a Single Slice CSI. That is beneficial as Multi-Slice CSIs are possible, but reduce either temporal or spatial resolution of the tumor slice. Three candidates that could fit to those descriptions were tested: Vessel (Vena cava inferior: signal intensity is directly linked to degree of polarisation, applied 1-^{13}C-Pyruvate and systemic conversion to lactate), kidney (shows constant perfusion and excretion, produces and takes up lactate in a constant manner) and muscle (shows low constant perfusion in rest). Exemplary, the vessel will be elucidated. Interindividually the AUC_l/AUC_p showed broad varying. This is to be expected as every mouse of course shows different systemic lactate production and therefore different intensities of lactate signal in the blood pool. Longitudinal vessel AUC_l/AUC_p however painted a different picture. Here the values are constant except for one measurement. This outlier was recognised as such and is not incorporated in the following reflections. This finding is supportive of the hypothesis that after 48h one can disregard major metabolic shifts without any kind of inflammation or other influencing variable and supports this study design retrospectively.

Next, it was to determine with which analysis protocol the values showed little variation over time. Analysis with a bandwidth of 15 Hz and double interpolation showed the smallest variation.

Afterwards, the AUC_l/AUC_p of the tumor was proportioned to the AUC_l/AUC_p of the vessel. There is a correlation of the combined ratios with tumor phenotype, however the combined ratios did not improve upon the longitudinal results.

To conclude, kidney, vessel and muscle did not show a better stratification of tumors and are not necessary/electable as good reference tissues in 1-^{13}C-pyruvate MRSI.

5.7 THE INFLUENCE OF NOISE ON THE AUC_L/AUC_P

As described above, there is a possible association of the AUC-ratios and the noise level of the measurement. The calculation method of the AUC_l/AUC_p is supported by the fact that there has been no association found between the average noise level, SNR and AUC_l/AUC_p.

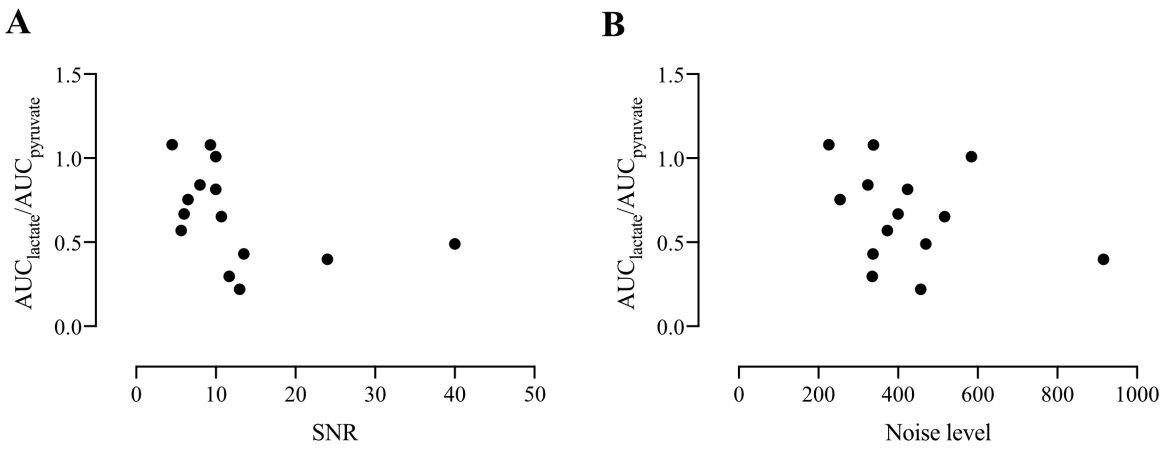

Fig.VII-15: Association of noise and AUC ***(A)*** *Association of SNR and AUC_l/AUC_p* ***(B)*** *Association of Noise level and AUC_l/AUC_p*

5.8 ANALYSIS OF SINGLE METABOLITE SIGNALS

The AUC_l/AUC_p as an approximation for k_{PL} is dependant on pyruvate and lactate signal intensities. A high AUC_l/AUC_p can be reached via a low pyruvate signal and/or a high lactate signal. Regarding chemical-shift imaging it is important to realize that there are certain limitations to that thought. As the pyruvate signal intensity is not only indicative of the tumors pyruvate uptake but also of tumor perfusion and is heavily influenced by partial volume of neighbouring vessels single metabolite analysis is necessary in order to reliably assess tumor biology.

There is a stronger correlation between pyruvate signal intensities and AUC_l/AUC_p than lactate signal intensities and AUC_l/AUC_p. This means generally the pyruvate signal intensities have more influence on the calculated AUC_l/AUC_p. Interestingly, more cellular tumors show lower pyruvate signal intensities indicating poor perfusion. The smaller amount of absorbed pyruvate then demonstrates why tumors cannot really be distinguished by lactate signal intensities. Concluding, the acquired pyruvate signal intensity gives more information about the tumors perfusion and cellularity while the

AUC_l/AUC_p casts light on enhanced metabolic pathways. Values need to be normalized by signals in the vessel, accounting for experimental deviations in measurement.

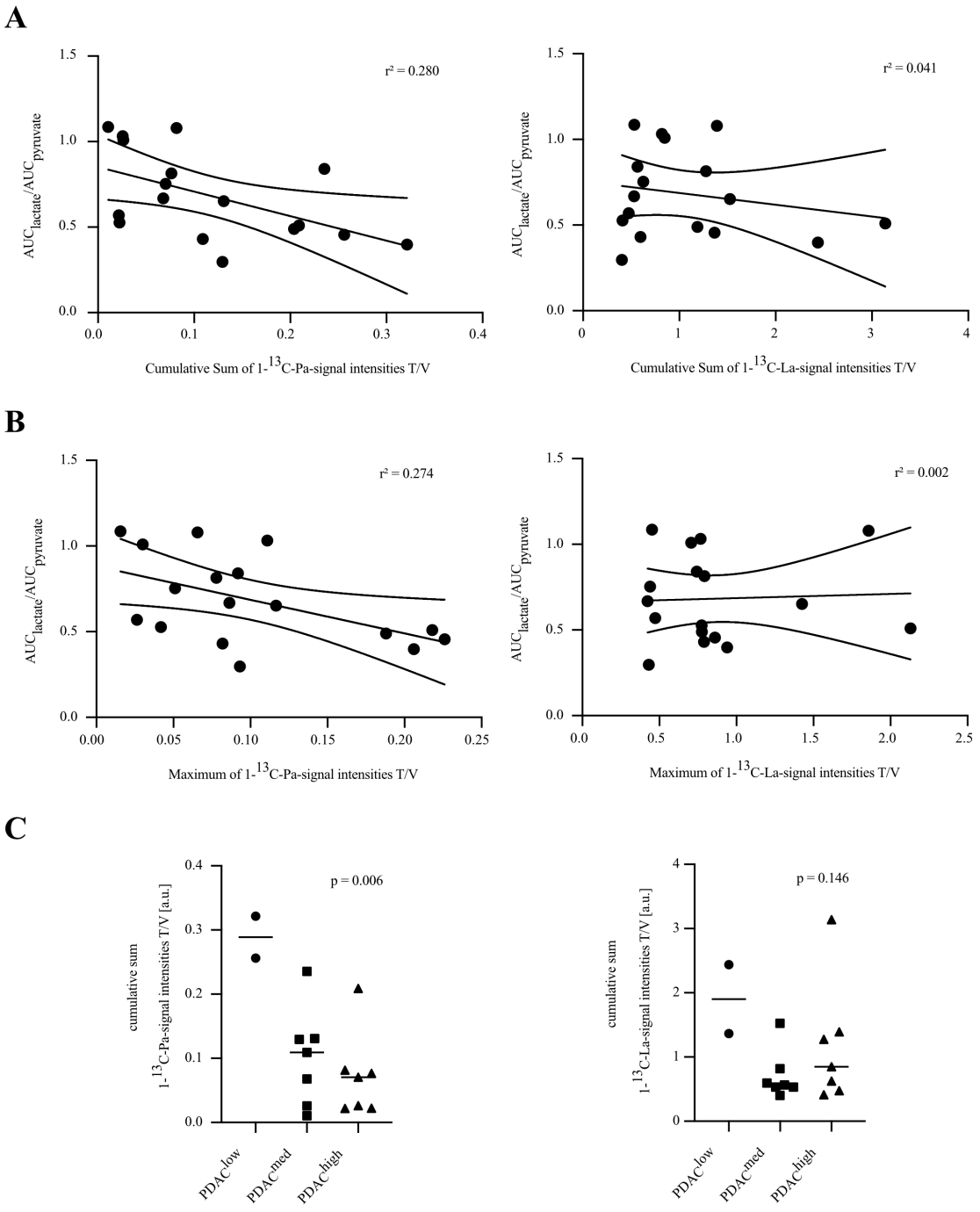

*Fig.VII-16: Single metabolite analysis **(A)** displays the influence of cumulative sum of 1-^{13}C-pyruvate (left) and 1-^{13}C-lactate (right) signal intensities on the overall AUC_l/AUC_p **(B)** correlates the maximum of the signal intensities with the AUC_l/AUC_p **(C)** arranges the single metabolite signals with tumor cellularity*

5.9 ASSOCIATION OF TUMOR SIZE, ROI VOXELS AND AUC

As shown in Fig.VII-17 there is a strong correlation between tumor size and AUC_l/AUC_p. In order to demonstrate that this is not just due to spatial volume artifacts and properties of the imaging modality used, it is displayed that there is no association between the voxels included in a ROI and the measured AUC_l/AUC_p.

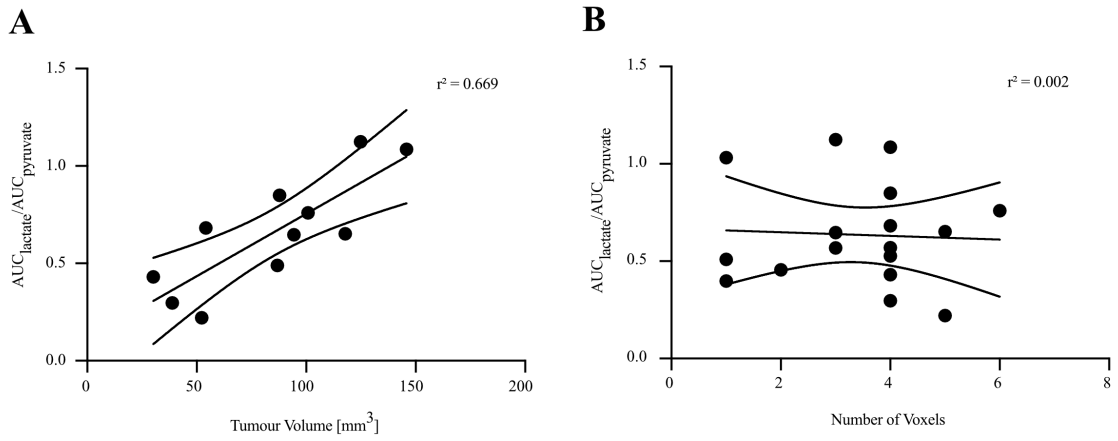

Fig.VII-17: – The influence of tumor volume on the measured AUC ***(A)*** *Correlation between tumor volume quantified by T_2-weighted MRI and AUC_l/AUC_p* ***(B)*** *Plot of Number of Voxels (2x2x2mm^3) in* 1-^{13}C-pyruvate MRSI *and AUC_l/AUC_p*

5.10 FLIP ANGLE

A flip angle (FA) of 5° was used in the 1-^{13}C-pyruvate MRSI sequence. This has been found to be a good trade off between initial signal intensity and saturation effects (see Fig. VII-18). Here, the same tumor was measured with a FA of 5° and 10°. Of course, the flip angle effects blend with cofounders such as differences in shimming, metabolic variability of the tumor and reactive perfusion differences. However, they underline the expected results and confirmed that a FA of 5° delivers acceptable results.

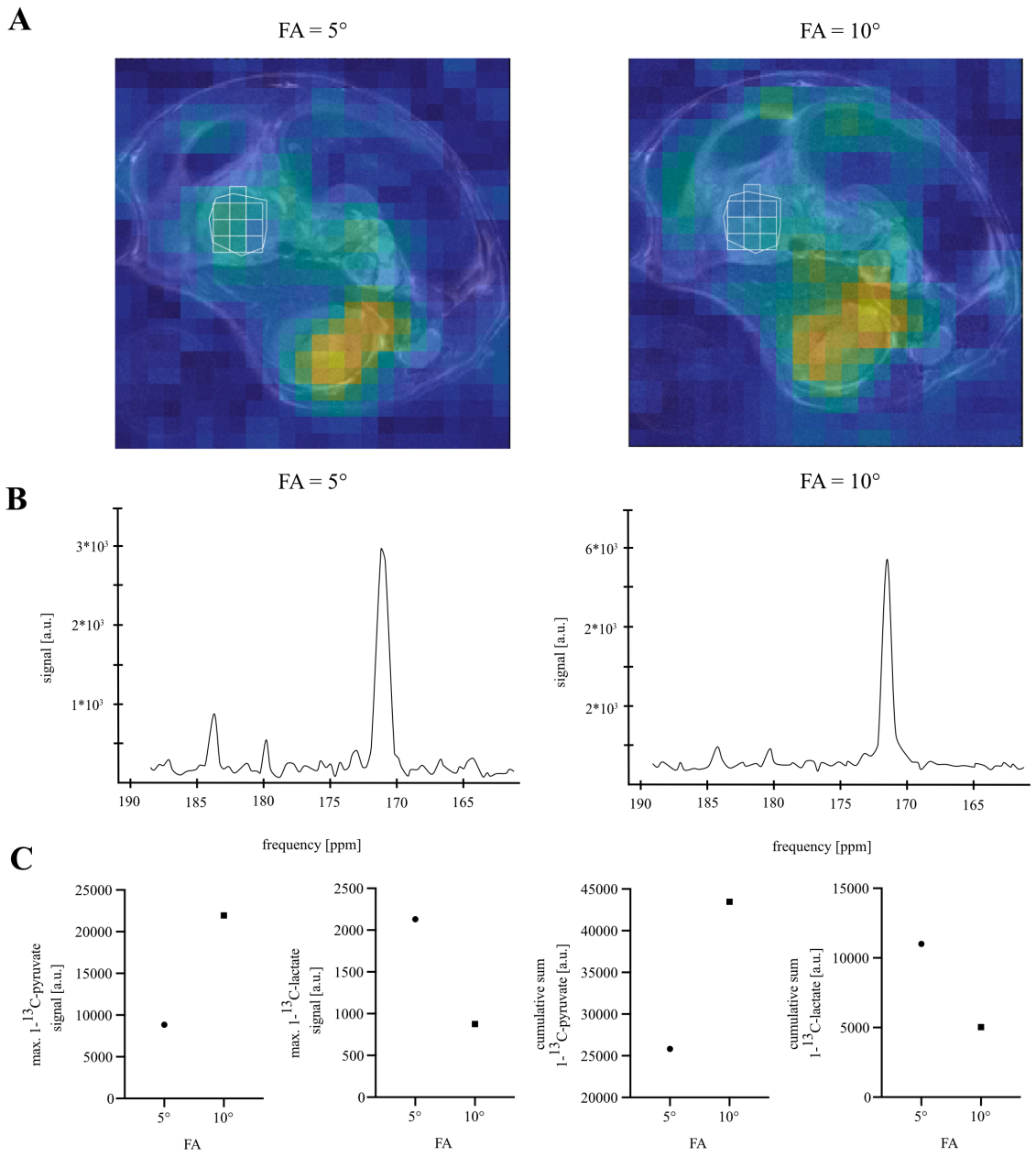

Fig.IX-18: Flip angle: ***(A)*** *1-^{13}C-lactate image of the same tumor measured with a FA of 5° (left) and 10° (right)* ***(B)*** *Respective spectra acquired with 5° FA (left) and 10° FA (right)* ***C)*** *Maximal measured signal intensities and cumulative sums with different FA*

5.11 THE INFLUENCE OF PHYSIOLOGICAL PARAMETERS

As the measurements are strongly dependent on physiological processes such as metabolism and perfusion, knowledge about the influence of physiologic characteristic of the mice is important.

5.11.1 Weight

The mice showed normal growth kinetics. There were no mice with visible cachexia. Mice losing weight were examined daily and the experiment was ended with weight loss >10%. Mice with significant weight loss were not included in the main study. In the results of PET it has been shown that significant weight loss, has a direct influence on tumor metabolism and therefore can lead to inaccuracies of measurements.

5.11.2 Blood glucose

As the applied metabolic imaging modalities PET and 1-^{13}C-pyruvate MRSI are involved in parts of glucose metabolism, measurements of the blood glucose levels were part of the standard protocol. Glucose measurements were performed before and after every scan. Comparing blood glucose levels before the scans of two subsequent scans 48h apart, it becomes apparent that the blood glucose level drops in most mice. This significant drop mainly affects mice with high-graded tumors disclosing their metabolic dysregulation and impaired adaptability. After 72h the blood glucose levels seem recovered as all mice had stable blood glucose levels.

This supports a therapy study design with intervals of 48h or 72h.

There is a relation between weight and blood glucose levels. Mice harbouring highly cellular tumors ($PDAC^{high}$) have significantly lower blood glucose levels ($p = 0.0447$). In part, tumors with high AUC_l/AUC_p showed lower blood glucose levels.

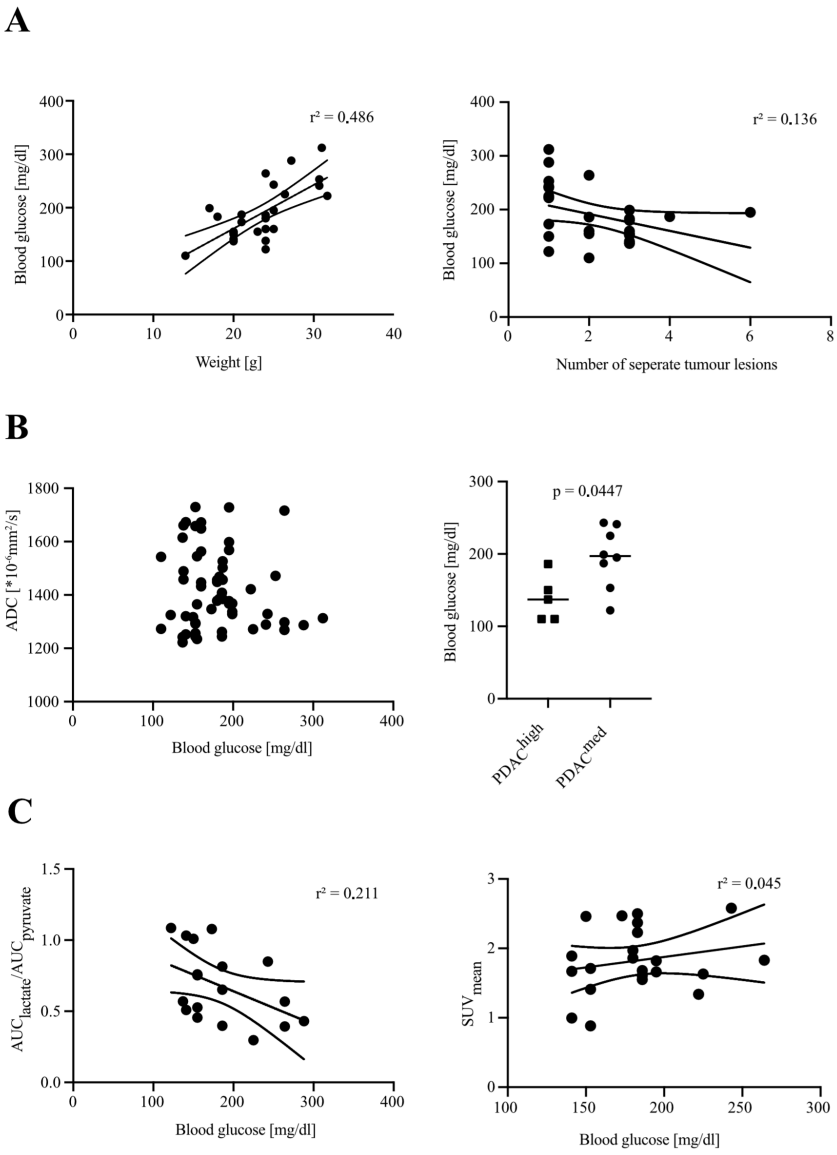

Fig.VII-19: Physiological parameters ***(A)*** *Correlation of Blood glucose levels and weight and association of number of separate tumor lesions and blood glucose* ***(B)*** *Blood glucose levels plotted with markers of cellularity of the tumor with the highest cellularity in the mouse* ***(C)*** *Blood glucose and its correlation with markers of glycolytic metabolism*

5.12 SUMMARY

The following figure summarized the proposed view of AUC_l/AUC_p as a multidimensional parameter.

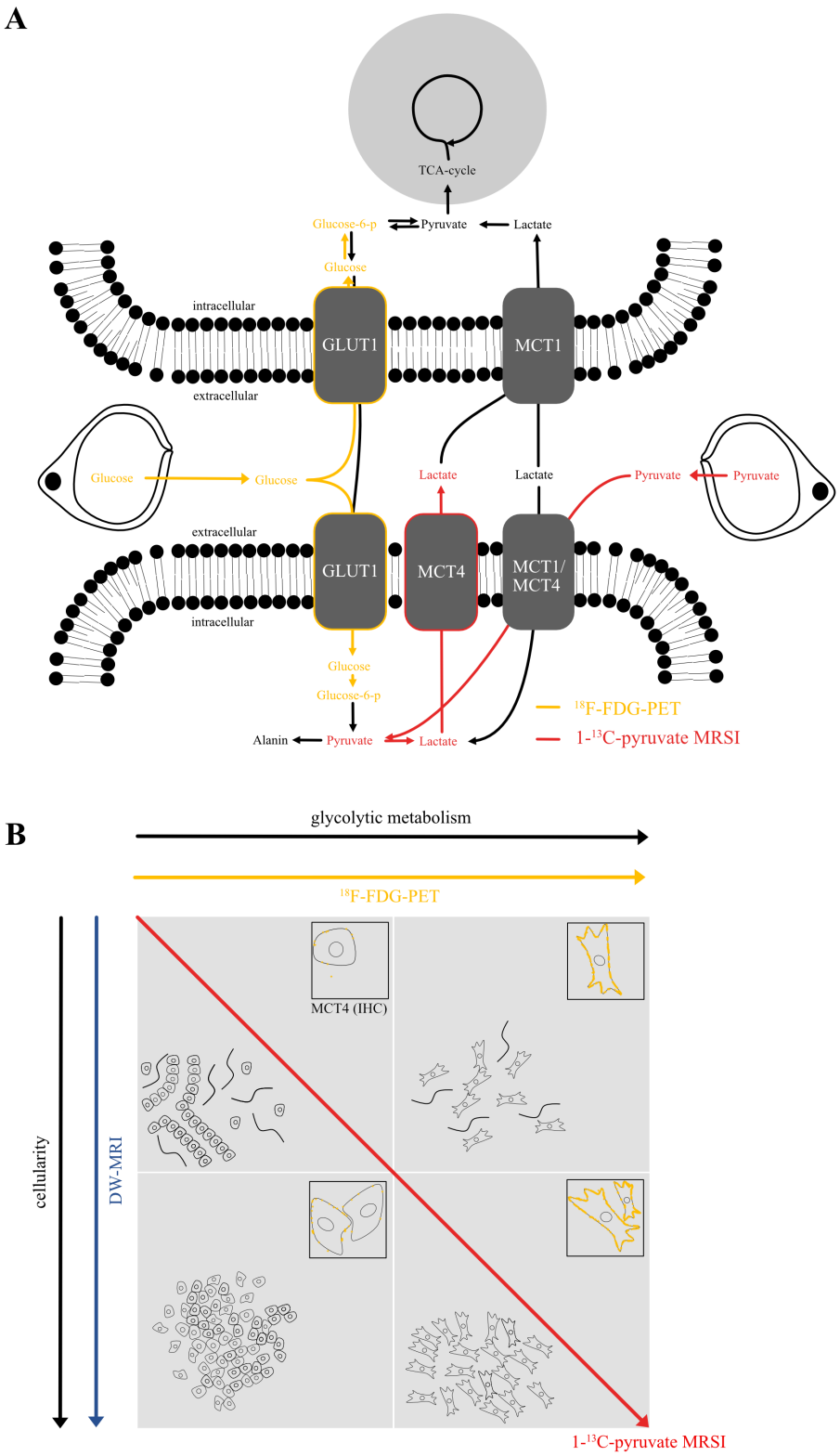

Fig.VII-20: Proposed characterization of AUC_l/AUC_p as a multidimensional parameter ***(A)*** *Shematic flow chart of metabolites and relevant substrate channels (lower cell = tumor cell, upper cell = activated stromal cell)* ***(B)*** *Illustration of multidimensionality of the AUC_l/AUC_p with it being influenced by cellularity and cellular metabolism combined*

5.13 COMPARISON OF 2-PARAMETER MODEL AND 3-PARAMETER MODEL IN DWI

36 Ptf1a$^{wt/cre}$;Kras$^{wt/G12D}$;p53$^{fl/fl}$ mice with 69 PDAC tumor regions were subjected to DWI at small animal 7 T MRI system (Agilent/GE magnet with Bruker AVANCE III HD electronics, with a 31 mm ID volume coil from RAPID Biomedical). DWI was conducted as free breathing using single-shot EPI-readout with 12 b-values (12-1528 s/mm^2), TE 34 ms, TR 5000 ms, voxel size 0.25x0.25x1 mm^3, 10 repetitions, scan time 10 min. DW magnitude image series with subsets of 12 (12-1528 s/mm^2) or 9 (12-722 s/mm^2) b-values were fit for the apparent diffusion coefficient (ADC) in MATLAB. Separately at each pixel, 10 repetitions were fit as a single data-set with least-squares nonlinear models, parameterized by the ADC, signal at 0 b-value (S0), and optionally a constant offset (C): Two parameter (2P): $S(b) = S_0 \cdot e^{-ADC \cdot b}$; three parameter (3P): $S(b) = S_0 \cdot e^{-ADC \cdot b} + C$. Tissue was formalin-fixed, H&E stained, and co-registered to ADC maps.

Murine endogenous PDAC was reliably visualized with the established high resolution DWI sequence at 7 T. Data, fitted with 2P equation, were equal to that achieved at 1.5 T and revealed the same overall distribution of values between subgroups. There was no significant separation between PDAC^{med} and PDAC^{high} using this method. Inclusion of DWI with b-values above 800 s/mm^2 and use of 3P fit, caused minor reduction of the qualitative image appearance but increased regional variance of ADC values leading to significant separation between groups by cellularity grade. Tumor cellularity subgroups had statistically significantly different mean ADC values (10^{-3}mm^2/s): PDAC^{low} = 1.56±0.1; PDAC^{med} = 1.34±0.1; PDAC^{high} = 1.26±0.1; ($p<0.0001$).

Mean ADC value reliably distinguishes previously proposed and clinically relevant subgroups of different cellularity. Inclusion of high b-values (>800 s/mm^2) and use of 3P model is necessary for reliable fitting of ADC maps. This observation may warrant further investigation in clinical scanners.

5.14 T_2*-MEASUREMENTS

T_2 is the time constant describing the loss of phase coherence of spins precessing in the transverse plain. Therefore, it is referred to as transverse relaxation. The properties of transverse relaxation are influenced by many factors: The two main factors are fluctuating changes of the local magnetic field experienced by single protons due to other adjacent nuclei and inhomogeneity of B_0. That is why the measurable signal decays faster than the actual T_2. The measurable apparent T_2 is called T_2*. Important pathological tissue properties posses the power to heavily influence the apparent T_2. Macromolecules including collagen, proteoglycans and so forth influence nearby protons, shortening their T_2. Also areas of reduced perfusion show shortening of apparent T_2 as in contrast to oxygenated

proteins, deoxygenated haemoglobin and myoglobin are paramagnetic perturbing the local fields experienced by single protons and thereby accelerating their dephasation.

To conclude, while measuring apparent T_2 tumorous tissue could stand out by unphysiological low T_2*.

Orthotopically implanted mice with mesenchymal (m.) and epithelial (e.) tumors (in total: 6 mice; 11 Tumor regions) were imaged and analysed. Single Slice Axial T_2 FSE was acquired with 8 different TE (6; 18; 30; 42; 54; 66; 78; 90 [ms]) and 6 Repetitions. R2 was fitted and analysed with MATLAB. R2 was validated with ^{13}C-urea phantom. In orthotopically implanted murine PDAC, tumorous tissue indeed displayed shorter T_2* than healthy adjacent tissue. The read-out parameter $R_2(^1H_2O)$ could be correlated with the apparent diffusion coefficient (r = 0.695). T_2* has been found to be directly proportional to ADC .

It can be concluded, that measurements of apparent T_2 can yield valuable insights into tissues' microstructure.

6. LITERATURE

Aggarwal, R., et al. (2017). "Hyperpolarized 1-[(13)C]-Pyruvate Magnetic Resonance Imaging Detects an Early Metabolic Response to Androgen Ablation Therapy in Prostate Cancer." Eur Urol **72**(6): 1028-1029.

Ardenkjaer-Larsen, J. H., et al. (2003). "Increase in signal-to-noise ratio of > 10,000 times in liquid-state NMR." Proc Natl Acad Sci U S A **100**(18): 10158-10163.

Baek, G., et al. (2014). "MCT4 defines a glycolytic subtype of pancreatic cancer with poor prognosis and unique metabolic dependencies." Cell Rep **9**(6): 2233-2249.

Bailey, P., et al. (2016). "Genomic analyses identify molecular subtypes of pancreatic cancer." Nature **531**(7592): 47-52.

Ben-David, U., et al. (2017). "Patient-derived xenografts undergo mouse-specific tumor evolution." Nat Genet **49**(11): 1567-1575.

Cao, M., et al. (2017). "Application of a Simplified Method for Estimating Perfusion Derived from Diffusion-Weighted MR Imaging in Glioma Grading." Front Aging Neurosci **9**: 432.

Chang, X., et al. (2022). "Glycolysis in the progression of pancreatic cancer." Am J Cancer Res **12**(2): 861-872.

Chen, H. Y., et al. (2020). "Hyperpolarized (13)C-pyruvate MRI detects real-time metabolic flux in prostate cancer metastases to bone and liver: a clinical feasibility study." Prostate Cancer Prostatic Dis **23**(2): 269-276.

Cheng, C. C., et al. (2013). "An automatic segmentation and classification framework for anti-nuclear antibody images." Biomed Eng Online **12 Suppl 1**(Suppl 1): S5.

Choi, S. Y., et al. (2016). "The MCT4 Gene: A Novel, Potential Target for Therapy of Advanced Prostate Cancer." Clin Cancer Res **22**(11): 2721-2733.

Collisson, E. A., et al. (2019). "Molecular subtypes of pancreatic cancer." Nat Rev Gastroenterol Hepatol **16**(4): 207-220.

Collisson, E. A., et al. (2011). "Subtypes of pancreatic ductal adenocarcinoma and their differing responses to therapy." Nat Med **17**(4): 500-503.

Costello, E., et al. (2012). "New biomarkers and targets in pancreatic cancer and their application to treatment." Nat Rev Gastroenterol Hepatol **9**(8): 435-444.

Daemen, A., et al. (2015). "Metabolite profiling stratifies pancreatic ductal adenocarcinomas into subtypes with distinct sensitivities to metabolic inhibitors." Proc Natl Acad Sci U S A **112**(32): E4410-4417.

Donehower, L. A., et al. (1992). "Mice deficient for p53 are developmentally normal but susceptible to spontaneous tumours." Nature **356**(6366): 215-221.

Dutta, P., et al. (2020). "Early Detection of Pancreatic Intraepithelial Neoplasias (PanINs) in Transgenic Mouse Model by Hyperpolarized (13)C Metabolic Magnetic Resonance Spectroscopy." Int J Mol Sci **21**(10).

Erstad, D. J., et al. (2018). "Orthotopic and heterotopic murine models of pancreatic cancer and their different responses to FOLFIRINOX chemotherapy." Dis Model Mech **11**(7).

Evan, G. I., et al. (2017). "Re-engineering the Pancreas Tumor Microenvironment: A "Regenerative Program" Hacked." Clin Cancer Res **23**(7): 1647-1655.

Feig, C., et al. (2012). "The pancreas cancer microenvironment." Clin Cancer Res **18**(16): 4266-4276.

Gallagher, F. A., et al. (2020). "Imaging breast cancer using hyperpolarized carbon-13 MRI." Proc Natl Acad Sci U S A **117**(4): 2092-2098.

Gnoni, A., et al. (2013). "Carcinogenesis of pancreatic adenocarcinoma: precursor lesions." Int J Mol Sci **14**(10): 19731-19762.

Goral, V. (2015). "Pancreatic Cancer: Pathogenesis and Diagnosis." Asian Pac J Cancer Prev **16**(14): 5619-5624.

Gupta, S., et al. (2010). "Nuclear morphometry and texture analysis of B-cell non-Hodgkin lymphoma: utility in subclassification on cytosmears." Diagn Cytopathol **38**(2): 94-103.

Gutte, H., et al. (2015). "Simultaneous hyperpolarized (13)C-pyruvate MRI and (18)F-FDG-PET in cancer (hyperPET): feasibility of a new imaging concept using a clinical PET/MRI scanner." Am J Nucl Med Mol Imaging **5**(1): 38-45.

Halestrap, A. P. and M. C. Wilson (2012). "The monocarboxylate transporter family--role and regulation." IUBMB Life **64**(2): 109-119.

Handra-Luca, A., et al. (2014). "EGFR expression in pancreatic adenocarcinoma. Relationship to tumour morphology and cell adhesion proteins." J Clin Pathol **67**(4): 295-300.

Harris, R. K., et al. (2002). "NMR Nomenclature: Nuclear Spin Properties and Conventions for Chemical Shifts. IUPAC Recommendations 2001." Solid State Nucl Magn Reson **22**(4): 458-483.

Heid, I., et al. (2022). "Functional noninvasive detection of glycolytic pancreatic ductal adenocarcinoma." Cancer Metab **10**(1): 24.

Heid, I., et al. (2017). "Co-clinical Assessment of Tumor Cellularity in Pancreatic Cancer." Clin Cancer Res **23**(6): 1461-1470.

Higashi, T., et al. (1998). "FDG uptake, GLUT-1 glucose transporter and cellularity in human pancreatic tumors." J Nucl Med **39**(10): 1727-1735.

Hill, D. K., et al. (2013). "Model free approach to kinetic analysis of real-time hyperpolarized 13C magnetic resonance spectroscopy data." PLoS One **8**(9): e71996.

Hingorani, S. R., et al. (2003). "Preinvasive and invasive ductal pancreatic cancer and its early detection in the mouse." Cancer Cell **4**(6): 437-450.

Hundshammer, C., et al. (2018). "Simultaneous characterization of tumor cellularity and the Warburg effect with PET, MRI and hyperpolarized (13)C-MRSI." Theranostics **8**(17): 4765-4780.

Hyun, S. H., et al. (2016). "Intratumoral heterogeneity of (18)F-FDG uptake predicts survival in patients with pancreatic ductal adenocarcinoma." Eur J Nucl Med Mol Imaging **43**(8): 1461-1468.

Ilic, M. and I. Ilic (2016). "Epidemiology of pancreatic cancer." World J Gastroenterol **22**(44): 9694-9705.

Jackson, E. L., et al. (2001). "Analysis of lung tumor initiation and progression using conditional expression of oncogenic K-ras." Genes Dev **15**(24): 3243-3248.

Jeon, S. K., et al. (2021). "Diffusion-weighted MR imaging in pancreatic ductal adenocarcinoma: prediction of next-generation sequencing-based tumor cellularity and prognosis after surgical resection." Abdom Radiol (NY) **46**(10): 4787-4799.

Johnson, S. J. and F. R. Walker (2015). "Strategies to improve quantitative assessment of immunohistochemical and immunofluorescent labelling." Sci Rep **5**: 10607.

Jørgensen, T., et al. (1996). "Nuclear texture analysis: a new prognostic tool in metastatic prostate cancer." Cytometry **24**(3): 277-283.

Kanda, M., et al. (2012). "Presence of somatic mutations in most early-stage pancreatic intraepithelial neoplasia." Gastroenterology **142**(4): 730-733.e739.

Kapuscinski, J. (1995). "DAPI: a DNA-specific fluorescent probe." Biotech Histochem **70**(5): 220-233.

Kong, S. C., et al. (2016). "Monocarboxylate Transporters MCT1 and MCT4 Regulate Migration and Invasion of Pancreatic Ductal Adenocarcinoma Cells." Pancreas **45**(7): 1036-1047.

Konstandinou, C., et al. (2018). "Multifeature Quantification of Nuclear Properties from Images of H&E-Stained Biopsy Material for Investigating Changes in Nuclear Structure with Advancing CIN Grade." J Healthc Eng **2018**: 6358189.

Langkilde, F., et al. (2018). "Evaluation of fitting models for prostate tissue characterization using extended-range b-factor diffusion-weighted imaging." Magn Reson Med **79**(4): 2346-2358.

Lee, S. H., et al. (2021). "MCT4 as a potential therapeutic target to augment gemcitabine chemosensitivity in resected pancreatic cancer." Cell Oncol (Dordr) **44**(6): 1363-1371.

Lehuédé, C., et al. (2016). "Metabolic Plasticity as a Determinant of Tumor Growth and Metastasis." Cancer Res **76**(18): 5201-5208.

Lunt, S. Y. and M. G. V. Heiden (2011). "Aerobic Glycolysis: Meeting the Metabolic Requirements of Cell Proliferation." Annual Review of Cell and Developmental Biology **27**(1): 441-464.

Mayer, P., et al. (2021). "Epithelial-to-Mesenchymal Transition in Pancreatic Cancer is associated with Restricted Water Diffusion in Diffusion-Weighted Magnetic Resonance Imaging." J Cancer **12**(24): 7488-7497.

Michel, K. A., et al. (2019). "Hyperpolarized Pyruvate MR Spectroscopy Depicts Glycolytic Inhibition in a Mouse Model of Glioma." Radiology **293**(1): 168-173.

Moffitt, R. A., et al. (2015). "Virtual microdissection identifies distinct tumor- and stroma-specific subtypes of pancreatic ductal adenocarcinoma." Nat Genet **47**(10): 1168-1178.

Muckenhuber, A., et al. (2018). "Pancreatic Ductal Adenocarcinoma Subtyping Using the Biomarkers Hepatocyte Nuclear Factor-1A and Cytokeratin-81 Correlates with Outcome and Treatment Response." Clin Cancer Res **24**(2): 351-359.

Mueller, S., et al. (2018). "Evolutionary routes and KRAS dosage define pancreatic cancer phenotypes." Nature **554**(7690): 62-68.

Mulkern, R. V., et al. (2006). "Biexponential characterization of prostate tissue water diffusion decay curves over an extended b-factor range." Magn Reson Imaging **24**(5): 563-568.

Murakami, K. (2011). "FDG-PET for hepatobiliary and pancreatic cancer: Advances and current limitations." World J Clin Oncol **2**(5): 229-236.

Nakamura, T., et al. (2007). "Gene expression profile of metastatic human pancreatic cancer cells depends on the organ microenvironment." Cancer Res **67**(1): 139-148.

Nelson, S. J., et al. (2013). "Metabolic imaging of patients with prostate cancer using hyperpolarized [1-^{13}C]pyruvate." Sci Transl Med **5**(198): 198ra108.

Nimmakayala, R. K., et al. (2021). "Metabolic programming of distinct cancer stem cells promotes metastasis of pancreatic ductal adenocarcinoma." Oncogene **40**(1): 215-231.

Noll, E. M., et al. (2016). "CYP3A5 mediates basal and acquired therapy resistance in different subtypes of pancreatic ductal adenocarcinoma." Nat Med **22**(3): 278-287.

O'Neill, R. S. and A. Stoita (2021). "Biomarkers in the diagnosis of pancreatic cancer: Are we closer to finding the golden ticket?" World J Gastroenterol **27**(26): 4045-4087.

Odell, I. D. and D. Cook (2013). "Immunofluorescence techniques." J Invest Dermatol **133**(1): e4.

Puleo, F., et al. (2018). "Stratification of Pancreatic Ductal Adenocarcinomas Based on Tumor and Microenvironment Features." Gastroenterology **155**(6): 1999-2013.e1993.

Rao, Y., et al. (2020). "Hyperpolarized [1-(13)C]pyruvate-to-[1-(13)C]lactate conversion is rate-limited by monocarboxylate transporter-1 in the plasma membrane." Proc Natl Acad Sci U S A **117**(36): 22378-22389.

Riches, S. F., et al. (2009). "Diffusion-weighted imaging of the prostate and rectal wall: comparison of biexponential and monoexponential modelled diffusion and associated perfusion coefficients." NMR Biomed **22**(3): 318-325.

Rozenblum, E., et al. (1997). "Tumor-suppressive pathways in pancreatic carcinoma." Cancer Res **57**(9): 1731-1734.

S, N. K., et al. (2020). "Morphological classification of pancreatic ductal adenocarcinoma that predicts molecular subtypes and correlates with clinical outcome." Gut **69**(2): 317-328.

Serrano, O. K., et al. (2010). "The role of PET scanning in pancreatic cancer." Adv Surg **44**: 313-325.

Stødkilde-Jørgensen, H., et al. (2020). "Pilot Study Experiences With Hyperpolarized [1-(13) C]pyruvate MRI in Pancreatic Cancer Patients." J Magn Reson Imaging **51**(3): 961-963.

Sukeda, A., et al. (2019). "Expression of Monocarboxylate Transporter 1 Is Associated With Better Prognosis and Reduced Nodal Metastasis in Pancreatic Ductal Adenocarcinoma." Pancreas **48**(8): 1102-1110.

Tanimoto, K., et al. (2010). "Role of glucose metabolism and cellularity for tumor malignancy evaluation using FDG-PET/CT and MRI." Nucl Med Commun **31**(6): 604-609.

Tayari, N., et al. (2017). "In vivo MR spectroscopic imaging of the prostate, from application to interpretation." Anal Biochem **529**: 158-170.

Teruel, J. R., et al. (2016). "A Simplified Approach to Measure the Effect of the Microvasculature in Diffusion-weighted MR Imaging Applied to Breast Tumors: Preliminary Results." Radiology **281**(2): 373-381.

Trajkovic-Arsic, M., et al. (2017). "Apparent Diffusion Coefficient (ADC) predicts therapy response in pancreatic ductal adenocarcinoma." Sci Rep **7**(1): 17038.

Tuveson, D. A. and S. R. Hingorani (2005). "Ductal pancreatic cancer in humans and mice." Cold Spring Harb Symp Quant Biol **70**: 65-72.

Wang, W., et al. (2018). "E-cadherin is downregulated by microenvironmental changes in pancreatic cancer and induces EMT." Oncol Rep **40**(3): 1641-1649.

Wang, X. Y., et al. (2014). "Utility of PET/CT in diagnosis, staging, assessment of resectability and metabolic response of pancreatic cancer." World J Gastroenterol **20**(42): 15580-15589.

Woitek, R., et al. (2021). "Hyperpolarized Carbon-13 MRI for Early Response Assessment of Neoadjuvant Chemotherapy in Breast Cancer Patients." Cancer Res **81**(23): 6004-6017.

Xu, H., et al. (2017). "Automatic Nuclear Segmentation Using Multiscale Radial Line Scanning With Dynamic Programming." IEEE Trans Biomed Eng **64**(10): 2475-2485.

Yang, X., et al. (2002). "Generation of Smad4/Dpc4 conditional knockout mice." Genesis **32**(2): 80-81.

Ying, H., et al. (2012). "Oncogenic Kras maintains pancreatic tumors through regulation of anabolic glucose metabolism." Cell **149**(3): 656-670.

Zhang, L., et al. (2018). "Challenges in diagnosis of pancreatic cancer." World J Gastroenterol **24**(19): 2047-2060.

Zhao, M., et al. (2017). "Segmentation and classification of two-channel C. elegans nucleus-labeled fluorescence images." BMC Bioinformatics **18**(1): 412.

Zhou, B., et al. (2017). "Early detection of pancreatic cancer: Where are we now and where are we going?" Int J Cancer **141**(2): 231-241.

Zhu, M., et al. (2021). "Accuracy of quantitative diffusion-weighted imaging for differentiating benign and malignant pancreatic lesions: a systematic review and meta-analysis." Eur Radiol **31**(10): 7746-7759.

7. List of Figures, Tables, Codes and Formulas

1. List of figures

2. LIST OF TABLES

3. LIST OF CODES

4. LIST OF FORMULAS

8. BENEDICTION

Diese Arbeit ist meinem geliebten Sohn Emil gewidmet, der mir mit jedem Tag durch sein Lächeln und seine Neugier die Schönheit am Leben und am Forschen zeigt. Tiefen Dank möchte ich meinen Eltern Gudrun und Mathias und meinem Bruder Maximilian aussprechen, die mich während der gesamten Dauer der Erstellung dieser Arbeit unterstützt haben. Weiterhin möchte ich mich bei meinen akademischen Lehrern Irina Heid und Rickmer Braren bedanken, die mir durch konstruktives Feedback und tatkräftige Unterstützung das Fertigstellen dieser Arbeit ermöglicht haben.